UNIVERSIDADE FEDERAL DE PERNAMBUCO
CENTRO DE TECNOLOGIA E GEOCIÊNCIAS
DEPARTAMENTO DE ENGENHARIA CIVIL
PROGRAMA DE PÓS GRADUAÇÃO EM ENGENHARIA CIVIL

PEDRO VICTOR PAIXÃO ALBUQUERQUE

Finite Volume Method with Muiltipoint Flux and Stress Approximations Using Harmonic Points for Solving Poroelasticity Problems

Recife
2023

PEDRO VICTOR PAIXÃO ALBUQUERQUE

Finite Volume Method with Muiltipoint Flux and Stress Approximations Using Harmonic Points for Solving Poroelasticity Problems

Dissertation submitted to Universidade Federal de Pernambuco's Graduate Program in Civil Engineering as partial fulfilment of the requirements to obtain the Master of Civil Engineering Title.

Knowledge Area: Computational Simulation and Modeling Applied to Oil and the Environment

Supervisor: Darlan Karlo Elisiário de Carvalho, PhD
Co-supervisor: Paulo Roberto Maciel Lyra, PhD

Recife
2023

Catalogação na fonte
Bibliotecário Gabriel Luz, CRB-4 / 2222

A345f Albuquerque, Pedro Victor Paixão.
Finite volume method with muiltipoint flux and stress approximations using harmonic points for solving poroelasticity problems / Pedro Victor Paixão Albuquerque. 2023.
88 f: il.

Orientador: Prof. Dr. Darlan Karlo Elisiário de Carvalho.
Coorientador: Prof. Dr. Paulo Roberto Maciel Lyra.
Dissertação (Mestrado) – Universidade Federal de Pernambuco. CTG. Programa de Pós-Graduação em Engenharia Civil, Recife, 2023.
Inclui referências e apêndices.
Textos em inglês.

1. Engenharia civil. 2. Método dos volumes finitos. 3. Aproximação de fluxo por múltiplos pontos. 4. Simulação de reservatórios. 5. Poroelasticidade. 6. Geomecânica. I. Carvalho, Darlan Karlo Elisiário de (Orientador). II. Lyra, Paulo Roberto Maciel (Coorientador). III. Título.

UFPE

624 CDD (22. ed.) BCTG / 2023 - 38

PEDRO VICTOR PAIXÃO ALBUQUERQUE

FINITE VOLUME METHOD WITH MUILTIPOINT FLUX AND STRESS APPROXIMATIONS USING HARMONIC POINTS FOR SOLVING POROELASTICITY PROBLEMS

Dissertação em Engenharia Civil da Universidade Federal de Pernambuco, Centro de Tecnologia e Geociências, como requisito para obtenção do título de Mestre em Engenharia Civil, Área de Concentração Simulação e Gerenciamento de Reservatórios de Petróleo.

Aprovada em 03/02/2023

Orientador: Prof. Dr. Darlan Karlo Elisiário de Carvalho – Universidade Federal de Pernambuco
Corientador: Prof. Dr. Paulo Roberto Maciel Lyra - Universidade Federal de Pernambuco

BANCA EXAMINADORA

participação por videoconferência
Prof. Dr. Leonardo José do Nascimento Guimarães (examinador interno)
Universidade Federal de Pernambuco

participação por videoconferência
Prof. Dr. Alessandro Romário Echevarria Antunes (examinador externo)
Universidade Federal de Pernambuco

participação por videoconferência
Prof. Dr. Igor Fernandes Gomes (examinador externo)
Universidade Federal de Pernambuco

Dedicado à todos que fizeram
parte dessa jornada junto comigo.

ACKNOWLEDGEMENTS

I thank God for strength, courage and discipline. I especially thank my family for their support at all times, I thank my parents Antônio Ary de Albuquerque Filho and Ana Célia Paixão de Albuquerque for not only giving me support but also being an example and inspiration for my life.

I thank my supervisors Professor Darlan Karlo Elisário de Carvalho and Professor Paulo Roberto Maciel Lyra, who made a fundamental contribution to my academic education and to the development of this work. I would also like to thank professors Lucíolo Vitor Magalhães e Silva, Johantan da Cunha Teixeira and Fernando Raúl Licapa Contreras, who also contributed fundamentally to my academic training and to this work.

I thank the remaining of PPGEC professors for sharing their knowledge with me, during my academic training

I would like to thank my friends in the graduate program and my friends outside the program for their presence and support during this period.

Thanks to the rest of the PADMEC Family and the PPGEC staff for always being supportive and available.

I would like to thank everyone who participated in my academic training since graduation, the UFCG professors and colleagues.

Furthermore, this work was carried out with the support of the Coordination for the Improvement of Higher Education Personnel - Brazil (CAPES) - Financing Code 001 and Energi/Simulation - Code 53/2020.

ABSTRACT

Modeling physical phenomena and how they interact with each another is at the core of Science and Engineering. In the present work, the phenomena of interest is the so called Poroelasticy, which is a field of science that studies the relationship between fluid flow and solid deformation within a porous media. This theory have several applications such as in Geotechnical and Petroleum Engineering, Hydrogeology and even in Medicine and Biology, to name a few. In the context of Petroleum Reservoir Engineering, until recently, the reservoir rocks mechanical response was neglected, to reduce simulations costs, since the main phenomena of interest was how the fluid flows inside the reservoir. The presence of a freely moving fluid in a porous rock modifies its mechanical response and, in return, this mechanical response influences the fluid flow inside the pore. The mathematical modeling of the aforementioned physical phenomena results in a set of partial differential equations which only have proper analytical solutions in simple, non-realistic cases. However, with the development of numerical and computational tools, approximate solutions can be obtained, thus allowing the understanding and prediction of the behavior of such physical phenomena. The mathematical model used in the present work is based on Biot's theory of poroelasticity with the following assumptions for the solid phase: Quasi-static loading; Plane Strain; Infinitesimal Strain; Isotropic Linear Elasticity; Compressible Solid Matrix; and the following assumptions for the fluid phase: Single Phase Fluid; Slightly Compressible Fluid; Newtonian Fluid; Isotermic flow and; No gravitational effects. The set of Differential Equations were approximated via a unified finite volume framework, using a Multipoint Flux Approximation unsing Harmonic Points for both the fluid and solid equations, with a co-located variable arrangement and the Rhie-Chow interpolation, along with a Backwards Euler Scheme for temporal integration. The coupling between pressure and displacement was done via the fixed-strain split. The numerical modeling described in the present work is verified using benchmark problems found in the Poroelasticiy Literature. The results presented shows the numerical model is capable of producing robust and accurate approximated solutions, with both structured and unstructured meshes.

Keywords: finite volume method, multipoint flux approximation, poroelasticity, reservoir simulation, geomechanics.

RESUMO

Modelar os diversos fenômenos físicos que ocorrem na natureza e como eles interagem uns com os outros esta no cerne da Ciência e da Engenharia. No presente trabalho, o fenômeno de interesse é a chamada Poroelasticidade, que é um campo da ciência que estuda a relação entre escoamento de fluidos em meios porosos e a deformação do mesmo. Esta teoria tem várias aplicações, como em Engenharia Geotécnica e de Petróleo, Hidrogeologia e até em Medicina e Biologia. No contexto da Engenharia de Reservatórios de Petróleo, até recentemente, a resposta mecânica das rochas reservatório era negligenciada, para reduzir os custos de simulações, uma vez que o principal fenômeno de interesse é o escoamento de fluido dentro do reservatório. A presença de um fluido em movimento dentro de uma rocha porosa modifica sua resposta mecânica e, por sua vez, essa resposta mecânica influencia o fluxo do fluido no interior do poro. A modelagem matemática dos fenômenos físicos mencionados resulta em um conjunto de equações diferenciais parciais que só possuem soluções analíticas em casos muito simplificados. Porém, com o desenvolvimento de ferramentas numéricas e computacionais, soluções aproximadas podem ser obtidas, permitindo assim a compreensão e previsão do comportamento de tais fenômenos físicos. O modelo matemático utilizado no presente trabalho é baseado na teoria da poroelasticidade de Biot com as seguintes considerações para a fase sólida: Carregamento quase-estático; Estado Plano de Deformação; Deformação infinitesimal; Elasticidade Linear Isotrópica e; Matriz Sólida Compressível; e as seguintes hipóteses para a fase fluida: Fluido Monofásico; Fluido levemente compressível; Fluido Newtoniano; Escoamento isotérmico e; Sem efeitos gravitacionais. O conjunto de equações diferenciais foi aproximado por meio de uma estrutura unificada em volumes finitos, usando uma aproximação de fluxo por múltiplos pontos usando pontos harmônicos para as equações de fluido e sólido, e com arranjo co-localizado para as variaveis e a interpolação de Rhie-Chow, juntamente com um esquema de Euler implícito para a integração temporal. O acoplamento entre pressão e deslocamento foi feito via a técnica *Fixed-Strain*. A modelagem numérica descrita no presente trabalho é verificada através da solução de problemas de referência encontrados na literatura de poroelasticidade. Os resultados apresentados mostram que o modelo numérico é capaz de produzir soluções aproximadas robustas e acuradas, tanto com malhas estruturadas quanto não estruturadas.

Palavras-chave: método dos volumes finitos, aproximação de fluxo por múltiplos pontos, simulação de reservatórios, poroelasticidade, geomecânica.

LIST OF FIGURES

LIST OF TABLES

CONTENTS

1 INTRODUCTION

In nature, a plethora of physical phenomena occur and modeling those phenomena and how they interact with each another is at the core of Science and Engineering. Our modern lives is a direct result of this practice. In the present work, the phenomena of interest is the so called Poroelasticy. Poroelasticy is a field of science that studies the relationship between fluid flow and solid deformation within a porous media. The theory of Poroelasticity typical application is in Geotechnical and Petroleum Engineering since it's the basis of modeling soil consolidation (LIU, 2018) , which can also be used to predict the behavior of petroleum reservoir rocks. In addition, the theory is used in the field of Hydrogeology (WANG, 2000) and has several applications in Medicine and Biology such as modeling the mechanic behavior of: bones (COWIN, 1999), living tissue (MALANDRINO; MOEENDARBARY, 2019) and cytoplasm (MOEENDARBARY et al., 2013) to name a few.

The presence of a freely moving fluid in a porous rock modifies its mechanical response. In return, this mechanical response influences the fluid flow inside the the pore. Two mechanisms play a key role in this interaction between the interstitial fluid and the porous material: an increase of pore pressure induces a dilation of the media, and compression of the media causes a rise of pore pressure, if the fluid is prevented from escaping the pore network. Moreover, if excess pore pressure induced by compression of the Media is allowed to dissipate through fluid mass transport, further deformation of the media progressively takes place (DETOURNAY; CHENG, 1993).

The mathematical modeling of the aforementioned physical phenomena results in a set of partial differential equations. Such equations only have proper analytical solutions under simplifying assumptions. However, for most problems faced by scientist and engineers, such a solution isn't available. Nonetheless, with the development of numerical and computational tools, approximate solutions can be obtained with a certain degree of accuracy, thus allowing the understanding and prediction of the behavior of such physical phenomena. This is pivotal for scientific development and decision making. Therefore, it's natural to apply numerical tools to solve the set of partial differential equations that comprises the theory of Poroelasticity, in order to understand the mechanical response of porous media and the interstitial fluid flow, in real life scenarios.

In the context of Petroleum Reservoir Engineering, since the start of the usage of numerical tools and until the last decade, the reservoir rocks mechanical response was neglected. This was done to reduce computational costs, and the main phenomena of interest was how the fluid flows inside the reservoir. The reservoir mechanical response was reduced to a compressibility coefficient, which allowed the mathematical model to

capture how that response influenced the interstitial fluid flow. However, phenomena such as borehole collapse and ocean floor subsidence highlighted the necessity to understand how oil production affects the reservoir and surrounding rocks and vice-versa (ZOBACK, 2010). Those phenomena can impact significantly the production behavior which can lead to profit losses and enviromental harzads.

1.1 Literature Review

The theory of Poroelasticity began its development with (TERZAGHI, 1923). In this work, the author studies the compression of a water saturated soil, which is a gradual process called consolidation. Moreover, the author models and solves a unidimensional consolidation problem under the assumptions of homogeneous and isotropic linear elastic porous media, under constant total stress. However, Terzaghi's most important contribution in his paper was the principle that carries his name, Terzaghi's Effective Stress principle. This principle states that the load applied to a porous media is shared between the solid skeleton and the interstitial fluid (TERZAGHI, 1923; TERZAGHI, 1943; DETOURNAY; CHENG, 1993; WANG, 2000; LIU, 2018), and it's at the core of any theory modeling flow inside a non-rigid porous media. Later, Terzaghi's consolidation theory was extended to three dimensions by (RENDULIC, 1935; TERZAGHI; FRÖHLICH, 1936; TERZAGHI, 1943).

Another theory of tridimensional consolidation began its development with (BIOT, 1941). Biot's theory was developed under the same assumptions as Terzaghi's, even applying Terzaghi's Effective Stress principle. However, Biot did not assume constant total stress. As consequence, the linear momentum conservation equations were introduced, along with the mass balance equation used by Terzaghi, in order to account the changes in total stress. Therefore, Biot's theory leads to a system of partial differential equations. The constant total stress assumption allowed a decoupling between fluid flow and solid deformation (VERRUIJT, 2013), thus the mass balance equation was enough to describe the problem in Terzaghi's Theory, while deformations were computed via Hooke's Law and Terzaghi's Principle.

In (MANDEL, 1953), the author used Biot's theroy to derive a solution for the consolidation of a rectangular sample and, in (CRYER, 1963), the author compares Terzaghi's and Biot's solutions to the consolidation in a spherical soil sample. In the sphere's solution Terzaghi's Theory described a monotone decrease in fluid pressure, while Biot's predicted, in both the spherical and rectangular solutions, an initial slightly increase in fluid pressure followed by its decrease. This difference was precisely because the variation in total stress. This slightly increase in pressure was later experimentally verified and was named the Mandel-Cryer effect, after both authors. Thus, Biot's theory became the main

theory of consolidation and Poroelasticity.

Howerver, due to being a system of PDEs, Biot's theory has only a handful of analytical solutions, only for specific situations: (MCNAMEE; GIBSON, 1960a; MCNAMEE; GIBSON, 1960b; BOOKER, 1974; WANG; FANG, 2003; SARVA; RANI; KUMAR, 2013; AMIRI; HAJALI; ESMAEILY, 2014). For most real-life cases, Biot's theory has no analytic solutions. As consequence, numerical tools are used to solve the system of PDEs in modern applications. The Poroelasticity theory can be divided into two separate problems interacting with each other, fluid flow inside pores and solid deformation. Historically speaking, solid mechanics problems were predominately solved via a Finite Element Method (FEM). This was due to the fact that the energy conservation principle was commonly used in solving engineering problems. This, along with the development of variational calculus, allowed a natural development of FEMs, which have the property of minimizing energy norm errors in the approximation of self-adjoint (elliptic) operators (GRESHO; SANI, 2000). Furthermore, the early applications of the FEM were in the field of solid mechanics (TURNER et al., 1956; CLOUGH, 1960). On the other hand, fluid dynamics problems has been mainly solved via a Finite Volume Method (FVM). This was due to the presence of advective transport operators (first order derivatives) which pose a problem for standard Galerkin FEM (SPALDING, 2008). However, due to its definition, FVMs naturally enforces conservation locally. This property made FVMs, in general, better suited for fluid dynamics problems. Therefore, a numerical simulation of a poroelastic problem has to reconcile two different numerical methods into a single simulation. This problem is mainly solved by (ASADOLLAHI, 2017):

- Using a FEM/FVM scheme, i.e., using a FEM for the solid mechanics problem and a FVM for the fluid flow problem, which is common practice, specially when commercial or open source softwares are used.
- Using a FEM/FEM scheme, i.e. employing a FEM to also solve the fluid flow problem.
- Using a FVM/FVM scheme, i.e. employing a FVM to solve both fluid flow and solid mechanics problems.

They main disadvantage of the FEM/FVM scheme is the usage of different data structures, which requires a routine to do the information exchange between softwares. Both FEM/FVM and FEM/FEM suffers from non-physical oscillations, even when using 'even-odd' stable FEM formulations, such as Taylor-Hood FEM (ASADI; ATAIE-ASHTIANI, 2016; RODRIGO et al., 2016). FEM/FEM and FVM/FVM have the benefit of a unified data structure, which avoids unecessary interpolations. It is important to note that FEM formulations better capable of dealing with standard FEM limitations were developed, such as Discontinuous Galerkin (DG) and Mixed Finite Element Methods (MFEM) to name a

few. In their works, (ASADI; ATAIE-ASHTIANI, 2016; RODRIGO et al., 2016) themselves proposed more stable FEMs. However, despite its advantages, the usage of FVM for solid mechanics and even more the usage of a FVM/FVM scheme for poroelasticity are relative unexplored fields of research. The earliest paper using a finite volume method for solid mechanics was (DEMIRDZIC; MARTINOVIC; IVANKOVIC, 1988), 32 years after the first application of FEM, in solid mechanics (TURNER et al., 1956) and 17 years after the first application FVM, in fluid flow (MCDONALD, 1971). FEMs has advantages over FVMs, some of them being already mentioned, but the rest of them are outside the present scope of discussion. However FVMs have advantages over FEMs, some of them being (DEMIRDZIC, 2020): The FVM is developed considering an arbitrary convex polyhedral element, i. e. the FV discretisation is independent of the cell shape; FVMs have global and local conservation by definition, while FEMs are conservative, primarily, only globally and; FVMs usually have less degrees of freedom than FEMs. Furthermore, FVMs can be as accurate as FEMs (DEMIRDZIC, 2020).

Literature in the application of FVMs for solid mechanics is scarce and for Poroelasticity and Geomechanics is even more scarce. However, since its first development, FVMs for solid mechanics has been extended to deal with: solid-fluid interaction, e.g. (TUKOVIĆ et al., 2018); non-elastic materials, e.g (TANG; HEDEDAL; CARDIFF, 2015); anisotropic materials and finite strains, e.g. (CARDIFF; KARAČ; IVANKOVIĆ, 2014); fracture mechanics, e.g. (CAROLAN et al., 2013); contact mechanics, e.q. (CARDIFF; KARAČ; IVANKOVIĆ, 2012) and; wave propagation in porous media (GAO; ZHANG, 2006) to name a few. For a more extensive review of the applications of FVMs in solid mechanics one can refer to (CARDIFF; DEMIRDŽIĆ, 2021). Another set of noteworthy contributions were the works of (NORDBOTTEN, 2014b), which extended the family of classical FVMs called Multipoint Flux Approximations (MPFA) to the problem of solid mechanics, more precisely the MPFA-O, MPFA-U and the MPFA-L, and later develop a MPFA method exclusive to the solid mechanics problem, the MPFA-W (KEILEGAVLEN; NORDBOTTEN, 2017). Regarding FVMs applications in Poroelascity and Reservoir Geomechanics one can cite the works of (SHAW; STONE, 2005; PIZZOL; MALISKA, 2012; TUKOVIĆ; IVANKOVIĆ; KARAČ, 2013; NORDBOTTEN, 2014a; PIZZOL, 2014; TANG; HEDEDAL; CARDIFF, 2015), along with more applications of classical FVM such as the element-based finite volume method (EBFVM) for single phase (TONELLI, 2016; RIBEIRO, 2016; HONÓRIO, 2018a; HONORIO et al., 2018b; HONÓRIO; MARTINS; MALISKA, 2021) and multi-phase (GREIN, 2019) flow in poroelastic simulations, and application of FVM method in simulation softwares such as INMOST (TEREKHOV; VASSILEVSKI, 2019; TEREKHOV; TCHELEPI, 2020a; TEREKHOV, 2020b; TEREKHOV; VASSILEVSKI, 2022) and OpenFoam (TUKOVIĆ et al., 2018).

Along with the choice of approximation, it is necessary a strategy to deal with the coupling between fluid flow and solid deformation, since it is necessary to obtain

pressure and displacement fields that satisfy the system of PDEs at each time step. The coupling strategies for the Poroelasticity problem can be grouped in four main categories (ASADI; ATAIE-ASHTIANI; SIMMONS, 2014): fully, iteratively or sequentialy, explicitly and loosely coupled.

1.1.1 Fully Coupled Strategy

In the fully coupled approach, both discrete equations are assembled in a single system of equations, which is solved for both unknowns p and $\overrightarrow{u}$ simultaneously in each time step (SETTARI; WALTERS, 2001). The fully coupled option is linearly unconditionally stable, but it is computationally expensive (KIM; TCHELEPI; JUANES, 2011c).

1.1.2 Iteratively/Sequentialy Coupled Strategy

In the iteratively coupled approach, also called two-way coupling, information is exchanged between the mechanics and flow equations sequentially until the solution converges within an acceptable tolerance at each time step. The iteratively coupled option is, in general, less computationally expensive and allows for the use of different computational domains for the flow and mechanical problems. However, some iterative schemes can be conditionally stable, and even non-convergent when stable. The main four sequential methods are (KIM; TCHELEPI; JUANES, 2011a; KIM; TCHELEPI; JUANES, 2011b; KIM; TCHELEPI; JUANES, 2011c):

- Drained Split: In this scheme, the solution is obtained sequentially by first solving the mechanics problem with constant pressure, then the fluid-flow problem is solved with a frozen displacement field. This split is conditionally stable and can be non-convergent even when it is stable.
- Undrained Split: In this scheme, the solution is obtained sequentially by first solving the mechanics problem with constant fluid mass content, then the fluid-flow problem is solved with a frozen displacement field. This assumption yields a different pressure predictor in contrast to the Drained Split. This method is unconditionally stable though it requires an increased number of iterations as coupling strength between fluid and solid problem increases and is non-convergent in case of a fully incompressible system.
- Fixed-Strain Split: In this scheme, the solution is obtained sequentially by first solving the fluid-flow problem with constant volumetric deformation, then the mechanics problem is solved with a frozen pressure field. This split also is conditionally stable and can be non-convergent even when it is stable.

- Fixed-Stress Split: In this scheme, the solution is obtained sequentially by first solving the fluid-flow problem with constant total mean stress, then the mechanics problem is solved with a frozen pressure field. This assumptions yields a additional term summed to the accumulation term in the mass balance equation. This split is as accurate and stable as fully coupled scheme.

1.1.3 Explicitly Coupled Strategy

In the explicitly coupled approach, also called one-way coupling, any operator split defined in Section 1.1.2 can be employed. However, the solution obtained in the first iteration is considered the converged solution for the time step. The exchange of information is unidirectional, thus one-way coupling. This strategy have reduced computational costs along with reduced accuracy, when compared with two-way coupling strategies.

1.1.4 Loosely Coupled Strategy

In the loosely coupled approach, also known as sub-cycling technique, different time steps are used in the fluid flow and solid deformation problem. The flow equation is calculated for each time step but mechanical updates are performed after multiple flow time steps. This strategy can be employed since fluid flow parameters (pressure) change over shorter time frames than mechanics parameters (displacement) which progress more slowly. Thus, pressure variations impose restriction on the growth of time step size throughout the course of simulation (MINKOFF; KRIDLER, 2006). The main three strategies to control when perform the mechanical updates are (ASADI; ATAIE-ASHTIANI; SIMMONS, 2014):

- Constant step size: In this method, the displacements are updated after a fixed amount of pressure time steps, regardless of the solution.
- Pore pressure method: In this method, current pore pressure is compared to the pore pressure in the last mechanical update. When this difference exceeds a threshold value, mechanical variables are updated.
- Local error method: In this method, a relative error is computed using displacement from two consecutive mechanical steps. Then, this error is compared to a goal local error, and based on this comparison, the time step for the next mechanical update is increased, decreased or unchanged, or the current mechanical update is redone with a smaller time step.

1.2 Objectives

The main objective of the present work is to develop a unified finite volume framework for solving poroelasticity problems, capable of handling unstructured meshes and full permeability and constitutive tensors.

The specific objectives of the present work are:

- Develop a FVM, based in the MPFA method using harmonic points (MPFA-H), for the solid mechanics problem.
- Employ the developed FVM for solid mechanics in solving Poroelasticity problems using the Fixed-Strain Split.
- Develop a software in python for numerical modeling of Poroelasticity problems.
- Verify the numerical model against benchmark problems.
- Analysis of the numerical convergence rates of the FVM/FVM scheme.
- Analysis of the numerical simulation results conformation with the expected physics of the problem.

1.3 Dissertation Outline

The present Dissertation is organized as follows:

- In Chapter 2, a description of the mathematical model is presented: the hypothesis used, governing equations, constitutive relationships and auxiliary conditions (initial and boundary conditions). In addition, a discussion about the coupling between variables is presented, along with the methodology used in the present work;
- In Chapter 3, the set of PDE's are discretized using the MPFA-H FVM, and the solution algorithm is presented;
- In Chapter 4, the numerical modeling discussed in the present work is verified against elementary problems found in the Poroelasticity literature;
- In Chapter 5, closing remarks and suggestions for future works are presented;

2 MATHEMATICAL MODEL

The mathematical model used in this work is based on Biot's theory of Consolidation. The model is comprised by two main partial differential equations, one describing the in-pore fluid behaviour and another describing the porous media mechanical response, along with the necessary constitutive relationships. The equations are derived under a Eulerian description of the problem. On the following description of the mathematical model, the equations pertaining to the fluid flow are called the fluid subsystem, and the ones that describe the the porous media mechanical response are called the solid subsystem.

2.1 Solid Subsystem

The hypothesis adopted to describe the porous media mechanical behavior are:

- Quasi-static loading;
- Plane Strain;
- Infinitesimal Strain;
- Isotropic Linear Elasticity;
- Compressible Solid Matrix;

2.1.1 Governing Equation

Since there is no changes in solid temperature (Isotermic Deformation), the only equation modelling the mechanical behavior of the porous media is the conservation of linear momentum, more precisely the Cauchy's Law of Motion. By assuming a quasi-static loading on the porous media, even tho the stress field changes over time, any given representative elementary volume is in a state of static force (translational and rotational) equilibrium at any point in time. Therefore, due to translational equilibrium, Cauchy's equations reduce to the stress equilibrium equations (WANG, 2000):

$$\nabla \cdot \underline{\sigma} + \overrightarrow{f} = 0 \tag{2.1}$$

with $\underline{\sigma}$ being the Cauchy's Stress Tensor, $\overrightarrow{f}$ comprising the body forces acting on the elastic body, and $\nabla\cdot$ is the divergence operator . Under spatial coordinates (Eulerian

Description) Cauchy's Stress Tensor is sufficient to describe the elastic body stress state and can be written as (WANG, 2000):

$$\underline{\sigma} = \begin{bmatrix} \sigma_{xx} & \sigma_{xy} & \sigma_{xz} \\ \sigma_{yx} & \sigma_{yy} & \sigma_{yz} \\ \sigma_{zx} & \sigma_{zy} & \sigma_{zz} \end{bmatrix} \tag{2.2}$$

Moreover, the rotational equilibrium implies Cauchy's tensor is symmetric. Thus $\sigma_{xy} = \sigma_{yx}$, $\sigma_{xz} = \sigma_{zx}$ and $\sigma_{zy} = \sigma_{yz}$ (WANG, 2000).

2.1.2 Terzaghi's Effective Stress Principle

Terzaghi's Effective Stress Principle states that the total stress $\underline{\sigma}$ on a porous media has two components: one acting on the in-pore fluid, which is its pressure p and one acting exclusively on the solid phase (solid matrix), called effective stress $\underline{\sigma'}$ (WANG, 2000). When adopting the convention of tension loads having positive signs, this contributions can be computed using the following expression:

$$\underline{\sigma'} = \underline{\sigma} - \alpha p \underline{\mathbf{I}} \tag{2.3}$$

where $\underline{\sigma'}$ is called the Effective Stress, α is Biot's coefficient, p is the fluid pressure and $\underline{\mathbf{I}}$ is the identity matrix. Furthermore, according to Terzaghi's Principle, the porous media mechanical behaviour under $\underline{\sigma}$ is equivalent to a non-porous material under $\underline{\sigma'}$. Therefore, $\underline{\sigma'}$ is the one being used in the stress-strain relationship. Moreover, Biot's coefficient can be expressed as:

$$\alpha = 1 - \frac{c_s}{c_m} \tag{2.4}$$

where c_s is the solid particles compressibility and c_m is the compressibility of the whole porous media.

By substituting Eq. (2.3) into Equation (2.1), one can arrive at the following expression:

$$\nabla \cdot \underline{\sigma'} - \alpha \nabla p + \overrightarrow{f} = 0 \tag{2.5}$$

where ∇ is the gradient operator.

2.1.3 Infinitesimal Strain

Under the Eulerian description of the problem, strain is measured by the Almansi-Hamel strain tensor (SLAUGHTER, 2012). Furthermore, by imposing the assumption of the Infinitesimal Strain Theory, which means the displacement gradients are infinitesimal ($\nabla \overrightarrow{u} << 1$) throughout the whole elastic body, the Almansi-Hamel strain tensor can be defined as (SLAUGHTER, 2012):

$$\underline{\varepsilon} = \frac{\nabla \overrightarrow{u} + (\nabla \overrightarrow{u})^{\top}}{2} \tag{2.6}$$

with $\overrightarrow{u} = [u\ v\ w]^{\top}$ being the displacement vector, whose components are u, v and w. The displacement vector gives the changes in particle position, where $u = \delta x$, $v = \delta y$ and $w = \delta z$. Due to the it's definition, along with Cauchy's stress tensor, the Almansi-Hamel (also known as the Eulerian strain tensor) is also symmetric.

2.1.4 Hooke's Law

Under the assumptions of linear elasticity, the constitutive relation between effective stress and strain is given by the Generalized Hooke's Law (SLAUGHTER, 2012), which is represented by the following tensor contraction:

$$\underline{\sigma}' = \underline{\mathbf{C}} : \underline{\varepsilon} \tag{2.7}$$

In Equation (2.7), $\underline{\mathbf{C}}$ is a rank 4 constitutive tensor. Under the assumption of isotropic linear elasticity, all 81 entries of $\underline{\mathbf{C}}$ can be written as functions of only two parameters, λ and G, which are called respectively Lamé's first and second parameters. G is also know as the shear modulus. Using the Lamé parameters, Eq. (2.7) can be written as (IRGENS, 2008):

$$\underline{\sigma}' = \lambda tr\left(\underline{\varepsilon}\right) \underline{\mathbf{I}} + 2G\underline{\varepsilon} \tag{2.8}$$

where $tr(\cdot)$ represents a matrix trace. Furthermore, the Lamé parameters can be expressed in term of other two material properties: the Young modulus E and Poisson's ratio ν:

$$\lambda = \frac{E\nu}{(1+\nu)(1-2\nu)},\ G = \frac{E}{2(1+\nu)} \tag{2.9}$$

Another important relationship is the one between effective isotropic stress σ_v' and the volumetric strain ε_v:

$$\sigma'_v = K\varepsilon_v \tag{2.10}$$

where $K = 1/c_m$ is known as the Bulk modulus, $\sigma'_v = tr(\underline{\sigma}')/3$ and $\varepsilon_v = tr(\underline{\varepsilon})$. The variables σ'_v and ε_v are the stress and strain components that contribute to changes in the elastic body's volume. The other stress and strain components, called shear components, only contributes to changes in the elastic body's shape. Furthermore, any pair of material properties (λ, G, E, ν and K) is enough to define Hooke's law for a isotropic elastic body.

2.1.5 Plane Strain

The Plane Strain (also called Plane Displacements) hypothesis implies that strain is restricted to a single plane: $\overrightarrow{u} = [u(x,y,t) \;\; v(x,y,t)]^\top$ and $w = 0$ (IRGENS, 2008). Thus, $\varepsilon_{xz} = \varepsilon_{yz} = \varepsilon_{zx} = \varepsilon_{zy} = \varepsilon_{zz} = 0$. Therefore, $\underline{\varepsilon}$ and $\underline{\sigma}'$ become:

$$\underline{\varepsilon} = \begin{bmatrix} \varepsilon_{xx} & \varepsilon_{xy} & 0 \\ \varepsilon_{yx} & \varepsilon_{yy} & 0 \\ 0 & 0 & 0 \end{bmatrix}, \; \underline{\sigma}' = \begin{bmatrix} \sigma'_{xx} & \sigma'_{xy} & 0 \\ \sigma'_{yx} & \sigma'_{yy} & 0 \\ 0 & 0 & \sigma'_{zz} \end{bmatrix} \tag{2.11}$$

The non-zero σ'_{zz} is necessary in order to ensure $\varepsilon_{zz} = 0$. Its value can be obtained via Hooke's Law as $\sigma'_{zz} = \nu(\sigma'_{xx} + \sigma'_{yy})$. Moreover, σ'_{zz} can be removed from the analysis, which turns the 3D problem into a much simpler 2D problem (IRGENS, 2008):

$$\underline{\varepsilon} = \begin{bmatrix} \varepsilon_{xx} & \varepsilon_{xy} \\ \varepsilon_{yx} & \varepsilon_{yy} \end{bmatrix}, \; \underline{\sigma}' = \begin{bmatrix} \sigma'_{xx} & \sigma'_{xy} \\ \sigma'_{yx} & \sigma'_{yy} \end{bmatrix} \tag{2.12}$$

where:

$$\sigma'_{xx} = \lambda\varepsilon_v + 2G\varepsilon_{xx}, \;\; \sigma'_{yy} = \lambda\varepsilon_v + 2G\varepsilon_{yy}, \;\; \sigma'_{xy} = \sigma'_{yx} = 2G\varepsilon_{xy} \tag{2.13}$$

$$\varepsilon_{xx} = \frac{\partial u}{\partial x}, \;\; \varepsilon_{yy} = \frac{\partial v}{\partial y}, \;\; \varepsilon_{xy} = \varepsilon_{yx} = \frac{1}{2}\left(\frac{\partial u}{\partial x} + \frac{\partial v}{\partial y}\right) \tag{2.14}$$

2.1.6 Navier-Cauchy Equation

By substituting Equation (2.8) into Equation (2.5) and doing the necessary algebraic manipulations, one can arrive at a poromechanical equivalent of the Navier-Cauchy Equation, which is given by:

$$(\lambda + G)\,\nabla\,(\nabla \cdot \overrightarrow{u}) + G\nabla \cdot (\nabla \overrightarrow{u}) - \alpha \nabla p = \overrightarrow{f} \tag{2.15}$$

2.1.7 Boundary Conditions

A proper set of boundary conditions for Eq. (2.5) is given by:

$$\begin{aligned} &\overrightarrow{u}\,(x,t) = \overrightarrow{g}^{u}_{D} \quad in \quad \Gamma^{u}_{D} \\ &\underline{\sigma'} \cdot \overrightarrow{n} = \overrightarrow{g}^{u}_{N} \quad in \quad \Gamma^{u}_{N} \end{aligned} \tag{2.16}$$

where $\overrightarrow{n}$ is the unit outward normal vector to the boundary, Γ^{u}_{D} denotes the Dirichlet Boundary and Γ^{u}_{N} denotes the Neumann Boundary, both for the geomechanical problem. $\overrightarrow{g}^{u}_{D}$ along with $\overrightarrow{g}^{u}_{N}$ are the prescribed values of the displacement $\overrightarrow{u}$ and traction $\underline{\sigma'} \cdot \overrightarrow{n}$ at the boundary, respectively.

Even though there is no time derivative in Eq. (2.5) due to the elastostatic condtion, $\overrightarrow{u}$ still changes over time, which entails a initial condition, which is given by:

$$\overrightarrow{u}\,(x,0) = \overrightarrow{u}_{0} \quad in \quad \Omega \tag{2.17}$$

where $\overrightarrow{u}_{0}$ is the initial values of displacement.

2.2 Fluid Subystem

The hypothesis adopted to describe the fluid behavior are:

- Single Phase Fluid;
- Slightly Compressible Fluid;
- Newtonian Fluid;
- No gravitational effects;

2.2.1 Governing Equation

Since there are no changes in fluid temperature (Isotermic Flow), the only equation modelling the fluid flow inside a porous media is the mass conservation. For the fluid phase, the mass conservation inside the pore is given by (VERRUIJT, 2013):

$$\frac{\partial\left(\phi\rho_f\right)}{\partial t} + \nabla\cdot\left(\phi\rho_f\overrightarrow{v_f}\right) = q_f \tag{2.18}$$

where ϕ is the porosity of the porous media, ρ_f is the fluid density, $\overrightarrow{v_f}$ is the fluid velocity and q_f is the source (or sink) term.

The fluid compressibility c_f can be expressed as follows:

$$c_f = \frac{1}{\rho_f}\frac{d\rho_f}{dp} \tag{2.19}$$

Due to the slightly compressible fluid consideration, c_f has a non-zero, constant value. By substituting Eq. (2.19), and doing some algebraic manipulation, Eq. (2.18) becomes:

$$\frac{\partial\phi}{\partial t} + \phi c_f\frac{\partial p}{\partial t} + \nabla\cdot\left(\phi\overrightarrow{v_f}\right) = Q_f \tag{2.20}$$

where $Q_f = q_f/\rho_f$.

The mass conservation principle applied to the solid material yields (VERRUIJT, 2013):

$$\frac{\partial\left[\left(1-\phi\right)\rho_s\right]}{\partial t} + \nabla\cdot\left[\left(1-\phi\right)\rho_s\overrightarrow{v_s}\right] = 0 \tag{2.21}$$

where ρ_s and $\overrightarrow{v_s}$ are the solid particles density and velocity respectively.

Then, it's assumed that ρ_s is a function of the total isotropic stress σ_v and the fluid pressure p such that (VERRUIJT, 2013):

$$\left(1-\phi\right)\frac{\partial\rho_s}{\partial t} = \rho_s c_s\left(-\frac{\partial\sigma_v}{\partial t} - \phi\frac{\partial p}{\partial t}\right) \tag{2.22}$$

where c_s is the solid particle compressibility and $\sigma_v = tr(\underline{\sigma})/3$.

By using Eq. (2.22), Eq. (2.21) can be written as:

$$-\frac{\partial\phi}{\partial t} + c_s\left(-\frac{\partial\sigma_v}{\partial t} - \phi\frac{\partial p}{\partial t}\right) - \nabla\cdot\left[\left(1-\phi\right)\overrightarrow{v_s}\right] = 0 \tag{2.23}$$

By adding Eq. (2.20) and Eq. (2.21), one gets:

$$\phi\left(c_f - c_s\right)\frac{\partial p}{\partial t} - c_s\frac{\partial \sigma_v}{\partial t} + \nabla\cdot\overrightarrow{v_t} + \nabla\cdot\overrightarrow{v_s} = Q_f \tag{2.24}$$

where $\overrightarrow{v_t} = \phi\left(\overrightarrow{v_f} - \overrightarrow{v_s}\right)$ is the Darcy velocity for a fluid in a non-rigid porous media. In a rigid porous media ($\overrightarrow{v_s} = 0$) the Darcy velocity is just $\overrightarrow{v_t} = \phi\overrightarrow{v_f}$.

By using the following relations: $\sigma_v = \sigma'_v - \alpha p$ (Terzaghi's Principle); $\sigma'_v = \varepsilon_v / c_m$; $tr(\underline{\varepsilon}) = \nabla\cdot\overrightarrow{u}$; Eq. (2.24) becomes (VERRUIJT, 2013):

$$S\frac{\partial p}{\partial t} + \nabla\cdot\overrightarrow{v_t} + \alpha\frac{\partial \varepsilon_v}{\partial t} = Q_f \tag{2.25}$$

where $S = \phi c_f + (\alpha - \phi)\, c_s$ is called the storage coefficient and Eq. (2.25) is also called The Storage Equation.

2.2.2 Darcy's Law

Darcy's Law is a constitutive relation between the in-pore fluid Darcy Velocity and the pressure gradient inside same pore. For a single phase fluid and neglecting gravitational effects, Darcy's Law can be written as (EWING, 1983):

$$\overrightarrow{v_t} = -\frac{1}{\mu}\underline{K}\nabla p \tag{2.26}$$

with μ being the fluid viscosity and $\underline{K}$ being the porous media permeability tensor. Due to the Newtonian Fluid hypothesis, μ assumes a constant value throughout the simulation.

2.2.3 Boundary Conditions

A proper set of boundary conditions for Eq. (2.25) is given by:

$$\begin{aligned} p\left(x,t\right) &= g_D^p \quad in \quad \Gamma_D^p \\ \overrightarrow{v_t}\cdot\overrightarrow{n} &= g_N^p \quad in \quad \Gamma_N^p \end{aligned} \tag{2.27}$$

where $\overrightarrow{n}$ is the unit normal vector to the boundary, Γ_D^p denotes the Dirichlet Boundary and Γ_N^p denotes the Neumann Boundary, both for the flow problem. $\overrightarrow{g}_D^p$ along with $\overrightarrow{g}_N^p$ are the prescribed values of the pressure p and flux $\overrightarrow{v_t}\cdot\overrightarrow{n}$ at the boundary.

Moreover, initial conditions is for the fluid flow problem are given by:

$$p\left(x,0\right) = p_0 \quad in \quad \Omega \tag{2.28}$$

where p_0 is the initial values of pressure.

2.3 Complete Poroelastic Model

In short, the coupled poroelastic model used in the present work involves the following equations:

- Stress Equilibrium Equation ,Eq. (2.5):

$$\nabla \cdot \underline{\sigma}' - \alpha \nabla p + \overrightarrow{f} = 0$$

- Hooke's Law, Eq. (2.8):

$$\underline{\sigma}' = \lambda tr\left(\underline{\varepsilon}\right) \underline{\mathbf{I}} + 2G\underline{\varepsilon}$$

- Strain-Displacement Relationship , Eq. (2.6):

$$\underline{\varepsilon} = \frac{\nabla \overrightarrow{u} + \nabla \overrightarrow{u}^{\top}}{2}$$

- The Storage Equation, Eq. (2.25):

$$S\frac{\partial p}{\partial t} + \nabla \cdot \overrightarrow{v_t} + \alpha \frac{\partial \varepsilon_v}{\partial t} = Q_f$$

- Darcy's Law, Eq. (2.26):

$$\overrightarrow{v_t} = -\frac{1}{\mu}\underline{K}\nabla p$$

- Boundary conditions, Eq. (2.27) and Eq. (2.16):

$$\overrightarrow{u}\left(x,t\right) = \overrightarrow{g}_D^u \quad in \quad \Gamma_D^u$$

$$\underline{\sigma}' \cdot \overrightarrow{n} = \overrightarrow{g}_N^u \quad in \quad \Gamma_N^u$$

$$p\left(x,t\right) = g_D^p \quad in \quad \Gamma_D^p$$

$$\overrightarrow{v} \cdot \overrightarrow{n} = g_N^p \quad in \quad \Gamma_N^p$$

- Initial Conditions, Eq. (2.28) and Eq. (2.17):

$$\overrightarrow{u}\left(x,0\right) = \overrightarrow{u}_0 \quad in \quad \Omega$$

$$p\left(x,0\right) = p_0 \quad in \quad \Omega$$

The mathematical description above has two coupling terms: $\alpha\nabla p$ in the solid equation, which comes from the solution of the fluid subsystem and $\alpha\dot{\varepsilon_v}$ in the fluid equation, comes from the solution of the solid subsystem. It is important to note that both terms are multiplied by Biot's coefficient α. Physically speaking, α represents how the momentum transferred through the porous media is shared by both the solid and the fluid phases.

3 NUMERICAL FORMULATION

This work uses a collocated cell-centred finite volume scheme. The main unknowns are p, cell pressure, u and v, cell displacements. The first step is to split the computational domain Ω into N_{cv} computational cells $\hat{L}$, with N_{cv} being the number of cells. Next step is to work with the integral formulation of the PDEs. Then the integral over the whole domain Ω is split into N_{cv} integrals over a cell domain $\Omega_{\hat{L}}$. The following description is how each term of each PDE is approximated inside the cell domain $\Omega_{\hat{L}}$. The integral formulation of Eq. (2.5) and Eq. (2.25) for a control volume $\hat{L}$ is as follows:

$$\int_{\Omega_{\hat{L}}} \nabla \underline{\sigma}' \, d\Omega_{\hat{L}} - \int_{\Omega_{\hat{L}}} \alpha \nabla p \, d\Omega_{\hat{L}} = \int_{\Omega_{\hat{L}}} \overrightarrow{f} \, d\Omega_{\hat{L}} \tag{3.1}$$

$$\int_{\Omega_{\hat{L}}} S \frac{\partial p}{\partial t} \, d\Omega_{\hat{L}} + \int_{\Omega_{\hat{L}}} \nabla \cdot \overrightarrow{v_t} \, d\Omega_{\hat{L}} + \int_{\Omega_{\hat{L}}} \alpha \frac{\partial \varepsilon_v}{\partial t} \, d\Omega_{\hat{L}} = \int_{\Omega_{\hat{L}}} Q_f \, d\Omega_{\hat{L}} \tag{3.2}$$

3.1 Solid Subsystem

3.1.1 Multipoint Stress Approximation using Harmonic Points (MPSA-H)

To approximate the effective stress divergent (first term of Eq. (3.1)) integral over a cell domain $\Omega_{\hat{L}}$, under a Finite Volume approximation, first the Divergence Theorem is applied as follows:

$$\int_{\Omega_{\hat{L}}} \nabla \underline{\sigma}' \, d\Omega_{\hat{L}} = \int_{\Gamma_{\hat{L}}} \underline{\sigma}' \cdot \overrightarrow{n} \, d\Gamma_{\hat{L}} \tag{3.3}$$

In Equation (3.3), $\Gamma_{\hat{L}}$ is the computational cell $\hat{L}$ boundary, and $\overrightarrow{n}$ is the unit outward normal vector to $\Gamma_{\hat{L}}$. Since the computational cells $\hat{L}$ are star-shaped polygons, the following identity holds:

$$\int_{\Gamma_{\hat{L}}} \underline{\sigma}' \cdot \overrightarrow{n} \, d\Gamma_{\hat{L}} = \sum_{IJ \in \Gamma_{\hat{L}}} \int_{IJ} \underline{\sigma}' \cdot \overrightarrow{n} \, ds \tag{3.4}$$

where IJ is a cell's face (edge in 2D). Furthermore, the integral over a cell face can be approximated via the Mean Value Theorem as follows:

$$\int_{IJ} \underline{\sigma}' \cdot \overrightarrow{n}\ ds \approx |IJ| \underline{\sigma}' \cdot \overrightarrow{n}_{IJ} = |IJ| \overrightarrow{\mathcal{T}}_{IJ} \tag{3.5}$$

where $\overrightarrow{\mathcal{T}}_{IJ} = \underline{\sigma}' \cdot \overrightarrow{n}_{IJ}$ is known as the traction vector. When $|IJ| \to 0$, the aforementioned approximation becomes exact. Furthermore, one can write the traction vector as follows:

$$\overrightarrow{\mathcal{T}}_{IJ} = \left[\underline{\mathbf{C}} : \frac{\nabla \overrightarrow{u} + \nabla \overrightarrow{u}^{\top}}{2} \right] \cdot \overrightarrow{n}_{IJ} = \begin{bmatrix} \nabla u \cdot \underline{C}^{xx} \overrightarrow{n}_{IJ} + \nabla v \cdot \underline{C}^{xy} \overrightarrow{n}_{IJ} \\ \nabla u \cdot \underline{C}^{yx} \overrightarrow{n}_{IJ} + \nabla v \cdot \underline{C}^{yy} \overrightarrow{n}_{IJ} \end{bmatrix} \tag{3.6}$$

where $\underline{C}^{xx}$, $\underline{C}^{xy}$, $\underline{C}^{yx}$, $\underline{C}^{yy}$ are diffusion coefficients constructed from $\underline{\mathbf{C}}$. Therefore, $\underline{C}^{xx} \overrightarrow{n}_{IJ}$, $\underline{C}^{xy} \overrightarrow{n}_{IJ}$, $\underline{C}^{yx} \overrightarrow{n}_{IJ}$, $\underline{C}^{yy} \overrightarrow{n}_{IJ}$ are co-normal vectors. The aforementioned diffusion coefficients are defined, under the isotropic linear elasticity assumption, as:

$$\underline{C}^{xx} = \begin{bmatrix} \lambda + 2G & 0 \\ 0 & G \end{bmatrix},\ \underline{C}^{xy} = \underline{C}^{yx\top} \begin{bmatrix} 0 & G \\ \lambda & 0 \end{bmatrix},\ \underline{C}^{yy} = \begin{bmatrix} G & 0 \\ 0 & \lambda + 2G \end{bmatrix} \tag{3.7}$$

The next step is to use the approximation for a generic diffusion term defined in (GAO; WU, 2014). Considering two generic computational cells $\hat{L}$ and $\hat{R}$, which shares the common edge IJ, one can write the stress vector on IJ using the properties of each cell as:

$$\overrightarrow{\mathcal{T}}^{\hat{L}}_{IJ} = \begin{bmatrix} \nabla u_{\hat{L}} \cdot \underline{C}^{xx}_{\hat{L}} \overrightarrow{n}_{IJ} + \nabla v_{\hat{L}} \cdot \underline{C}^{xy}_{\hat{L}} \overrightarrow{n}_{IJ} \\ \nabla u_{\hat{L}} \cdot \underline{C}^{yx}_{\hat{L}} \overrightarrow{n}_{IJ} + \nabla v_{\hat{L}} \cdot \underline{C}^{yy}_{\hat{L}} \overrightarrow{n}_{IJ} \end{bmatrix} \tag{3.8}$$

$$\overrightarrow{\mathcal{T}}^{\hat{R}}_{IJ} = \begin{bmatrix} \nabla u_{\hat{R}} \cdot \underline{C}^{xx}_{\hat{R}} \overrightarrow{n}_{JI} + \nabla v_{\hat{R}} \cdot \underline{C}^{xy}_{\hat{R}} \overrightarrow{n}_{JI} \\ \nabla u_{\hat{R}} \cdot \underline{C}^{yx}_{\hat{R}} \overrightarrow{n}_{JI} + \nabla v_{\hat{R}} \cdot \underline{C}^{yy}_{\hat{R}} \overrightarrow{n}_{JI} \end{bmatrix} \tag{3.9}$$

where $\overrightarrow{n}_{JI} = -\overrightarrow{n}_{IJ}$. Next, we decompose each co-normal vector as follows:

$$\underline{C}^{\eta}_{\hat{L}} \overrightarrow{n}_{IJ} = \alpha^{\eta}_{\hat{L},i(IJ)} \overrightarrow{x_{\hat{L}} x_{\hat{L},i(IJ)}} + \alpha^{\eta}_{\hat{L},j(IJ)} \overrightarrow{x_{\hat{L}} x_{\hat{L},j(IJ)}},\ \eta = xx,\ xy,\ yx,\ yy \tag{3.10}$$

where $x_{\hat{L},i(IJ)}$ and $x_{\hat{L},j(IJ)}$ are auxiliary points inside $\hat{L}$, which may or may not belong to IJ (See Fig. 1. In the Finite Volume method presented in this work, the auxiliary points are the Harmonic Point. A harmonic point $x_{\hat{L},i(IJ)}$ is a point belonging to the edge IJ in which the value of the solution field (e.g. Displacement) is a function of only the two computational cells that share IJ. However, to construct the average stress vector in each face IJ, two harmonic points are necessary. The pair of harmonic points used in the approximation are required to satisfy the following conditions:

1. With $\theta^1_{\hat{L},IJ}$ and $\theta^2_{\hat{L},IJ}$ being the angles between $\underline{C}^{\eta}_{\hat{L}}\,\vec{n}_{IJ}$ and $\overrightarrow{x_{\hat{L}}x_{\hat{L},i(IJ)}}$, and between $\underline{C}^{\eta}_{\hat{L}}\,\vec{n}_{IJ}$ and $\overrightarrow{x_{\hat{L}}x_{\hat{L},i(IJ)}}$, respectively (See Fig 1), each angle and their sum, $\theta^1_{\hat{L},IJ}+\theta^2_{\hat{L},IJ}$, must lie in the interval $[0,\pi)$

2. The Cross products $\underline{C}^{\eta}_{\hat{L}}\,\vec{n}_{IJ} \times \overrightarrow{x_{\hat{L}}x_{\hat{L},i(IJ)}}$ and $\underline{C}^{\eta}_{\hat{L}}\,\vec{n}_{IJ} \times \overrightarrow{x_{\hat{L}}x_{\hat{L},j(IJ)}}$ must have positive sign.

Figure 1 – Points used in the stress approximation

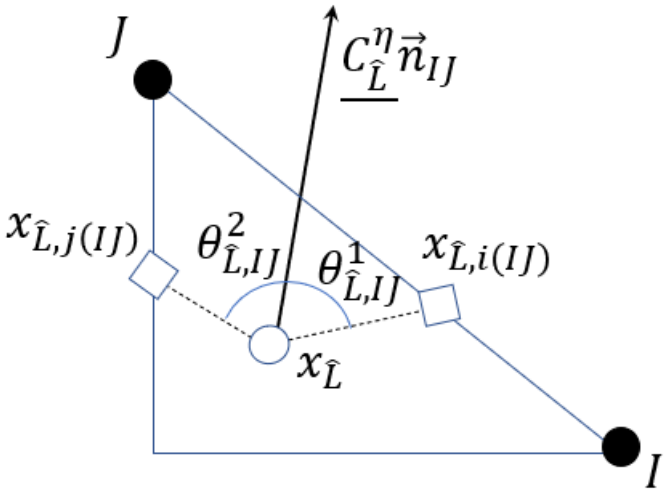

Source: Own authorship (2023)

Furthermore, $\alpha^{\eta}_{\hat{L},i(IJ)}$ and $\alpha^{\eta}_{\hat{L},j(IJ)}$ are defined as:

$$\alpha^{\eta}_{\hat{L},i(IJ)} = \frac{\left(\underline{C}^{\eta}_{\hat{L}}\,\vec{n}_{IJ},\ \overrightarrow{x_{\hat{L}}x_{\hat{L},j(IJ)}}, \vec{e_z}\right)}{\left(\overrightarrow{x_{\hat{L}}x_{\hat{L},i(IJ)}},\ \overrightarrow{x_{\hat{L}}x_{\hat{L},j(IJ)}},\ \vec{e_z}\right)} \tag{3.11}$$

$$\alpha^{\eta}_{\hat{L},j(IJ)} = \frac{\left(\underline{C}^{\eta}_{\hat{L}}\,\vec{n}_{IJ},\ \overrightarrow{x_{\hat{L}}x_{\hat{L},i(IJ)}}, \vec{e_z}\right)}{\left(\overrightarrow{x_{\hat{L}}x_{\hat{L},i(IJ)}},\ \overrightarrow{x_{\hat{L}}x_{\hat{L},j(IJ)}},\ \vec{e_z}\right)} \tag{3.12}$$

where $(\vec{a}, \vec{b}, \vec{c})$ is the mixed product between vectors $\vec{a}$, $\vec{b}$ and $\vec{c}$. Also, $\vec{e_z}$ is the unit vector normal to the xy plane. By substituting Eq. (3.10) in one diffusive term (e.g. $\underline{C}^{xx}_{\hat{L}}\,\vec{n}_{IJ} \cdot \nabla u_{\hat{L}}$ in Eq. (3.8)) , one gets:

$$\underline{C}^{xx}_{\hat{L}}\,\vec{n}_{IJ} \cdot \nabla u_{\hat{L}} = \alpha^{xx}_{\hat{L},i(IJ)} \nabla u_{\hat{L}} \cdot \overrightarrow{x_{\hat{L}}x_{\hat{L},i(IJ)}} + \alpha^{xx}_{\hat{L},j(IJ)} \nabla u_{\hat{L}} \cdot \overrightarrow{x_{\hat{L}}x_{\hat{L},j(IJ)}} \tag{3.13}$$

Then, by using the following Taylor Series approximations $\nabla u_{\hat{L}} \cdot \overrightarrow{x_{\hat{L}}x_{\hat{L},i(IJ)}} \approx u_{\hat{L},i(IJ)} - u_{\hat{L}}$ and $\nabla u_{\hat{L}} \cdot \overrightarrow{x_{\hat{L}}x_{\hat{L},j(IJ)}} \approx u_{\hat{L},j(IJ)} - u_{\hat{L}}$, Eq. (3.13) becomes:

$$\underline{C}^{xx}_{\hat{L}} \overrightarrow{n}_{IJ} \cdot \nabla u_{\hat{L}} \approx \alpha^{xx}_{\hat{L},i(IJ)} \left(u_{\hat{L},i(IJ)} - u_{\hat{L}} \right) + \alpha^{xx}_{\hat{L},j(IJ)} \left(u_{\hat{L},j(IJ)} - u_{\hat{L}} \right) \tag{3.14}$$

When $|IJ| \to 0$, the approximation in Eq. (3.14) becomes exact. By following similar procedure, one can also define an approximation for the diffusive term in regards to the computational cell $\hat{R}$ as:

$$\underline{C}^{xx}_{\hat{R}} \overrightarrow{n}_{JI} \cdot \nabla u_{\hat{R}} \approx \alpha^{xx}_{\hat{R},i(IJ)} \left(u_{\hat{R}} - u_{\hat{R},i(IJ)} \right) + \alpha^{xx}_{\hat{R},j(IJ)} \left(u_{\hat{R}} - u_{\hat{R},j(IJ)} \right) \tag{3.15}$$

Remark. *Even though the same label, i and j, are used to refer to harmonic points in both $\hat{L}$ and $\hat{R}$ for simplicity sake, the points used in each approximation are not the same. They can share, at most, one point. That only happens if both use the harmonic point belonging to IJ.*

Furthermore, Eq. (3.14) and Eq. (3.15) can be written as:

$$\underline{C}^{xx}_{\hat{L}} \overrightarrow{n}_{IJ} \cdot \nabla u_{\hat{L}} \approx \mathcal{D}^{xx}_{\hat{L},IJ} - \mathcal{A}^{xx}_{\hat{L},IJ} u_{\hat{L}} \tag{3.16}$$

$$\underline{C}^{xx}_{\hat{R}} \overrightarrow{n}_{IJ} \cdot \nabla u_{\hat{R}} \approx \mathcal{A}^{xx}_{\hat{R},IJ} u_{\hat{R}} - \mathcal{D}^{xx}_{\hat{L},IJ} \tag{3.17}$$

where

$$\mathcal{A}^{xx}_{\hat{L},IJ} = \left(\alpha^{xx}_{\hat{L},i(IJ)} + \alpha^{xx}_{\hat{L},j(IJ)} \right), \ \mathcal{A}^{xx}_{\hat{R},IJ} = \left(\alpha^{xx}_{\hat{R},i(IJ)} + \alpha^{xx}_{\hat{R},j(IJ)} \right) \tag{3.18}$$

$$\mathcal{D}^{xx}_{\hat{L},IJ} = \left(\alpha^{xx}_{\hat{L},i(IJ)} u_{\hat{L},i(IJ)} + \alpha^{xx}_{\hat{L},j(IJ)} u_{\hat{L},j(IJ)} \right) \tag{3.19}$$

$$\mathcal{D}^{xx}_{\hat{R},IJ} = \left(\alpha^{xx}_{\hat{R},i(IJ)} u_{\hat{R},i(IJ)} + \alpha^{xx}_{\hat{R},j(IJ)} u_{\hat{R},j(IJ)} \right) \tag{3.20}$$

By applying the MPFA-H method to each diffusive term in Eq. (3.8) and in Eq. (3.9), one can approximate the average stress vectors defined in said equations. The resulting discrete stress is as follows:

$$\overrightarrow{\mathcal{T}}^{\hat{L}}_{IJ} \approx \begin{bmatrix} \mathcal{D}^{xx}_{\hat{L},IJ} - \mathcal{A}^{xx}_{\hat{L},IJ} u_{\hat{L}} + \mathcal{D}^{xy}_{\hat{L},IJ} - \mathcal{A}^{xy}_{\hat{L},IJ} v_{\hat{L}} \\ \mathcal{D}^{yx}_{\hat{L},IJ} - \mathcal{A}^{yx}_{\hat{L},IJ} u_{\hat{L}} + \mathcal{D}^{yy}_{\hat{L},IJ} - \mathcal{A}^{yy}_{\hat{L},IJ} v_{\hat{L}} \end{bmatrix} \tag{3.21}$$

$$\overrightarrow{\mathcal{T}}^{\hat{R}}_{IJ} \approx \begin{bmatrix} \mathcal{A}^{xx}_{\hat{R},IJ} u_{\hat{R}} - \mathcal{D}^{xx}_{\hat{R},IJ} + \mathcal{A}^{xy}_{\hat{R},IJ} v_{\hat{R}} - \mathcal{D}^{xy}_{\hat{R},IJ} \\ \mathcal{A}^{yx}_{\hat{R},IJ} u_{\hat{R}} - \mathcal{D}^{yx}_{\hat{R},IJ} + \mathcal{A}^{yy}_{\hat{R},IJ} v_{\hat{R}} - \mathcal{D}^{yy}_{\hat{R},IJ} \end{bmatrix} \tag{3.22}$$

3.1.1.1 Harmonic Points Interpolation for Linear Elasticity Problems

To construct the Finite Volume Method used in this paper to approximate the Stress Vector, First we must arrive at a definition for the position of said points in the computational cell edge IJ, and a definition for the displacement value in said edge, as a function only of the two computational cell $\hat{L}$ and $\hat{R}$. In (AGÉLAS; EYMARD; HERBIN, 2009), the authors proposed the harmonic points definition for simple diffusive problems. Later, (TEREKHOV; TCHELEPI, 2020a) extended this concept to the Linear Elasticity problem. The procedure used in this paper is based of (TEREKHOV; TCHELEPI, 2020a).

First, each co-normal vector given in Eq. (3.8) and in (3.9) is decomposed in a normal(n superscript) and a tangential(t superscript) component to IJ, as follows:

$$\underline{C}^{\eta}_{\hat{L}} \overrightarrow{n}_{IJ} = \overrightarrow{C^{\eta(n)}_{\hat{L}}} + \overrightarrow{C^{\eta(t)}_{\hat{L}}}, \ \underline{C}^{\eta}_{\hat{R}} \overrightarrow{n}_{JI} = \overrightarrow{C^{\hat{R}(n)}_{\eta}} + \overrightarrow{C^{\hat{R}(t)}_{\eta}} \tag{3.23}$$

with $\eta = xx, xy, yx, yy$. Furthermore, the normal part of the co-normal vector can be written as $\overrightarrow{C^{\eta(n)}_{\hat{L}}} = C^{\eta(n)}_{\hat{L}} \overrightarrow{n}_{IJ}$ with $C^{\eta(n)}_{\hat{L}} = \left(\underline{C}^{\eta}_{\hat{L}} \overrightarrow{n}_{IJ}\right) \cdot \overrightarrow{n}_{IJ}$ and $\overrightarrow{C^{\eta(t)}_{\hat{L}}} = \underline{C}^{\eta}_{\hat{L}} \overrightarrow{n}_{IJ} - \overrightarrow{C^{\eta(n)}_{\hat{L}}}$.

Then, each gradient vector is also split into a normal and tangential components:

$$\nabla u_{\hat{V}} = \nabla u^{(n)}_{\hat{V}} + \nabla u^{(t)}_{\hat{V}}, \ \nabla v_{\hat{V}} = \nabla v^{(n)}_{\hat{V}} + \nabla v^{(t)}_{\hat{V}} \tag{3.24}$$

with $\hat{V} = \hat{L}, \hat{R}$.

To reduce the notation used in the following steps, the following matrices are defined:

$$\underline{C_{\hat{L},IJ}} = \begin{bmatrix} C^{xx(n)}_{\hat{L}} & C^{xy(n)}_{\hat{L}} \\ C^{yx(n)}_{\hat{L}} & C^{xx(n)}_{\hat{L}} \end{bmatrix}, \ \underline{T_{\hat{L},IJ}} = \begin{bmatrix} \left(\overrightarrow{C^{xx(t)}_{\hat{L}}}\right)^{\top} & \left(\overrightarrow{C^{xy(t)}_{\hat{L}}}\right)^{\top} \\ \left(\overrightarrow{C^{yx(t)}_{\hat{L}}}\right)^{\top} & \left(\overrightarrow{C^{yy(t)}_{\hat{L}}}\right)^{\top} \end{bmatrix} \tag{3.25}$$

Remark. *The matrix $\underline{T_{\hat{L},IJ}}$ is a 2x4 matrix, whose components are the transpose of the co-normals tangential parts, since vectors are defined as column matrices.*

By using Eq.(3.25), substituting Eq. (3.23) and Eq. (3.24) into Eq. (3.8) and Eq. (3.9), and doing the proper algebraic manipulation, one can arrive at the following expressions for each cell average stress vector:

$$\overrightarrow{\mathcal{T}_{IJ}^{\hat{L}}} = \underline{C_{\hat{L},IJ}} \begin{bmatrix} |\nabla u_{\hat{L}}^{(n)}| \\ |\nabla v_{\hat{L}}^{(n)}| \end{bmatrix} + \underline{T_{\hat{L},IJ}} \begin{bmatrix} \nabla u_{\hat{L}}^{(t)} \\ \nabla v_{\hat{L}}^{(t)} \end{bmatrix} \tag{3.26}$$

$$\overrightarrow{\mathcal{T}_{IJ}^{\hat{R}}} = \underline{C_{\hat{R},IJ}} \begin{bmatrix} |\nabla u_{\hat{R}}^{(n)}| \\ |\nabla v_{\hat{R}}^{(n)}| \end{bmatrix} + \underline{T_{\hat{R},IJ}} \begin{bmatrix} \nabla u_{\hat{R}}^{(t)} \\ \nabla v_{\hat{R}}^{(t)} \end{bmatrix} \tag{3.27}$$

where $|\overrightarrow{a}|$ represents vector $\overrightarrow{a}$ norm

Furthermore, the Eq. 3.26 and Eq. 3.27 must satisfy the stress vector continuity, $\overrightarrow{\mathcal{T}_{IJ}^{\hat{L}}} = \overrightarrow{\mathcal{T}_{IJ}^{\hat{R}}}$. Therefore:

$$\underline{C_{\hat{L},IJ}} \begin{bmatrix} |\nabla u_{\hat{L}}^{(n)}| \\ |\nabla v_{\hat{L}}^{(n)}| \end{bmatrix} + \underline{T_{\hat{L},IJ}} \begin{bmatrix} \nabla u_{\hat{L}}^{(t)} \\ \nabla v_{\hat{L}}^{(t)} \end{bmatrix} = \underline{C_{\hat{R},IJ}} \begin{bmatrix} |\nabla u_{\hat{R}}^{(n)}| \\ |\nabla v_{\hat{R}}^{(n)}| \end{bmatrix} + \underline{T_{\hat{R},IJ}} \begin{bmatrix} \nabla u_{\hat{R}}^{(t)} \\ \nabla v_{\hat{R}}^{(t)} \end{bmatrix} \tag{3.28}$$

Moreover, the displacement vector continuity can be expressed as:

$$\overrightarrow{u_{\hat{L}}} + \underline{G_{\hat{L}}}\,(x - x_{\hat{L}}) = \overrightarrow{u_{\hat{R}}} - \underline{G_{\hat{R}}}\,(x_{\hat{R}} - x) \tag{3.29}$$

where x is a point belonging to IJ and:

$$\underline{G_{\hat{L}}} = \begin{bmatrix} \frac{\partial u}{\partial x}\Big|_{\hat{L}} & \frac{\partial u}{\partial y}\Big|_{\hat{L}} \\ \frac{\partial v}{\partial x}\Big|_{\hat{L}} & \frac{\partial v}{\partial y}\Big|_{\hat{L}} \end{bmatrix}, \qquad \underline{G_{\hat{R}}} = \begin{bmatrix} \frac{\partial u}{\partial x}\Big|_{\hat{R}} & \frac{\partial u}{\partial y}\Big|_{\hat{R}} \\ \frac{\partial v}{\partial x}\Big|_{\hat{R}} & \frac{\partial v}{\partial y}\Big|_{\hat{R}} \end{bmatrix} \tag{3.30}$$

By defining $h_{\hat{L},IJ}$ and $h_{\hat{R},IJ}$ as the distances between IJ and $x_{\hat{L}}$ and between IJ and $x_{\hat{R}}$ respectively (Fig. 2), points $y_{\hat{L},IJ}$ and $y_{\hat{R},IJ}$ such as $y_{\hat{L},IJ} = x_{\hat{L}} + h_{\hat{L},IJ}\,\overrightarrow{n}_{IJ}$ and $y_{\hat{R},IJ} = x_{\hat{R}} - h_{\hat{R},IJ}\,\overrightarrow{n}_{IJ}$, along with the displacement gradient split defined in Eq. (3.24), Eq. (3.29) can be written as:

$$\overrightarrow{u_{\hat{L}}} + h_{\hat{L},IJ} \begin{bmatrix} |\nabla u_{\hat{L}}^{(n)}| \\ |\nabla v_{\hat{L}}^{(n)}| \end{bmatrix} - \underline{Y_{\hat{L},IJ}} \begin{bmatrix} \nabla u_{\hat{L}}^{(t)} \\ \nabla v_{\hat{L}}^{(t)} \end{bmatrix} = \overrightarrow{u_{\hat{R}}} - h_{\hat{R},IJ} \begin{bmatrix} |\nabla u_{\hat{R}}^{(n)}| \\ |\nabla v_{\hat{R}}^{(n)}| \end{bmatrix} - \underline{Y_{\hat{R},IJ}} \begin{bmatrix} \nabla u_{\hat{R}}^{(t)} \\ \nabla v_{\hat{R}}^{(t)} \end{bmatrix} \tag{3.31}$$

The 2x4 matrices $\underline{Y_{\hat{L},IJ}}$ and $\underline{Y_{\hat{R},IJ}}$ are defined as $\underline{Y_{\hat{L},IJ}} = \left[\underline{I} \otimes y_{\hat{L},IJ}^{\top}\right]$ and $\underline{Y_{\hat{R},IJ}} = \left[\underline{I} \otimes y_{\hat{R},IJ}^{\top}\right]$, where the symbol $\otimes$ represents the Kronecker product.

Figure 2 – Distances from cell edge IJ to cell centers $x_{\hat{L}}$ and $x_{\hat{R}}$

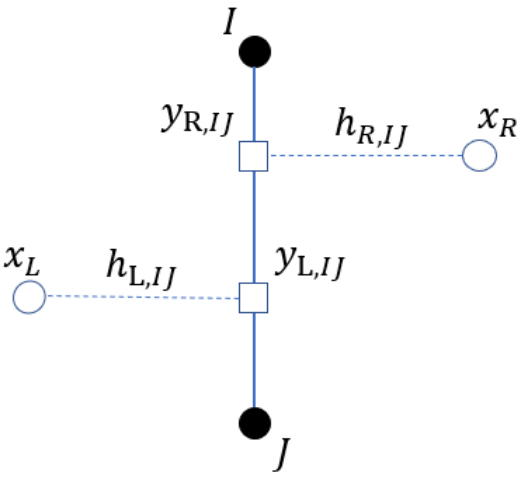

Source: Own authorship (2023)

From the displacement continuity, Eq. (3.29), it follows that $\nabla u_{\hat{L}}^{(t)} = \nabla u_{\hat{R}}^{(t)} = \nabla u^{(t)}$ and $\nabla v_{\hat{L}}^{(t)} = \nabla v_{\hat{R}}^{(t)} = \nabla v^{(t)}$. Thus, we can write Eq. (3.28) as:

$$\begin{bmatrix} |\nabla u_{\hat{R}}^{(n)}| \\ |\nabla v_{\hat{R}}^{(n)}| \end{bmatrix} = \underline{C_{\hat{R},IJ}}^{-1} \left(\underline{C_{\hat{L},IJ}} \begin{bmatrix} |\nabla u_{\hat{L}}^{(n)}| \\ |\nabla v_{\hat{L}}^{(n)}| \end{bmatrix} + \left(\underline{T_{\hat{L},IJ}} - \underline{T_{\hat{R},IJ}} \right) \begin{bmatrix} \nabla u^{(t)} \\ \nabla v^{(t)} \end{bmatrix} \right) \tag{3.32}$$

By substituting Eq. (3.32) into Eq. 3.31, and doing the proper algebraic manipulation, one gets:

$$\overrightarrow{u}_{\hat{L}} - \overrightarrow{u}_{\hat{R}} + \left(h_{\hat{L},IJ}\underline{I} + h_{\hat{R},IJ}\underline{C_{\hat{R},IJ}}^{-1}\underline{C_{\hat{L},IJ}} \right) \begin{bmatrix} |\nabla u_{\hat{L}}^{(n)}| \\ |\nabla v_{\hat{L}}^{(n)}| \end{bmatrix} + \underline{U} \begin{bmatrix} \nabla u^{(t)} \\ \nabla v^{(t)} \end{bmatrix} = 0 \tag{3.33}$$

$$\underline{U} = \left[\underline{Y_{\hat{R},IJ}} - \underline{Y_{\hat{L},IJ}} + h_{\hat{R},IJ}\underline{C_{\hat{R},IJ}}^{-1} \left(\underline{T_{\hat{L},IJ}} - \underline{T_{\hat{R},IJ}} \right) \right] \tag{3.34}$$

Moreover, Eq. 3.33 can be written as:

$$\begin{bmatrix} |\nabla u_{\hat{L}}^{(n)}| \\ |\nabla v_{\hat{L}}^{(n)}| \end{bmatrix} = \left(h_{\hat{L},IJ}\underline{I} + h_{\hat{R},IJ}\underline{C_{\hat{R},IJ}}^{-1}\underline{C_{\hat{L},IJ}} \right)^{-1} \left(\overrightarrow{u}_{\hat{R}} - \overrightarrow{u}_{\hat{L}} - \underline{U} \begin{bmatrix} \nabla u^{(t)} \\ \nabla v^{(t)} \end{bmatrix} \right) \tag{3.35}$$

If $\overrightarrow{u}_{IJ}$ is the displacement evaluated at IJ, the displacement continuity, Eq. 3.29, can be written as:

$$\overrightarrow{u_{\hat{L}}} + \underline{G_{\hat{L}}}\,(x - x_{\hat{L}}) = \overrightarrow{u}_{IJ} \tag{3.36}$$

By introducing the 2x4 matrix $\underline{Y_{IJ}}$, Eq. 3.36 can be written as:

$$\overrightarrow{u_{\hat{L}}} + \left(\underline{Y_{IJ}} - \underline{X_{\hat{L}}}\right) \begin{bmatrix} \nabla u_{\hat{L}} \\ \nabla v_{\hat{L}} \end{bmatrix} = \overrightarrow{u}_{IJ} \tag{3.37}$$

where $\underline{X_{\hat{L}}} = \left[\underline{I} \otimes x_{\hat{L}}^{\top}\right]$. By introducing Eq. 3.24 into Eq. 3.37, one gets:

$$\overrightarrow{u_{\hat{L}}} + h_{\hat{L},IJ} \begin{bmatrix} |\nabla u_{\hat{L}}^{(n)}| \\ |\nabla v_{\hat{L}}^{(n)}| \end{bmatrix} + \left(\underline{Y_{IJ}} - \underline{Y_{\hat{L},IJ}}\right) \begin{bmatrix} \nabla u^{(t)} \\ \nabla v^{(t)} \end{bmatrix} = \overrightarrow{u}_{IJ} \tag{3.38}$$

Furthermore, by introducing the expression for $\left[|\nabla u_{\hat{L}}^{(n)}||\nabla v_{\hat{L}}^{(n)}|\right]^{\top}$, Eq. 3.35, into Eq. 3.38, and by doing some algebraic manipulation, one gets:

$$\overrightarrow{u}_{IJ} = \underline{W_{\hat{L},IJ}}\,\overrightarrow{u}_{\hat{L}} + \underline{W_{\hat{R},IJ}}\,\overrightarrow{u}_{\hat{R}} + \left(\underline{Y_{IJ}} - \underline{Y}\right) \begin{bmatrix} \nabla u^{(t)} \\ \nabla v^{(t)} \end{bmatrix} \tag{3.39}$$

$$\underline{Y} = \underline{W_{\hat{L},IJ} Y_{\hat{L},IJ}} + \underline{W_{\hat{R},IJ} Y_{\hat{R},IJ}} + \underline{W_{IJ}} \left(\underline{T_{\hat{L},IJ}} - \underline{T_{\hat{R},IJ}}\right) \tag{3.40}$$

where:

$$\underline{W_{\hat{L},IJ}} = \left(h_{\hat{L},IJ}\underline{C_{\hat{R},IJ}} + h_{\hat{R},IJ}\underline{C_{\hat{L},IJ}}\right)^{-1} h_{\hat{R},IJ}\underline{C_{\hat{L},IJ}} \tag{3.41}$$

$$\underline{W_{\hat{R},IJ}} = \left(h_{\hat{L},IJ}\underline{C_{\hat{R},IJ}} + h_{\hat{R},IJ}\underline{C_{\hat{L},IJ}}\right)^{-1} h_{\hat{L},IJ}\underline{C_{\hat{R},IJ}} \tag{3.42}$$

$$\underline{W_{IJ}} = h_{\hat{L},IJ} h_{\hat{R},IJ} \left(h_{\hat{L},IJ}\underline{C_{\hat{R},IJ}} + h_{\hat{R},IJ}\underline{C_{\hat{L},IJ}}\right)^{-1} \tag{3.43}$$

The sufficient condition for the displacement $\overrightarrow{u}_{IJ}$ being a function of only $\overrightarrow{u}_{\hat{L}}$ and $\overrightarrow{u}_{\hat{R}}$ is $\underline{Y_{IJ}} = \underline{Y}$. Therefore:

$$\underline{Y_{IJ}} = \underline{W_{\hat{L},IJ} Y_{\hat{L},IJ}} + \underline{W_{\hat{R},IJ} Y_{\hat{R},IJ}} + \underline{W_{IJ}} \left(\underline{T_{\hat{L},IJ}} - \underline{T_{\hat{R},IJ}}\right) \tag{3.44}$$

By using the definitions of $\underline{Y_{\hat{L},IJ}}$, $\underline{Y_{\hat{R},IJ}}$, $y_{\hat{L},IJ}$, $y_{\hat{R},IJ}$, $\underline{T_{\hat{L},IJ}}$, $\underline{T_{\hat{R},IJ}}$ and doing some algebraic manipulation, Eq. 3.44 can be written as:

$$\underline{Y} = \underline{W_{\hat{L},IJ} X_{\hat{L},IJ}} + \underline{W_{\hat{R},IJ} X_{\hat{R},IJ}} + \underline{W_{IJ}} \left(\underline{C_{\hat{L}}} - \underline{C_{\hat{R}}} \right) \tag{3.45}$$

where:

$$\underline{C_{\hat{L}}} = \begin{bmatrix} \left(\underline{C}^{xx}_{\hat{L}} \overrightarrow{n}_{IJ} \right)^{\top} & \left(\underline{C}^{xy}_{\hat{L}} \overrightarrow{n}_{IJ} \right)^{\top} \\ \left(\underline{C}^{yx}_{\hat{L}} \overrightarrow{n}_{IJ} \right)^{\top} & \left(\underline{C}^{yy}_{\hat{L}} \overrightarrow{n}_{IJ} \right)^{\top} \end{bmatrix}, \; \underline{C_{\hat{R}}} = \begin{bmatrix} \left(\underline{C}^{xx}_{\hat{R}} \overrightarrow{n}_{IJ} \right)^{\top} & \left(\underline{C}^{xy}_{\hat{R}} \overrightarrow{n}_{IJ} \right)^{\top} \\ \left(\underline{C}^{yx}_{\hat{R}} \overrightarrow{n}_{IJ} \right)^{\top} & \left(\underline{C}^{yy}_{\hat{R}} \overrightarrow{n}_{IJ} \right)^{\top} \end{bmatrix} \tag{3.46}$$

It's important to notice that Eq. 3.45 is analogous to the definition for harmonic points in (AGÉLAS; EYMARD; HERBIN, 2009; GAO; WU, 2013), but for a vector field $\overrightarrow{u}$ instead of a scalar field p. Moreover, the displacement $\overrightarrow{u}_{IJ}$ is given by:

$$\overrightarrow{u}_{IJ} = \underline{W_{\hat{L},IJ}} \overrightarrow{u}_{\hat{L}} + \underline{W_{\hat{R},IJ}} \overrightarrow{u}_{\hat{R}} \tag{3.47}$$

3.1.1.2 Unique Stress Vector

The unique Stress Vector in IJ, $\overrightarrow{\mathcal{T}}_{IJ}$, is given by a convex combination of the unilateral Stress Vectors $\overrightarrow{\mathcal{T}}^{\hat{L}}_{IJ}$ and $\overrightarrow{\mathcal{T}}^{\hat{R}}_{IJ}$:

$$\overrightarrow{\mathcal{T}}_{IJ} = \underline{W_{\hat{R},IJ}} \overrightarrow{\mathcal{T}}^{\hat{L}}_{IJ} + \underline{W_{\hat{L},IJ}} \overrightarrow{\mathcal{T}}^{\hat{R}}_{IJ} \tag{3.48}$$

Eq. 3.48 satisfies the convex condition because:

$$\underline{W_{\hat{L},IJ}} + \underline{W_{\hat{R},IJ}} = \underline{I} \tag{3.49}$$

3.1.1.3 Treatment of Boundary Conditions

When the computational cell edge IJ belongs to the domain Ω boundary, one of the following may happen:

1. If IJ belongs to a Dirichlet Boundary, the stress vector is unknown, therefore is approximated by the one-sided stress vector, Eq. 3.21, as follows:

$$\overrightarrow{\mathcal{T}}_{IJ} = \overrightarrow{\mathcal{T}}^{\hat{L}}_{IJ} \approx \begin{bmatrix} \mathcal{D}^{xx}_{\hat{L},IJ} - \mathcal{A}^{xx}_{\hat{L},IJ} u_{\hat{L}} + \mathcal{D}^{xy}_{\hat{L},IJ} - \mathcal{A}^{xy}_{\hat{L},IJ} v_{\hat{L}} \\ \mathcal{D}^{yx}_{\hat{L},IJ} - \mathcal{A}^{yx}_{\hat{L},IJ} u_{\hat{L}} + \mathcal{D}^{yy}_{\hat{L},IJ} - \mathcal{A}^{yy}_{\hat{L},IJ} v_{\hat{L}} \end{bmatrix} \tag{3.50}$$

Furthermore, the displacement in the harmonic point pertaining to IJ is known, therefore it has the prescribed value at the boundary. Thus:

$$\begin{bmatrix} u_{\hat{L},i(IJ)} \\ v_{\hat{L},i(IJ)} \end{bmatrix} = \overrightarrow{g}^{u}_{D} \quad or \quad \begin{bmatrix} u_{\hat{L},j(IJ)} \\ v_{\hat{L},j(IJ)} \end{bmatrix} = \overrightarrow{g}^{u}_{D} \tag{3.51}$$

2. If IJ belongs to a Neumann Boundary, the stress is known, therefore is has the prescribed value at said boundary. Thus:

$$\overrightarrow{\mathcal{T}}_{IJ} = \overrightarrow{g}^{u}_{N} \tag{3.52}$$

Furthermore, the displacement in IJ is unknown, therefore it's recovered from the following expression:

$$\begin{bmatrix} \mathcal{D}^{xx}_{\hat{L},IJ} - \mathcal{A}^{xx}_{\hat{L},IJ} u_{\hat{L}} + \mathcal{D}^{xy}_{\hat{L},IJ} - \mathcal{A}^{xy}_{\hat{L},IJ} v_{\hat{L}} \\ \mathcal{D}^{yx}_{\hat{L},IJ} - \mathcal{A}^{yx}_{\hat{L},IJ} u_{\hat{L}} + \mathcal{D}^{yy}_{\hat{L},IJ} - \mathcal{A}^{yy}_{\hat{L},IJ} v_{\hat{L}} \end{bmatrix} = \overrightarrow{g}^{u}_{N} \tag{3.53}$$

Remark. *Accordingly to the boundary conditions of a given problem, Eq.3.53 leads to a local system of equations, with up to 4 unknowns, whose solution yields the interpolation of all harmonic points.*

3.2 Fluid Subsystem

3.2.1 Implicit Euler

The pressure time derivative, first term in Eq. (3.2), in a computational cell $\hat{L}$ is approximated, via the Mean Value Theorem and Finite Difference, as follows:

$$\int_{\Omega_{\hat{L}}} S \frac{\partial p}{\partial t} \, d\Omega_{\hat{L}} \approx \frac{V_{\hat{L}} S_{\hat{L}}}{\Delta t} \left(p^{n+1}_{\hat{L}} - p^{n}_{\hat{L}} \right) \tag{3.54}$$

where $p^{n+1}_{\hat{L}}$ and $p^{n}_{\hat{L}}$ are the pressure values at cell $\hat{L}$ on the respective times t^{n+1} and t^{n}, with $\Delta t = t^{n+1} - t^{n}$. $V_{\hat{L}}$ is the computation cell area. Furthermore, a Backwards Euler scheme is used to evaluate spatial terms. Therefore:

$$\int_{\Omega_{\hat{L}}} S \frac{\partial p}{\partial t} \, d\Omega_{\hat{L}} + \int_{\Omega_{\hat{L}}} \nabla \cdot \overrightarrow{v_t} \, d\Omega_{\hat{L}} \approx \frac{V_{\hat{L}} S_{\hat{L}}}{\Delta t} \left(p^{n+1}_{\hat{L}} - p^{n}_{\hat{L}} \right) + \int_{\Omega_{\hat{L}}} \nabla \cdot \overrightarrow{v_t} \, d\Omega_{\hat{L}} \Bigg|^{n+1} \tag{3.55}$$

It is possible to trace a parallel between the fluid terms in Eq. (2.25) and a general diffusion equation. For the 1D case:

$$\frac{\partial p}{\partial t} = \frac{k}{S\mu}\frac{\partial^2 p}{\partial x^2} \tag{3.56}$$

$$\frac{\partial \theta}{\partial t} = \omega\frac{\partial^2 \theta}{\partial x^2} \tag{3.57}$$

where $\theta = p$ and $\omega = k/S\mu$. In the context of a general diffusion problem, θ is the unknown variable(e.g. Temperature, Pressure) and ω is a diffusion coefficient. In the context of Poroelasticity, more precisely in Soil Mechanics, the quantity $\omega = k/S\mu$ is known as the consolidation coefficient (WANG, 2000). This similarity was first noted by Terzaghi himself. The time evolution of the pressure profile for Terzaghi's experiment was the same as the analogous thermal problem of a sudden step change (WANG, 2000).

In numerical simulations of diffusion problems, the stability of a numerical scheme is related to the Fourier's number (HENSEN; NAKHI, 1994):

$$Fo_{\hat{L}} = \omega_{\hat{L}}\frac{\Delta t}{h^2_{\hat{L}}} \tag{3.58}$$

$h_{\hat{L}}$ is cell $\hat{L}$ characteristic length, and $\omega_{\hat{L}}$ is cell $\hat{L}$ diffusive coefficient. The value of Fo that corresponds to the limit of stability in a diffusion problem is give by:

$$Fo = \frac{1}{4(1-d)} \tag{3.59}$$

where $d = 0$ for the Forwards Euler scheme, $d = 0.5$ for the Crank-Nicholson scheme and $d = 1$ for the Backwards Euler scheme. Thus, the Backwards Euler scheme is unconditionally stable. Fourier's number establishes a relationship between time step and mesh resolution, which will be evident in section

3.2.2 Multipoint Flux Approximation using Harmonic Points (MPFA-H)

The Darcy Flux term (second term in Eq. (3.2)) is approximated using the original MPFA-H defined in (GAO; WU, 2014; CONTRERAS et al., 2017). First we use The Divergence theorem as follows:

$$\int_{\Omega_{\hat{L}}} \nabla \cdot \overrightarrow{v_t}\ d\Omega_{\hat{L}} = \int_{\Gamma_{\hat{L}}} \overrightarrow{v_t} \cdot \overrightarrow{n}\ d\Gamma_{\hat{L}} = \sum_{IJ\in\Gamma_{\hat{L}}} \int_{IJ} \overrightarrow{v_t} \cdot \overrightarrow{n}\ ds \tag{3.60}$$

Next, we use the Mean Value theorem to approximate the Darcy Flux on the cell edge IJ. Furthermore, after substituting Darcy's Law, Eq (2.26), in the result, one gets:

$$\int_{IJ} \overrightarrow{v_t} \cdot \overrightarrow{n}\ ds \approx |IJ| \overrightarrow{v_t} \cdot \overrightarrow{n}_{IJ} = |IJ|(-\frac{1}{\mu}\underline{K}\nabla p) \cdot \overrightarrow{n}_{IJ} \tag{3.61}$$

Furthermore one can write the unilateral flux in regards to the cells $\hat{L}$ and $\hat{R}$ as:

$$\overrightarrow{v_t}^{\hat{L}} \cdot \overrightarrow{n}_{IJ} = -\frac{1}{\mu}\underline{K_{\hat{L}}^{\top}}\nabla p \cdot \overrightarrow{n}_{IJ} = -\frac{1}{\mu}\nabla p \cdot \underline{K_{\hat{L}}^{\top}}\overrightarrow{n}_{IJ} \tag{3.62}$$

$$\overrightarrow{v_t}^{\hat{R}} \cdot \overrightarrow{n}_{JI} = -\frac{1}{\mu}\underline{K_{\hat{R}}^{\top}}\nabla p \cdot \overrightarrow{n}_{JI} = -\frac{1}{\mu}\nabla p \cdot \underline{K_{\hat{R}}^{\top}}\overrightarrow{n}_{JI} \tag{3.63}$$

where $\underline{K_{\hat{L}}^{\top}}\overrightarrow{n}_{IJ}$ and $\underline{K_{\hat{R}}^{\top}}\overrightarrow{n}_{JI}$ are co-normal vectors corresponding to the diffusion coefficients $\underline{K_{\hat{L}}}$ and $\underline{K_{\hat{R}}}$. Similarly to Eq. (3.10), each co-normal vector is decomposed as follows:

$$\underline{K_{\hat{L}}^{\top}}\overrightarrow{n}_{IJ} = \alpha^K_{\hat{L},i(IJ)}\overrightarrow{x_{\hat{L}}x_{\hat{L},i(IJ)}} + \alpha^K_{\hat{L},j(IJ)}\overrightarrow{x_{\hat{L}}x_{\hat{L},j(IJ)}} \tag{3.64}$$

where:

$$\alpha^K_{\hat{L},i(IJ)} = \frac{\left(\underline{K_{\hat{L}}^{\top}}\overrightarrow{n}_{IJ},\ \overrightarrow{x_{\hat{L}}x_{\hat{L},j(IJ)}}, \overrightarrow{e_z}\right)}{\left(\overrightarrow{x_{\hat{L}}x_{\hat{L},i(IJ)}},\ \overrightarrow{x_{\hat{L}}x_{\hat{L},j(IJ)}},\ \overrightarrow{e_z}\right)} \tag{3.65}$$

$$\alpha^K_{\hat{L},j(IJ)} = \frac{\left(\underline{K_{\hat{L}}^{\top}}\overrightarrow{n}_{IJ},\ \overrightarrow{x_{\hat{L}}x_{\hat{L},i(IJ)}}, \overrightarrow{e_z}\right)}{\left(\overrightarrow{x_{\hat{L}}x_{\hat{L},i(IJ)}},\ \overrightarrow{x_{\hat{L}}x_{\hat{L},j(IJ)}},\ \overrightarrow{e_z}\right)} \tag{3.66}$$

Remark. *Due to the use of shared notation, $x_{\hat{L},l(IJ)}$ and $x_{\hat{L},j(IJ)}$, the reader can infer that the points used in the stress and flux approximations are the same, which may or may not be the case. The Linear Elasticity problem has its set of harmonic points, corresponding to $\underline{\boldsymbol{C}}$, and those points come in pairs for each cell edge IJ. Meanwhile Darcy Flow problem has a different set of harmonic points, now corresponding to $\underline{K}$, which are unique for each edge IJ.*

Then, by substituting Eq. 3.64 into the diffusive term, $\nabla p \cdot \underline{K_{\hat{L}}^{\top}}\overrightarrow{n}_{IJ}$, in Eq. 3.62 one gets:

$$\nabla p \cdot \underline{K_{\hat{L}}^{\top}}\overrightarrow{n}_{IJ} = \alpha^K_{\hat{L},i(IJ)}\nabla p \cdot \overrightarrow{x_{\hat{L}}x_{\hat{L},i(IJ)}} + \alpha^K_{\hat{L},j(IJ)}\nabla p \cdot \overrightarrow{x_{\hat{L}}x_{\hat{L},j(IJ)}} \tag{3.67}$$

By doing a Taylor Series expansion of ∇p in the directions of $\overrightarrow{x_{\hat{L}}x_{\hat{L},i(IJ)}}$ and $\overrightarrow{x_{\hat{L}}x_{\hat{L},j(IJ)}}$, one can approximate the Darcy flux as:

$$\overrightarrow{v_t}^{\hat{L}} \cdot \overrightarrow{n}_{IJ} \approx \frac{1}{\mu}\left[\alpha^K_{\hat{L},i(IJ)}\left(p_{\hat{L}} - p_{\hat{L},i(IJ)}\right) + \alpha^K_{\hat{L},j(IJ)}\left(p_{\hat{L}} - p_{\hat{L},j(IJ)}\right)\right] \tag{3.68}$$

Similarly for the cell $\hat{R}$:

$$\overrightarrow{v_t}^{\hat{R}} \cdot \overrightarrow{n}_{JI} \approx \frac{1}{\mu}\left[\alpha^K_{\hat{R},i(IJ)}\left(p_{\hat{R},i(IJ)} - p_{\hat{R}}\right) + \alpha^K_{\hat{R},j(IJ)}\left(p_{\hat{R},j(IJ)} - p_{\hat{L}}\right)\right] \tag{3.69}$$

Moreover, each one sided flux can be written as:

$$\overrightarrow{v_t}^{\hat{L}} \cdot \overrightarrow{n}_{IJ} \approx \frac{1}{\mu}\left(\mathcal{A}^K_{\hat{L},IJ}p_{\hat{L}} - \mathcal{D}^K_{\hat{L},IJ}\right),\ \overrightarrow{v_t}^{\hat{R}} \cdot \overrightarrow{n}_{JI} \approx \frac{1}{\mu}\left(\mathcal{D}^K_{\hat{R},IJ} - \mathcal{A}^K_{\hat{R},IJ}p_{\hat{R}}\right) \tag{3.70}$$

where:

$$\mathcal{A}^K_{\hat{L},IJ} = \left(\alpha^K_{\hat{L},i(IJ)} + \alpha^K_{\hat{L},j(IJ)}\right),\ \mathcal{A}^K_{\hat{R},IJ} = \left(\alpha^K_{\hat{R},i(IJ)} + \alpha^K_{\hat{R},j(IJ)}\right) \tag{3.71}$$

$$\mathcal{D}^K_{\hat{L},IJ} = \left(\alpha^K_{\hat{L},i(IJ)}p_{\hat{L},i(IJ)} + \alpha^K_{\hat{L},j(IJ)}p_{\hat{L},j(IJ)}\right) \tag{3.72}$$

$$\mathcal{D}^K_{\hat{R},IJ} = \left(\alpha^K_{\hat{R},i(IJ)}p_{\hat{R},i(IJ)} + \alpha^K_{\hat{R},j(IJ)}p_{\hat{R},j(IJ)}\right) \tag{3.73}$$

3.2.2.1 Harmonic Points Interpolation for general diffusion problems

As previously mentioned, in (AGÉLAS; EYMARD; HERBIN, 2009), the authors proposed the harmonic points definition for simple diffusive problems with a sketch proof for the equations. Latter, in (GAO; WU, 2013), the authors proposed a proper derivation for the Harmonic Points, which is where the methodology used in the present work is based upon.

First, similarly to Eq. (3.23), each co-normal vector is decomposed in a normal and a tangential part, as follows:

$$\underline{K^K_{\hat{L}}}^{\top}\overrightarrow{n}_{IJ} = a^K_{\hat{L}}\left(y_{IJ} - x_{\hat{L}}\right) + b^K_{\hat{L}}\overrightarrow{IJ},\ \underline{K^K_{\hat{R}}}^{\top}\overrightarrow{n}_{JI} = a^K_{\hat{R}}\left(y_{IJ} - x_{\hat{R}}\right) - b^K_{\hat{R}}\overrightarrow{IJ} \tag{3.74}$$

where:

$$a_{\hat{L}}^{K} = \frac{K_{\hat{L}}^{(n)}}{h_{\hat{L},IJ}},\ a_{\hat{R}}^{K} = \frac{K_{\hat{R}}^{(n)}}{h_{\hat{R},IJ}},\ K_{\hat{L}}^{(n)} = \overrightarrow{n}_{IJ}^{\top} \underline{K_{\hat{L}}}\, \overrightarrow{n}_{IJ},\ K_{\hat{R}}^{(n)} = \overrightarrow{n}_{JI}^{\top} \underline{K_{\hat{R}}}\, \overrightarrow{n}_{JI} \tag{3.75}$$

Furthermore, y_{IJ} is a point in the cell edge IJ. In order for y_{IJ} to be a Harmonic Point, the pressure p_{IJ} at y_{IJ} should be a combination of only the pressures $p_{\hat{L}}$ and $p_{\hat{R}}$ at the adjacent cells $\hat{L}$ and $\hat{R}$. By substituting Eq. (3.74) into Eq. 3.62 and Eq. 3.63, we get for the each cell:

$$\nabla p \cdot \underline{K_{\hat{L}}^{\top}} \overrightarrow{n}_{IJ} = a_{\hat{L}}^{K} \nabla p \cdot (y_{IJ} - x_{\hat{L}}) + b_{\hat{L}}^{K} \nabla p \cdot \overrightarrow{IJ} \tag{3.76}$$

$$\nabla p \cdot \underline{K_{\hat{R}}^{\top}} \overrightarrow{n}_{JI} = a_{\hat{R}}^{K} \nabla p \cdot (y_{IJ} - x_{\hat{L}}) - b_{\hat{R}}^{K} \nabla p \cdot \overrightarrow{IJ} \tag{3.77}$$

Due to flux continuity through IJ, $\nabla p \cdot \underline{K_{\hat{L}}^{\top}} \overrightarrow{n}_{IJ} = -\nabla p \cdot \underline{K_{\hat{R}}^{\top}} \overrightarrow{n}_{JI}$. Thus:

$$a_{\hat{L}}^{K} \nabla p \cdot (y_{IJ} - x_{\hat{L}}) + b_{\hat{L}}^{K} \nabla p \cdot \overrightarrow{IJ} = -a_{\hat{R}}^{K} \nabla p \cdot (y_{IJ} - x_{\hat{R}}) + b_{\hat{R}}^{K} \nabla p \cdot \overrightarrow{IJ} \tag{3.78}$$

A sufficient condition for p_{IJ} being a function of only $p_{\hat{L}}$ and $p_{\hat{R}}$ is $b_{\hat{L}}^{K} = b_{\hat{R}}^{K}$. That implies:

$$a_{\hat{L}}^{K} \nabla p \cdot (y_{IJ} - x_{\hat{L}}) = -a_{\hat{R}}^{K} \nabla p \cdot (y_{IJ} - x_{\hat{R}}) \tag{3.79}$$

The terms $\nabla p \cdot (y_{IJ} - x_{\hat{L}})$ and $\nabla p \cdot (y_{IJ} - x_{\hat{R}})$ can be approximated using a Taylor Series expansion as $\nabla p \cdot (y_{IJ} - x_{\hat{L}}) \approx p_{IJ} - p_{\hat{L}}$ and $\nabla p \cdot (y_{IJ} - x_{\hat{R}}) \approx p_{IJ} - p_{\hat{R}}$. Using said approximation, Eq. 3.79 can be written as:

$$a_{\hat{L}}^{K} (p_{IJ} - p_{\hat{L}}) = -a_{\hat{R}}^{K} (p_{IJ} - p_{\hat{R}}) \tag{3.80}$$

By isolating p_{IJ} from Eq. 3.80, one get the expression for the pressure value p_{IJ} in the harmonic point y_{IJ} as:

$$p_{IJ} = \frac{a_{\hat{L}}^{K} p_{\hat{L}} + a_{\hat{R}}^{K} p_{\hat{R}}}{a_{\hat{L}}^{K} + a_{\hat{R}}^{K}} \tag{3.81}$$

Furthermore, Eq. 3.81 can be written as:

$$p_{IJ} = w^K_{\hat{L},IJ} p_{\hat{L}} + w^K_{\hat{R},IJ} p_{\hat{R}} \tag{3.82}$$

where:

$$w^K_{\hat{L},IJ} = \frac{a^K_{\hat{L}}}{a^K_{\hat{L}} + a^K_{\hat{R}}},\ w^K_{\hat{R},IJ} = \frac{a^K_{\hat{R}}}{a^K_{\hat{L}} + a^K_{\hat{R}}} \tag{3.83}$$

By substituting Eq. (3.75) into Eq. (3.83) and doing the necessary algebraic manipulations, one gets:

$$w^K_{\hat{L},IJ} = \frac{h_{\hat{R},IJ} K^{(n)}_{\hat{L}}}{h_{\hat{R},IJ} K^{(n)}_{\hat{L}} + h_{\hat{L},IJ} K^{(n)}_{\hat{R}}},\ w^K_{\hat{R},IJ} = \frac{h_{\hat{L},IJ} K^{(n)}_{\hat{R}}}{h_{\hat{R},IJ} K^{(n)}_{\hat{L}} + h_{\hat{L},IJ} K^{(n)}_{\hat{R}}} \tag{3.84}$$

Its worth noticing that $w^K_{\hat{L},IJ} + w^K_{\hat{R},IJ} = 1$. In order to compute the coordinates for y_{IJ}, first we add $\underline{K^\top_{\hat{R}}} \overrightarrow{n}_{IJ}$ to $\underline{K^\top_{\hat{L}}} \overrightarrow{n}_{JI}$ defined in Eq. (3.74):

$$\left(\underline{K^\top_{\hat{L}}} - \underline{K^\top_{\hat{R}}}\right) \overrightarrow{n}_{IJ} = \left(a^K_{\hat{L}} + a^K_{\hat{R}}\right) y_{IJ} - a^K_{\hat{L}} x_{\hat{L}} - a^K_{\hat{R}} x_{\hat{R}} + \left(b^K_{\hat{R}} - b^K_{\hat{L}}\right) \overrightarrow{IJ} \tag{3.85}$$

Since $b^K_{\hat{L}} = b^K_{\hat{R}}$, one can extract from Eq. (3.85) the expression for the Harmonic Point y_{IJ} pertaining to the edge IJ as:

$$y_{IJ} = \frac{a^K_{\hat{L}} x_{\hat{L}} + a^K_{\hat{R}} x_{\hat{R}} + \left(\underline{K^\top_{\hat{L}}} - \underline{K^\top_{\hat{R}}}\right) \overrightarrow{n}_{IJ}}{a^K_{\hat{L}} + a^K_{\hat{R}}} \tag{3.86}$$

By substituting Eq. (3.75) into Eq. ((3.86)) and doing the necessary algebraic manipulations, one gets:

$$y_{IJ} = \frac{h_{\hat{R},IJ} K^{(n)}_{\hat{L}} x_{\hat{L}} + h_{\hat{L},IJ} K^{(n)}_{\hat{R}} x_{\hat{R}} + h_{\hat{L},IJ} h_{\hat{R},IJ} \left(\underline{K^\top_{\hat{L}}} - \underline{K^\top_{\hat{R}}}\right) \overrightarrow{n}_{IJ}}{h_{\hat{R},IJ} K^{(n)}_{\hat{L}} + h_{\hat{L},IJ} K^{(n)}_{\hat{R}}} \tag{3.87}$$

3.2.2.2 Unique Flux Construction

The unique flux through the cell edge IJ is constructed via a convex combination using the one sided flux definitions in Eq. 3.70 and the weights defined in Eq. 3.83 as such:

$$\overrightarrow{v_t} \cdot \overrightarrow{n}_{IJ} = w^K_{\hat{R},IJ} \overrightarrow{v_t}^{\hat{L}} \cdot \overrightarrow{n}_{IJ} + w^K_{\hat{L},IJ} \overrightarrow{v_t}^{\hat{R}} \cdot \overrightarrow{n}_{IJ} \tag{3.88}$$

3.2.2.3 Treatment of Boundary Conditions

When the computational cell edge IJ belongs to the domain Ω boundary, one of the following may happen:

1. If IJ belongs to a Dirichlet Boundary, the flux is unknown, therefore is approximated by the one-sided flux, Eq. 3.68, as follows:

$$\overrightarrow{v_t} \cdot \overrightarrow{n}_{IJ} = \overrightarrow{v_t}^{\hat{L}} \cdot \overrightarrow{n}_{IJ} \approx \frac{1}{\mu} \left(\mathcal{A}^K_{\hat{L},IJ} p_{\hat{L}} - \mathcal{D}^K_{\hat{L},IJ} \right) \tag{3.89}$$

Furthermore, the pressure in the harmonic point pertaining to IJ is known, therefore it has the prescribed value at the boundary. Thus:

$$p_{\hat{L},i(IJ)} = g^p_D \quad or \quad p_{\hat{L},j(IJ)} = g^p_D \tag{3.90}$$

2. If IJ belongs to a Neumann Boundary, the flux is known, therefore is has the prescribed value at said boundary. Thus:

$$\overrightarrow{v_t} \cdot \overrightarrow{n}_{IJ} = g^p_N \tag{3.91}$$

Furthermore, the pressure in IJ is unknown, therefore it's recovered from the following expression:

$$\frac{1}{\mu} \left(\alpha^K_{\hat{L},i(IJ)} \left(p_{\hat{L}} - p_{\hat{L},i(IJ)} \right) + \alpha^K_{\hat{L},j(IJ)} \left(p_{\hat{L}} - p_{\hat{L},j(IJ)} \right) \right) = g^p_N \tag{3.92}$$

Remark. *If both $p_{\hat{L},i(IJ)}$ and $p_{\hat{L},j(IJ)}$ in Eq.3.92 belong to a edge in the Neumann Boundary, this leads to a local system of equations whose solution yields the interpolation of both harmonic points.*

3.3 Coupling Terms

3.3.1 Pressure Gradient

The pressure gradient, second term in Eq. (3.1), is approximated via the Divergence Theorem and the Mean Value Theorem as follows:

$$\int_{\Omega_{\hat{L}}} \alpha \nabla p \, d\Omega_{\hat{L}} = \alpha_{\hat{L}} \int_{\Gamma_{\hat{L}}} p \overrightarrow{n} \, d\Gamma_{\hat{L}} = \alpha_{\hat{L}} \sum_{IJ \in \Gamma_{\hat{L}}} \int_{IJ} p \overrightarrow{n}_{IJ} \, ds \approx$$

$$\approx \alpha_{\hat{L}} \sum_{IJ \in \Gamma_{\hat{L}}} |IJ| p_{IJ} \overrightarrow{n}_{IJ} \tag{3.93}$$

where p_{IJ} is the pressure value in IJ. In the present work, p_{IJ} is interpolated via the Harmonic points interpolation.

3.3.2 Solid Velocity

This subsection is dedicated to the discretization of solid velocity term, third term in Eq. (3.2). Since Integration and Differenciation are linear operators their order can be swapped, leading to:

$$\int_{\Omega_{\hat{L}}} \frac{\partial \varepsilon_v}{\partial t}\, d\Omega_{\hat{L}} = \frac{\partial}{\partial t}\int_{\Omega_{\hat{L}}} \varepsilon_v\, d\Omega_{\hat{L}} = \frac{\partial}{\partial t}\int_{\Omega_{\hat{L}}} \nabla \cdot \overrightarrow{u}\, d\Omega_{\hat{L}} = \frac{\partial E_{\hat{L}}}{\partial t} \tag{3.94}$$

where $E_{\hat{L}} = \int_{\Omega_{\hat{L}}} \nabla \cdot \overrightarrow{u}\, d\Omega_{\hat{L}}$. A first order finite difference method is used to approximate $E_{\hat{L}}$ time derivative, as follows:

$$\frac{\partial E_{\hat{L}}}{\partial t} = \frac{E_{\hat{L}}^{n+1} - E_{\hat{L}}^{n}}{\Delta t} \tag{3.95}$$

where the superscript n indicates the value of $E_{\hat{L}}$ at the time level t, and the superscript $n+1$ indicates the value of $E_{\hat{L}}$ at the time level $t + \Delta t$. Furthermore, $E_{\hat{L}}$ can be computed, using the Divergence Theorem, with the following expression:

$$E_{\hat{L}} = \int_{\Omega_{\hat{L}}} \nabla \cdot \overrightarrow{u}\, d\Omega_{\hat{L}} = \int_{\Gamma_{\hat{L}}} \overrightarrow{u} \cdot \overrightarrow{n}\, d\Gamma_{\hat{L}} = \sum_{IJ \in \Gamma_{\hat{L}}} \int_{IJ} \overrightarrow{u} \cdot \overrightarrow{n}\, ds \tag{3.96}$$

where $\Gamma_{\hat{L}}$ is the computational cell boundary, and IJ is a edge belonging to said boundary, since the computational cells are star-shaped polygons. $\overrightarrow{n}$ is the unit normal vector to IJ Furthermore, the integral over IJ defined in Equation 3.96 is approximated by the Mean Value Theorem, as follows:

$$\int_{IJ} \overrightarrow{u} \cdot \overrightarrow{n}\, ds \approx |IJ| \overrightarrow{u}_{IJ} \cdot \overrightarrow{n}_{IJ} \tag{3.97}$$

with $|IJ|$ being the size of IJ, $\overrightarrow{u}_{IJ}$ and $\overrightarrow{n}_{IJ}$ being, respectively, the displacement and unit normal vectors pertaining to the computational edge IJ.

The scheme proposed in this work uses a cell-center, co-located variable arrangement with a the same order of approximation for the Linear Momentum and Mass Conservation Equations. This leads to a violation of the Ladyzhenskaya–Babuška–Brezzi (LBB for short) condition, which incurs in non-physical oscillations in the solution field. This problem is commonly known as "Even-Odd decoupling". In order to work around the LBB condition, the edge velocity $\overrightarrow{u}_{IJ}$ is computed using a interpolation method based of the Modified Rhie-Chow interpolation (ZHANG; ZHAO; BAYYUK, 2014), to increase the coupling strength between the variables p and $\overrightarrow{u}$.

3.3.2.1 Modified Rhie-Chow interpolation

The first step to the Modified Rhie-Chow interpolation (ZHANG; ZHAO; BAYYUK, 2014) is to write Equation (2.15) for the computational edge IJ as if it was a center of a computational cell in a staggered grid. By neglecting the term $(\lambda + G)\,\nabla\,(\nabla \cdot \overrightarrow{u})$, Equation (2.15) can be written as:

$$G\nabla \cdot (\nabla \overrightarrow{u}) = \alpha \nabla p \tag{3.98}$$

Remark. *The suppression of* $(\lambda + G)\,\nabla\,(\nabla \cdot \overrightarrow{u})$ *is a reasonable approximation, that is done only in the interpolation step. The governing equation for the Solid Subsystem still is Equation* (2.5) *along with Equation* (2.8)*.*

The diffusive term in Equation (3.98), under a finite volume framework, is approximated using a standard MPFA-H method (GAO; WU, 2014). First we apply the Divergence Theorem to the Integral formulation of Equation (3.98). For the u component of the displacement vector, one can write:

$$\int_{\Omega_{\hat{L}}} \underline{G}\nabla \cdot (\nabla u)\ d\Omega_{\hat{L}} = \int_{\Gamma_{\hat{L}}} \underline{G}\nabla u \cdot \overrightarrow{n}\ d\Gamma_{\hat{L}} = \sum_{IJ \in \Gamma_{\hat{L}}} \int_{IJ} \underline{G}\nabla u \cdot \overrightarrow{n}\ ds \tag{3.99}$$

where $\underline{G} = G\underline{I}$. Furthermore, the integral over IJ defined in Equation 3.99 can be approximated via the Mean Value Theorem as:

$$\int_{IJ} \underline{G}\nabla u \cdot \overrightarrow{n}\ ds \approx |IJ| \underline{G}\nabla u \cdot \overrightarrow{n}_{IJ} = |IJ| \nabla u \cdot \underline{G}\overrightarrow{n}_{IJ} \tag{3.100}$$

The diffusive term $\nabla u \cdot \underline{G}\overrightarrow{n}_{IJ}$ is now written as a convex combination of the one sided diffusive terms $\nabla u \cdot \underline{G_{\hat{L}}}\,\overrightarrow{n}_{IJ}$ and $\nabla u \cdot \underline{G_{\hat{R}}}\,\overrightarrow{n}_{JI}$ as follows:

$$\nabla u \cdot \underline{G}\overrightarrow{n}_{IJ} \approx w^G_{\hat{R},IJ} \nabla u \cdot \underline{G_{\hat{L}}}\,\overrightarrow{n}_{IJ} + w^G_{\hat{L},IJ} \nabla u \cdot \underline{G_{\hat{R}}}\,\overrightarrow{n}_{JI} \tag{3.101}$$

where:

$$w^G_{\hat{L},IJ} = \frac{h_{\hat{R},IJ} G^{(n)}_{\hat{L}}}{h_{\hat{R},IJ} G^{(n)}_{\hat{L}} + h_{\hat{L},IJ} G^{(n)}_{\hat{R}}},\ w^G_{\hat{R},IJ} = \frac{h_{\hat{L},IJ} G^{(n)}_{\hat{R}}}{h_{\hat{R},IJ} G^{(n)}_{\hat{L}} + h_{\hat{L},IJ} G^{(n)}_{\hat{R}}} \tag{3.102}$$

and

$$G_{\hat{L}}^{(n)} = \overrightarrow{n}_{IJ}^{\top} \underline{G_{\hat{L}}} \overrightarrow{n}_{IJ},\ G_{\hat{R}}^{(n)} = \overrightarrow{n}_{JI}^{\top} \underline{G_{\hat{R}}} \overrightarrow{n}_{JI} \tag{3.103}$$

Furthermore, each one sided diffusive term can be approximated as follows:

$$\nabla u \cdot \underline{G_{\hat{L}}} \overrightarrow{n}_{IJ} \approx \alpha_{\hat{L},i(IJ)}^{G} \left(u_{\hat{L},i(IJ)} - u_{\hat{L}} \right) + \alpha_{\hat{L},j(IJ)}^{G} \left(u_{\hat{L},j(IJ)} - u_{\hat{L}} \right) \tag{3.104}$$

$$\nabla u \cdot \underline{G_{\hat{R}}} \overrightarrow{n}_{JI} \approx \alpha_{\hat{R},i(IJ)}^{G} \left(u_{\hat{R}} - u_{\hat{R},i(IJ)} \right) + \alpha_{\hat{R},j(IJ)}^{G} \left(u_{\hat{R}} - u_{\hat{R},j(IJ)} \right) \tag{3.105}$$

where:

$$\alpha_{\hat{L},i(IJ)}^{G} = \frac{\left(\underline{G_{\hat{L}}} \overrightarrow{n}_{IJ},\ \overrightarrow{x_{\hat{L}} x_{\hat{L},j(IJ)}}, \overrightarrow{e_z} \right)}{\left(\overrightarrow{x_{\hat{L}} x_{\hat{L},i(IJ)}},\ \overrightarrow{x_{\hat{L}} x_{\hat{L},j(IJ)}},\ \overrightarrow{e_z} \right)} \tag{3.106}$$

$$\alpha_{\hat{L},j(IJ)}^{G} = \frac{\left(\underline{G_{\hat{L}}} \overrightarrow{n}_{IJ},\ \overrightarrow{x_{\hat{L}} x_{\hat{L},i(IJ)}}, \overrightarrow{e_z} \right)}{\left(\overrightarrow{x_{\hat{L}} x_{\hat{L},i(IJ)}},\ \overrightarrow{x_{\hat{L}} x_{\hat{L},j(IJ)}},\ \overrightarrow{e_z} \right)} \tag{3.107}$$

$$\alpha_{\hat{R},j(IJ)}^{G} = \frac{\left(\underline{G_{\hat{R}}} \overrightarrow{n}_{JI},\ \overrightarrow{x_{\hat{R}} x_{\hat{R},i(IJ)}}, \overrightarrow{e_z} \right)}{\left(\overrightarrow{x_{\hat{R}} x_{\hat{R},i(IJ)}},\ \overrightarrow{x_{\hat{R}} x_{\hat{R},j(IJ)}},\ \overrightarrow{e_z} \right)} \tag{3.108}$$

$$\alpha_{\hat{R},i(IJ)}^{G} = \frac{\left(\underline{G_{\hat{R}}} \overrightarrow{n}_{JI},\ \overrightarrow{x_{\hat{R}} x_{\hat{R},j(IJ)}}, \overrightarrow{e_z} \right)}{\left(\overrightarrow{x_{\hat{R}} x_{\hat{R},i(IJ)}},\ \overrightarrow{x_{\hat{R}} x_{\hat{R},j(IJ)}},\ \overrightarrow{e_z} \right)} \tag{3.109}$$

Similar to Eq. 3.68 and Eq. 3.69, both Eq. 3.104 and Eq. 3.105 can be written as:

$$\nabla u \cdot \underline{G_{\hat{L}}} \overrightarrow{n}_{IJ} \approx \mathcal{D}_{\hat{L},IJ}^{G,u} - \mathcal{A}_{\hat{L},IJ}^{G} u_{\hat{L}},\ \nabla u \cdot \underline{G_{\hat{R}}} \overrightarrow{n}_{IJ} \approx \mathcal{A}_{\hat{R},IJ}^{G} u_{\hat{L}} - \mathcal{D}_{\hat{R},IJ}^{G,u} \tag{3.110}$$

where:

$$\mathcal{A}_{\hat{L},IJ}^{G} = \left(\alpha_{\hat{L},i(IJ)}^{G} + \alpha_{\hat{L},j(IJ)}^{G} \right),\ \mathcal{A}_{\hat{R},IJ}^{G} = \left(\alpha_{\hat{R},i(IJ)}^{G} + \alpha_{\hat{R},j(IJ)}^{G} \right) \tag{3.111}$$

$$\mathcal{D}_{\hat{L},IJ}^{G,u} = \left(\alpha_{\hat{L},i(IJ)}^{G} u_{\hat{L},i(IJ)} + \alpha_{\hat{L},j(IJ)}^{G} u_{\hat{L},j(IJ)} \right) \tag{3.112}$$

$$\mathcal{D}^{G,u}_{\hat{R},IJ} = \left(\alpha^{G}_{\hat{R},i(IJ)} u_{\hat{R},i(IJ)} + \alpha^{G}_{\hat{R},j(IJ)} u_{\hat{R},j(IJ)}\right) \tag{3.113}$$

and $u_{\hat{L},i(IJ)} = u_{\hat{R},i(IJ)} = w^{G}_{\hat{L},IJ} u_{\hat{L}} + w^{G}_{\hat{R},IJ} u_{\hat{R}}$, $u_{\hat{L},j(IJ)} = w^{G}_{\hat{L},HI} u_{\hat{L}} + w^{G}_{\hat{M},HI} u_{\hat{M}}$ and $u_{\hat{L},j(IJ)} = w^{G}_{\hat{L},JK} u_{\hat{L}} + w^{G}_{\hat{N},JK} u_{\hat{N}}$. HI and JK are the edges belonging to $\hat{L}$ and $\hat{R}$ respectively, whose harmonic point are used in the MPFA-H interpolation. In addition, $\hat{M}$ and $\hat{N}$ are other volumes in the MPFA-H stencil that shares HI and JK with $\hat{L}$ and $\hat{R}$ respectively. All of those points can be seen in Fig. To reduce notation in the remaining of this section, the subsequent definitions are used: $w^{G}_{\hat{L},i(IJ)} = w^{G}_{\hat{L},IJ}$, $w^{G}_{\hat{L},j(IJ)} = w^{G}_{\hat{M},HI}$, $w^{G}_{\hat{R},i(IJ)} = w^{G}_{\hat{R},IJ}$, $w^{G}_{\hat{R},j(IJ)} = w^{G}_{\hat{N},JK}$.

Figure 3 – Points used in the MPFA-H approximation.

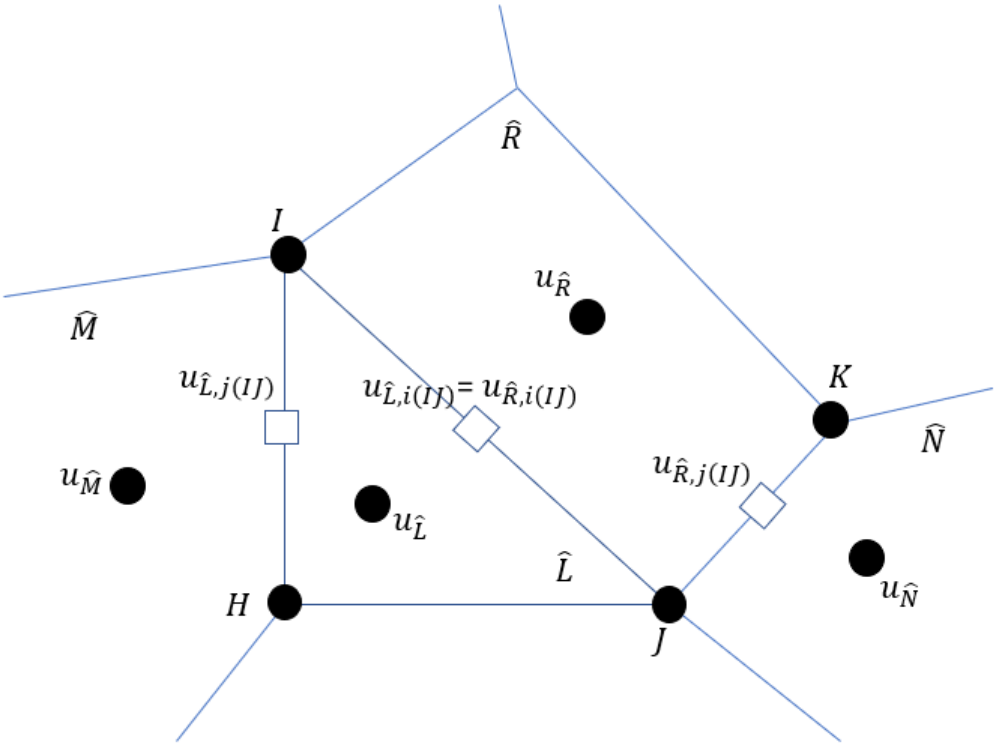

Source: Own authorship (2023)

By substituting Eq. 3.104 and Eq. 3.105 into Eq. 3.101, and doing some albegraic manipulations, one gets:

$$\nabla u \cdot \underline{G}\overrightarrow{n}_{IJ} \approx w^{G}_{\hat{L},i(IJ)} \mathcal{A}^{G}_{\hat{R},IJ} u_{\hat{R}} - w^{G}_{\hat{R},i(IJ)} \mathcal{A}^{G}_{\hat{L},IJ} u_{\hat{L}} + w^{G}_{\hat{R},i(IJ)} \mathcal{D}^{G,u}_{\hat{L},IJ} - w^{G}_{\hat{L},i(IJ)} \mathcal{D}^{G,u}_{\hat{R},IJ} \tag{3.114}$$

Furthermore, the pressure gradient in Eq. 3.98 is approximated by using Eq. 3.93 and Eq. 3.82. After the discretization of all terms in Eq. 3.98, one can write for the cell $\hat{L}$ the following expression:

$$\sum_{IJ\in\Gamma_{\hat{L}}} |IJ| \left[w^G_{\hat{L},i(IJ)} \mathcal{A}^G_{\hat{R},IJ} u_{\hat{R}} - w^G_{\hat{R},i(IJ)} \mathcal{A}^G_{\hat{L},IJ} u_{\hat{L}} + w^G_{\hat{R},i(IJ)} \mathcal{D}^{G,u}_{\hat{L},IJ} - w^G_{\hat{L},i(IJ)} \mathcal{D}^{G,u}_{\hat{R},IJ} \right] = \\ = \alpha_{\hat{L}} \sum_{IJ\in\Gamma_{\hat{L}}} |IJ| p_{IJ} n_{IJ,x} \quad (3.115)$$

where $n_{IJ,x}$ is the x component of $\overrightarrow{n}_{IJ}$.

Similarly, for the v component of the displacement vector, one can write:

$$\sum_{IJ\in\Gamma_{\hat{L}}} |IJ| \left[w^G_{\hat{L},i(IJ)} \mathcal{A}^G_{\hat{R},IJ} v_{\hat{R}} - w^G_{\hat{R},i(IJ)} \mathcal{A}^G_{\hat{L},IJ} v_{\hat{L}} + w^G_{\hat{R},i(IJ)} \mathcal{D}^{G,v}_{\hat{L},IJ} - w^G_{\hat{L},i(IJ)} \mathcal{D}^{G,v}_{\hat{R},IJ} \right] = \\ = \alpha_{\hat{L}} \sum_{IJ\in\Gamma_{\hat{L}}} |IJ| p_{IJ} n_{IJ,y} \quad (3.116)$$

where $n_{IJ,y}$ is the y component of $\overrightarrow{n}_{IJ}$. By isolating $u_{\hat{L}}$ from Eq. 3.115, one gets:

$$a_{u,\hat{L}} u_{\hat{L}} = \sum_{nb} \left(a_{u,nb} u_{nb} \right)_{\hat{L}} + \alpha_{\hat{L}} \sum_{IJ\in\Gamma_{\hat{L}}} |IJ| p_{IJ} n_{IJ,x} \quad (3.117)$$

where:

$$\sum_{nb} \left(a_{u,nb} u_{nb} \right)_{\hat{L}} = \\ = \sum_{IJ\in\Gamma_{\hat{L}}} w^G_{\hat{L},i(IJ)} \left(b_{u,\hat{L}} u_{\hat{R}} + \alpha^G_{\hat{L},j(IJ)} w_{\hat{L},j(IJ)} u_{\hat{M}} - \alpha^G_{\hat{R},j(IJ)} w_{\hat{R},j(IJ)} u_{\hat{N}} \right) \quad (3.118)$$

$$b_{u,\hat{L}} = \mathcal{A}^G_{\hat{R},IJ} + \alpha^G_{\hat{L},i(IJ)} w^G_{\hat{R},i(IJ)} - \sum_{\gamma=i,j} \alpha^G_{\hat{R},\gamma(IJ)} w^G_{\hat{R},\gamma(IJ)} \quad (3.119)$$

$$a_{u,\hat{L}} = \sum_{IJ\in\Gamma_{\hat{L}}} w^G_{\hat{R},i(IJ)} \left(\mathcal{A}^G_{\hat{L},IJ} - \sum_{\gamma=i,j} \alpha^G_{\hat{L},\gamma(IJ)} w^G_{\hat{L},\gamma(IJ)} + \alpha^G_{\hat{R},i(IJ)} w^G_{\hat{L},i(IJ)} \right) \quad (3.120)$$

By doing similar procedure for $u_{\hat{R}}$, one can write:

$$a_{u,\hat{R}} u_{\hat{R}} = \sum_{nb} \left(a_{u,nb} u_{nb} \right)_{\hat{R}} + \alpha_{\hat{R}} \sum_{IJ\in\Gamma_{\hat{R}}} |IJ| p_{IJ} n_{IJ,x} \quad (3.121)$$

where:

$$\sum_{nb}\left(a_{u,nb}u_{nb}\right)_{\hat{R}} = \\ = \sum_{IJ\in\Gamma_{\hat{R}}} w^G_{\hat{R},i(IJ)}\left(b_{u,\hat{R}}u_{\hat{L}} - \alpha^G_{\hat{L},j(IJ)}w_{\hat{L},j(IJ)}u_{\hat{M}} + \alpha^G_{\hat{R},j(IJ)}w_{\hat{R},j(IJ)}u_{\hat{N}}\right) \quad (3.122)$$

$$b_{u,\hat{R}} = \mathcal{A}^G_{\hat{L},IJ} + \alpha^G_{\hat{R},i(IJ)}w^G_{\hat{L},i(IJ)} - \sum_{\gamma=i,j}\alpha^G_{\hat{L},\gamma(IJ)}w^G_{\hat{L},\gamma(IJ)} \quad (3.123)$$

$$a_{u,\hat{R}} = \sum_{IJ\in\Gamma_{\hat{R}}} w^G_{\hat{L},i(IJ)}\left(\mathcal{A}^G_{\hat{R},IJ} - \sum_{\gamma=i,j}\alpha^G_{\hat{R},\gamma(IJ)}w^G_{\hat{R},\gamma(IJ)} + \alpha^G_{\hat{L},i(IJ)}w^G_{\hat{R},i(IJ)}\right) \quad (3.124)$$

Furthermore, we define the following auxiliary variables:

$$M_{\hat{L}} = \frac{\sum_{nb}\left(a_{u,nb}u_{nb}\right)_{\hat{L}}}{a_{u,\hat{L}}},\ M_{\hat{R}} = \frac{\sum_{nb}\left(a_{u,nb}u_{nb}\right)_{\hat{R}}}{a_{u,\hat{R}}} \quad (3.125)$$

Using the definitions of Eq. 3.125, one can write Eq. 3.117 and Eq. 3.121 as follows:

$$u_{\hat{L}} = M_{\hat{L}} + \frac{\alpha_{\hat{L}}}{a_{u,\hat{L}}}\sum_{IJ\in\Gamma_{\hat{L}}}|IJ|p_{IJ}n_{IJ,x} \quad (3.126)$$

$$u_{\hat{R}} = M_{\hat{R}} + \frac{\alpha_{\hat{R}}}{a_{u,\hat{R}}}\sum_{IJ\in\Gamma_{\hat{R}}}|IJ|p_{IJ}n_{IJ,x} \quad (3.127)$$

Similarly, one can write the approximation of the Linear Momentum Conservation Equation for the middle point of IJ:

$$u_{IJ} = M_{IJ} + \frac{\alpha_{IJ}V_{IJ}}{a_{u,IJ}}\frac{\partial p}{\partial x}\bigg|_{IJ} \quad (3.128)$$

where the coefficients M_{IJ} and $V_{IJ}/a_{u,IJ}$ are obtained via interpolation as follows (ZHANG; ZHAO; BAYYUK, 2014):

$$M_{IJ} = (1-\beta)\,M_{\hat{L}} + \beta M_{\hat{R}},\ \frac{\alpha_{IJ}V_{IJ}}{a_{u,IJ}} = (1-\beta)\,\frac{\alpha_{\hat{L}}V_{\hat{L}}}{a_{u,L}} + \beta\frac{\alpha_{\hat{R}}V_{\hat{R}}}{a_{u,R}} \quad (3.129)$$

In the present work, we have chosen $\beta = \frac{1}{2}$. By isolating $M_{\hat{L}}$ and $M_{\hat{L}}$ and then substituting them on Eq. 3.128 one gets:

$$u_{IJ} = (1-\beta)\left(u_{\hat{L}} - \frac{\alpha_{\hat{L}}}{a_{u,\hat{L}}}\sum_{IJ\in\Gamma_{\hat{L}}}|IJ|p_{IJ}n_{IJ,x}\right) + \\ + \beta\left(u_{\hat{R}} - \frac{\alpha_{\hat{R}}}{a_{u,\hat{R}}}\sum_{IJ\in\Gamma_{\hat{R}}}|IJ|p_{IJ}n_{IJ,x}\right) + \frac{\alpha_{IJ}V_{IJ}}{a_{u,IJ}}\left.\frac{\partial p}{\partial x}\right|_{IJ} \quad (3.130)$$

Furthermore, rearranging the terms in Eq. 3.130, it's possible to write:

$$u_{IJ} = \overline{u_{IJ}} - (1-\beta)\frac{\alpha_{\hat{L}}}{a_{u,\hat{L}}}\sum_{IJ\in\Gamma_{\hat{L}}}|IJ|p_{IJ}n_{IJ,x} - \\ - \beta\frac{\alpha_{\hat{R}}}{a_{u,\hat{R}}}\sum_{IJ\in\Gamma_{\hat{R}}}|IJ|p_{IJ}n_{IJ,x} + \frac{\alpha_{IJ}V_{IJ}}{a_{u,IJ}}\left.\frac{\partial p}{\partial x}\right|_{IJ} \quad (3.131)$$

where:

$$\overline{u_{IJ}} = (1-\beta)\,u_{\hat{L}} + \beta u_{\hat{R}} \quad (3.132)$$

Similarly, for v_{IJ}:

$$v_{IJ} = \overline{v_{IJ}} - (1-\beta)\frac{\alpha_{\hat{L}}}{a_{v,\hat{L}}}\sum_{IJ\in\Gamma_{\hat{L}}}|IJ|p_{IJ}n_{IJ,y} - \\ - \beta\frac{\alpha_{\hat{R}}}{a_{v,\hat{R}}}\sum_{IJ\in\Gamma_{\hat{R}}}|IJ|p_{IJ}n_{IJ,y} + \frac{\alpha_{IJ}V_{IJ}}{a_{u,IJ}}\left.\frac{\partial p}{\partial y}\right|_{IJ} \quad (3.133)$$

where:

$$\overline{v_{IJ}} = (1-\beta)\,v_{\hat{L}} + \beta v_{\hat{R}} \quad (3.134)$$

Moreover, the following approximation is used for the pressure gradient at IJ (ZHANG; ZHAO; BAYYUK, 2014):

$$\left.\nabla p\right|_{IJ} \approx \left.\frac{\partial p}{\partial \overrightarrow{n}}\right|_{IJ} = \left(\left.\nabla p\right|_{IJ}\cdot\overrightarrow{n}_{IJ}\right)\overrightarrow{n}_{IJ} = \frac{p_{\hat{R}} - p_{\hat{L}}}{|\overrightarrow{r}_{\hat{L},\hat{R}}\cdot\overrightarrow{n}_{IJ}|}\overrightarrow{n}_{IJ} \quad (3.135)$$

where $\overrightarrow{r}_{\hat{L},\hat{R}} = x_{\hat{R}} - x_{\hat{L}}$. Finally, by using Eq. 3.131 and Eq. 3.133 as the interpolation functions for u_{IJ} and v_{IJ} respectively, the edge displacements depend not only of $\overrightarrow{u}_{\hat{L}}$ and $\overrightarrow{u}_{\hat{R}}$, but also of $p_{\hat{L}}$ and $p_{\hat{R}}$ directly, which should increase the coupling strength between the solution fields p and $\overrightarrow{u}$, thus preventing the "Even-Odd decoupling" from happening.

3.4 Solution Procedure

The solution algorithm used in the present work is based on the fixed-strain operator split. First the solution is obtained by first solving the fluid-flow problem with constant volumetric deformation rate, then the mechanics problem is solved with a frozen pressure field. This choice of operator split was based on the ease of implementation and natural migration towards a better operator split, the Fixed-Stress Split. The Fixed-Strain split is conditionally stable, where the coupling strength between pressure and displacement, for a Backward Euler time integration, is given by (KIM; TCHELEPI; JUANES, 2011b):

$$\mathcal{C} = \frac{\alpha}{SK} \leq 1 \tag{3.136}$$

where $\mathcal{C}$ is the coupling strength. The split stability is dependant only of material properties.

Thus, the $3 * N_{cv} \times 3 * N_{cv}$ fully coupled problem is split into a $N_{cv} \times N_{vc}$ fluid flow problem and $2 * N_{cv} \times 2 * N_{cv}$ solid deformation problem (KIM; TCHELEPI; JUANES, 2011b):

$$\begin{bmatrix} \overrightarrow{u}^n \\ p^n \end{bmatrix} \underrightarrow{\mathcal{A}^p} \begin{bmatrix} \overrightarrow{u}^* \\ p^{n+1} \end{bmatrix} \underrightarrow{\mathcal{A}^u} \begin{bmatrix} \overrightarrow{u}^{n+1} \\ p^{n+1} \end{bmatrix} \tag{3.137}$$

where:

$$\mathcal{A}^p = \frac{\partial p}{\partial t} + \nabla \cdot \overrightarrow{v_t} + \alpha \frac{\partial \varepsilon_v}{\partial t} = Q_f,\ \delta\dot{\varepsilon_v} = 0 \tag{3.138}$$

$$\mathcal{A}^u = \nabla \cdot \underline{\sigma}' - \alpha \nabla p = \overrightarrow{f},\ p : prescribed. \tag{3.139}$$

The fluid flow problem is solved first while fixing the volumetric strain rate, then the resulting pressure field is prescribed to the solid deformation problem. $\delta\dot{\varepsilon_v} = 0$ means that $\alpha\dot{\varepsilon_v}$ is evaluated explicitly using the approximation define in section 3.3.2 and the Modified Rhie-Chow interpolation. A flowchart with the complete solution algorithm can be seen in Fig. 4. To initialize the solution, the first iteration start from the initial pressure $p0$, which is obtained via the analytical solution, then the next value of p is computed with $\dot{\varepsilon_v} = 0$, then a displacement field is computed via a one way coupling using the approximation for Eq. (2.5). Then, for remaining time steps, the simulation follows Fig. 4. Both system of equations are solved using a direct LU method.

Figure 4 – Flowchart for the fixed-strain solution algorithm

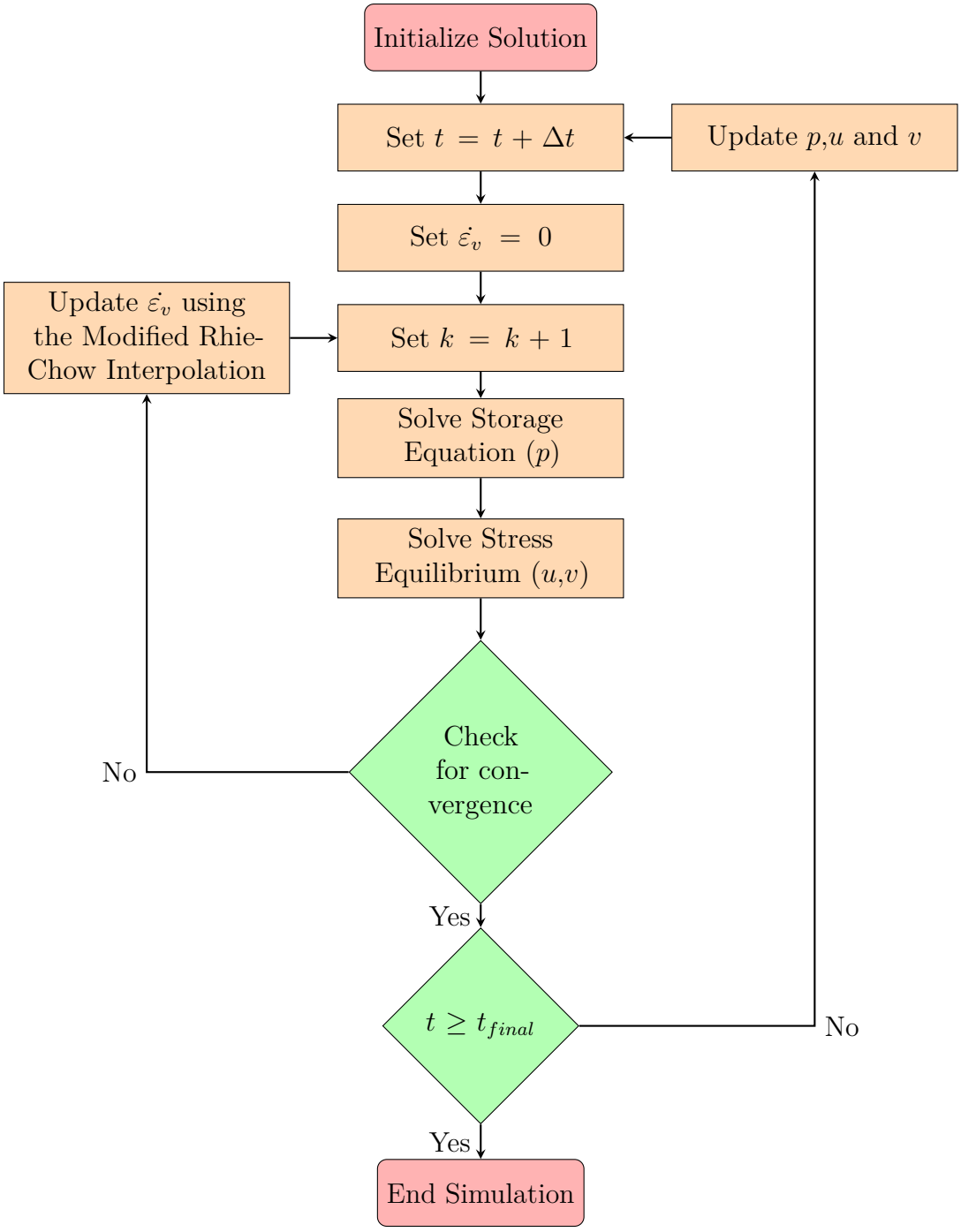

Source: Own authorship (2023)

Moreover, the convergence criteria is defined as follows:

$$\tau \geq \frac{\left|\left|p_{\Omega}^{k+1} - p_{\Omega}^{k}\right|\right|_{\infty}}{\left|\left|p_{\Omega}^{k+1}\right|\right|_{\infty}} \tag{3.140}$$

where p_{Ω} is a vector whose components are the pressure value of each cell $\hat{L}$. In addition,

the symbol $||\cdot||_\infty$ represents the L_∞ norm, whose value is the supremum of the set inside the brackets. τ is a set tolerance.

The simulations in the present work were done using a Intel i5-8400 CPU 2.80 GHz, 12GB of RAM, and the following software:

- Mesh generation was done using the software Gmsh (GEUZAINE; REMACLE, 2017);
- Mesh pre-processing was done using the software (IMPRESS, 2020);
- Simulation was done using a in-house python software;
- Post processing was done using VisIt (LLNL, 2005);

4 RESULTS

In the following chapter, the numerical formulation shown in the present work is used to solve elementary poroelastic problems, all of them with analytic solutions, in order to assess the formulation's consistency and accuracy. Those problems are Terzahi's Problem, with both a homogeneous (WANG, 2000) and a heterogeneous (VERRUIJT, 2013) porous media and Mandel's Problem (ABOUSLEIMAN et al., 1996). All the examples solved uses the convergence tolerance $\tau = 10^{-8}$. For the benchmarks solved in the present work, the Rhie-Chow interpolation was not used and satisfactory results were obtained. However, more sophisticated problems are going to require a LBB stabilization, which will be tested in future works.

4.1 Error Evaluation

In order to compare analytical and numeric solutions, where one is available, first we define a normalized L_2 error norm as follows (HERBIN; HUBERT, 2008):

$$\epsilon_\psi = \left(\frac{\sum_{\hat{L}\in\Omega} \left(\psi(x_{\hat{L}}) - \psi_{\hat{L}}\right)^2 V_{\hat{L}}}{\sum_{\hat{L}\in\Omega} \psi(x_{\hat{L}})^2 V_{\hat{L}}} \right)^{\frac{1}{2}}, \ \psi = p, \ u, \ v \tag{4.1}$$

where $\psi_{\hat{L}}$ is the numerical solution associated with the computational cell $\hat{L}$, and $\psi(x_{\hat{L}})$ is the analytical solution evaluated at $\hat{L}$ centroid $x_{\hat{L}}$. Moreover, the characteristic length associated with each mesh is given by:

$$h = \frac{\sum_{\hat{L}\in\Omega} \sqrt{V_{\hat{L}}}}{N_{cv}} \tag{4.2}$$

4.2 Terzaghi's Problem

4.2.1 Problem Description

Terzaghi's Problems consists in a homogeneous poroelastic column with height H and length L, where, at its top, a load σ_0 is applied and drainage occurs (Fig. 5). Its sides are impermeable and are prevented from lateral movement. Its bottom portion is fixed and also impermeable. Thus, the columns has a displacement only in the vertical direction. In Fig. 6, it's possible to see the dimensions of the poroelastic column and the boundary conditions, which are explicited in Table 1. Moreover, Table 2 shows solid and

fluid properties used in the simulation, both sourced from (WANG, 2000). Furthermore, $p_0 = 435.2\ kPa$.

Figure 5 – Terzaghi's Problem - Description diagram.

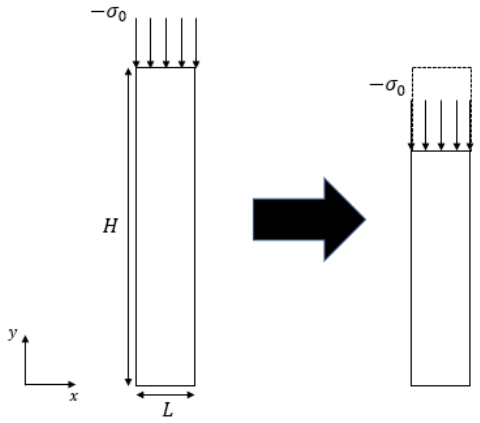

Source: Own authorship (2023)

Figure 6 – Terzaghi's Problem - *a*) Domain dimensions and *b*) Domain boundaries.

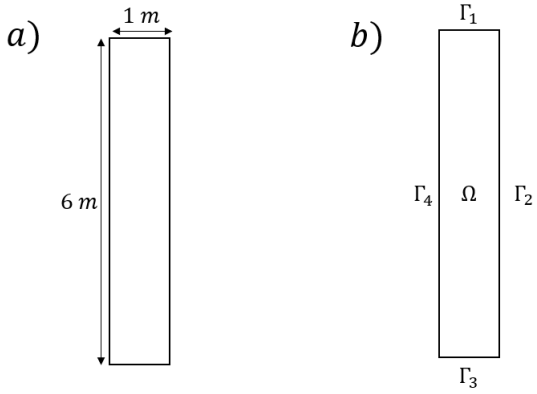

Source: Own authorship (2023)

Table 1 – Terzaghi's Problem - Boundary conditions.

Boundary	Fluid	Solid	
Γ_1	$p = 0\ Pa$	$\mathcal{T}_x = 0\ Pa$	$\mathcal{T}_y = -1 \times 10^6\ Pa$
Γ_2	$\overrightarrow{v_t} \cdot \overrightarrow{n}_{IJ} = 0\ ms^{-1}$	$u = 0\ m$	$\mathcal{T}_y = 0\ Pa$
Γ_3	$\overrightarrow{v_t} \cdot \overrightarrow{n}_{IJ} = 0\ ms^{-1}$	$\mathcal{T}_x = 0\ Pa$	$v = 0\ m$
Γ_4	$\overrightarrow{v_t} \cdot \overrightarrow{n}_{IJ} = 0\ ms^{-1}$	$u = 0\ m$	$\mathcal{T}_y = 0\ Pa$

Source: Own authorship (2023)

Table 2 – Terzaghi's Problem - Solid and fluid properties.

Property	Value
Solid Compressibility (c_s)	$2.777778 \times 10^{-11}\ Pa^{-1}$
Young's Modulus (E)	$14.4 \times 10^{9}\ Pa$
Poisson's Coefficient (ν)	0.2
Porosity (ϕ)	0.19
Permeability (k)	$1.9 \times 10^{-15}\ m^2$
Biot's Coefficient (α)	0.777778
Fluid Compressibility (c_f)	$3.030303 \times 10^{-10}\ Pa^{-1}$
Viscosity (μ)	$1 \times 10^{-3}\ Pa.s$

Source: Own authorship (2023)

4.2.2 Results

For this preliminary analysis, three different meshes will be used (Fig. 7): one structured with quadrilateral elements, called mesh A; one unstructured with triangular elements, called mesh B, and one unstructured with quadrilateral elements, called mesh C. Both the structured quadrilateral and the unstructured triangular have a resolution of 3x15, with a total of 45 elements for the structured mesh, 90 for the triangular mesh, and the unstructured quadrilateral mesh has a total of 58 elements.

Figure 7 – Terzaghi's Problem - meshes *a*) structured with quadrilateral elements; *b*) unstructured with triangular elements; *c*) unstructured with quadrilateral elements.

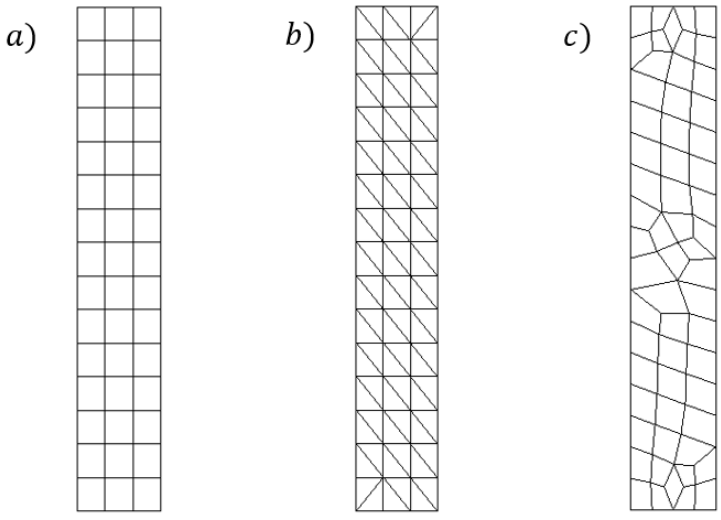

Source: Own authorship (2023)

Fig. 8, Fig. 9 and Fig. 10 show a comparison between the numerical and analytic pressure solutions, whose description in detail can be found in Appendix A, along the line $x = 0.5\ m$ and $\Delta t = 1\ s$.

Figure 8 – Terzaghi's Problem - pore pressure distribution for mesh A and $\Delta t = 1\ s$.

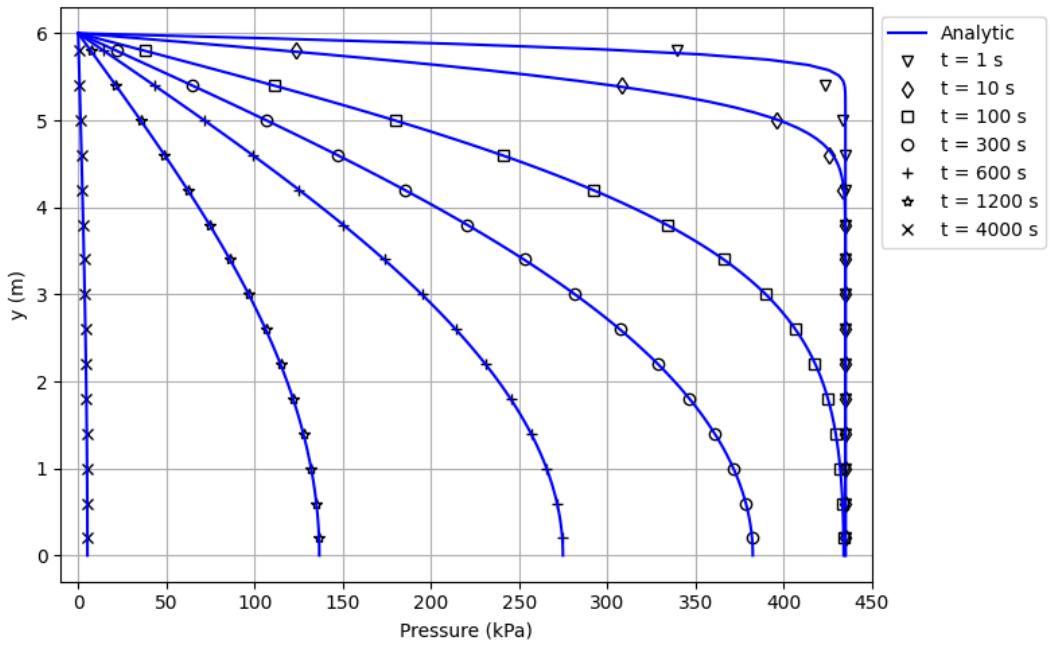

Source: Own authorship (2023)

Figure 9 – Terzaghi's Problem - pore pressure distribution for mesh B and $\Delta t = 1\ s$.

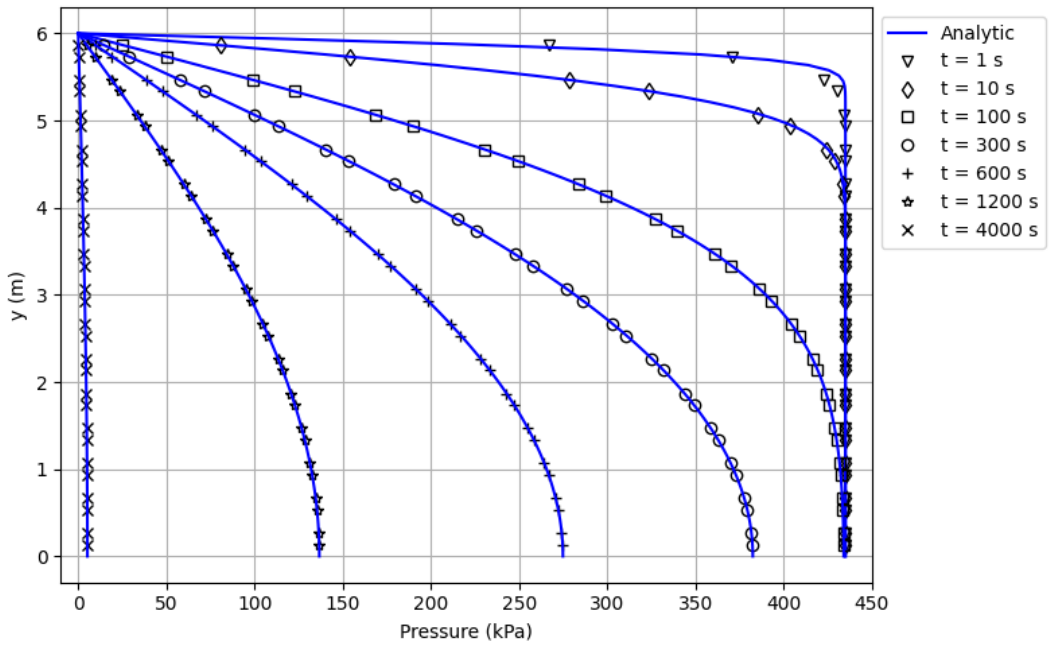

Source: Own authorship (2023)

Figure 10 – Terzaghi's Problem - pore pressure distribution for mesh C and $\Delta t = 1\ s$.

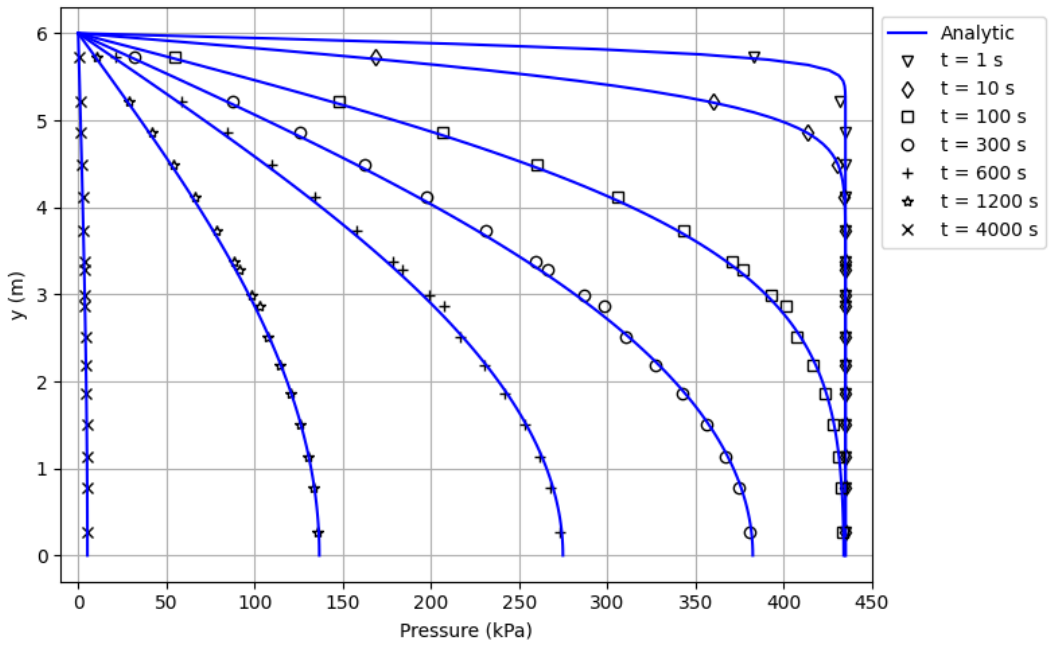

Source: Own authorship (2023)

From Fig. 8, Fig. 9 and Fig. 10, one can conclude that the numerical formulation presented in this work is capable of accurately match the problem's analytical solution. The error observed at $t = 1\ s$ in the three plots is expected due to the high pressure gradient that happens at low values of t. This error can be reduced via the usage of a higher-order approximation or mesh refinement. The latter option is going to be explored in section 4.2.3. In addition, the pressure oscillation observed in Fig. 10, between 2 m and 4 m is due to the fact that, in its middle portion, mesh C is more coarse and slightly distorted, which increases error. However, this loss of accuracy is still in the acceptable range.

Furthermore, the pressure and displacements profiles are shown in Fig. 11 and Fig. 12 respectively. Fig. 13 shows the displacement field behavior in different time values. They exhibit the expected behavior of a sample under the conditions describe. The load at the top promotes a compression of the porous media which drives fluid drainage through the permeable lid. The lowest values of pressure are closer to the top, where $p = 0$, while the highest values are close to the bottom, with a decrease in overall fluid pressure over time. On the other hand, the highest values of displacement are closer to the top, where the load is applied, while the lowest values of displacement are at the bottom, where the sample is fixed.

Figure 11 – Terzaghi's Problem - pore pressure profiles for mesh A and $\Delta t = 1\ s$.

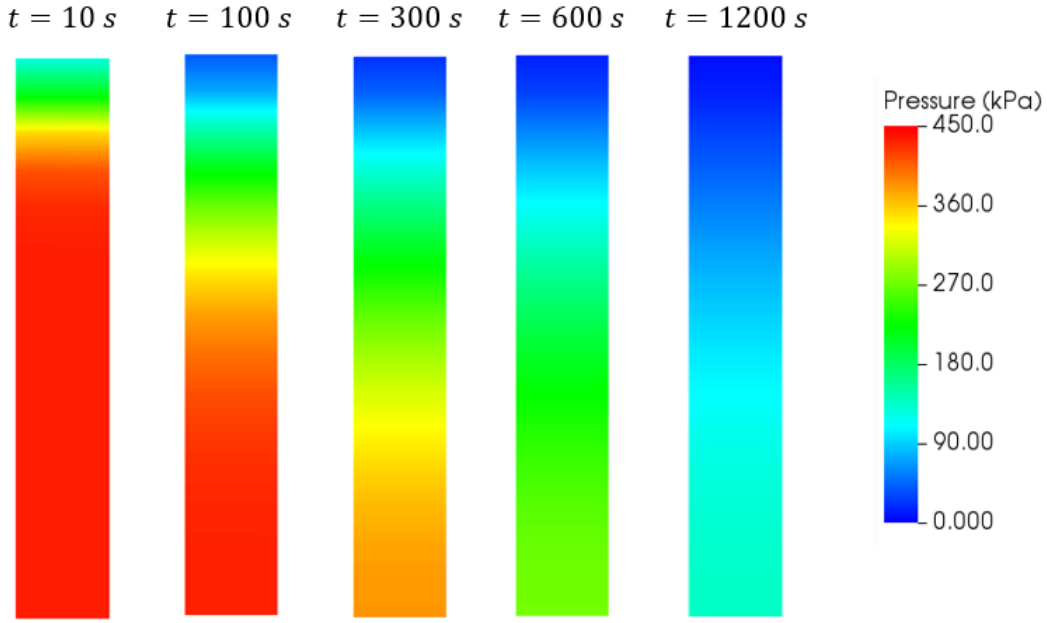

Source: Own authorship (2023)

Figure 12 – Terzaghi's Problem - Vertical displacement profiles for different times with for mesh A and $\Delta t = 1\ s$.

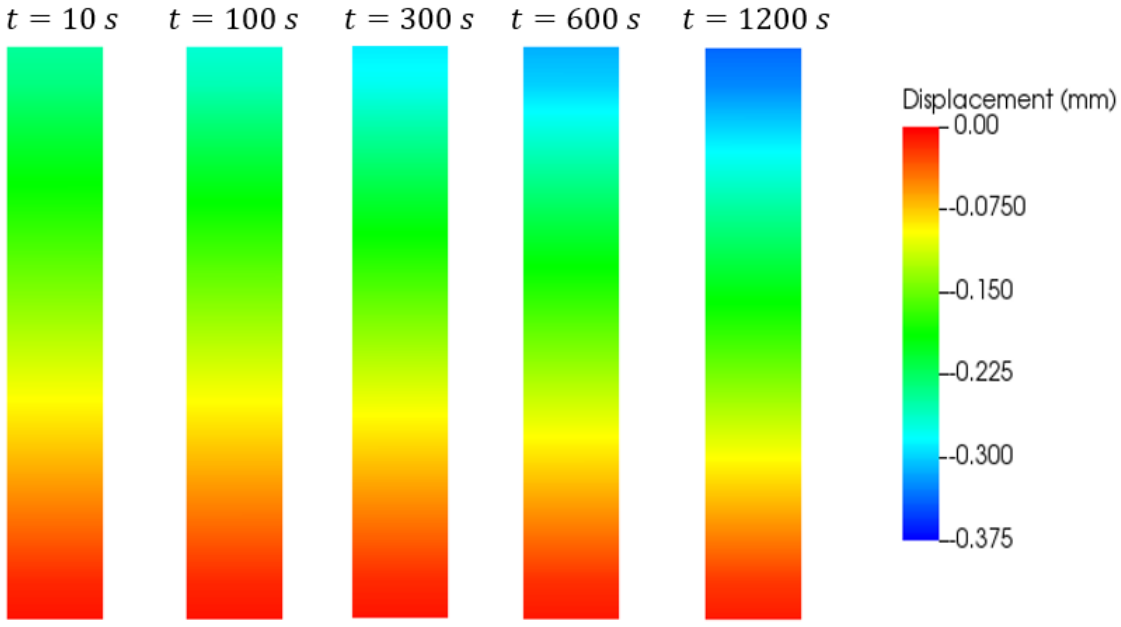

Source: Own authorship (2023)

Figure 13 – Terzaghi's Problem - Displacement field for different times with for mesh A and $\Delta t = 1\ s$.

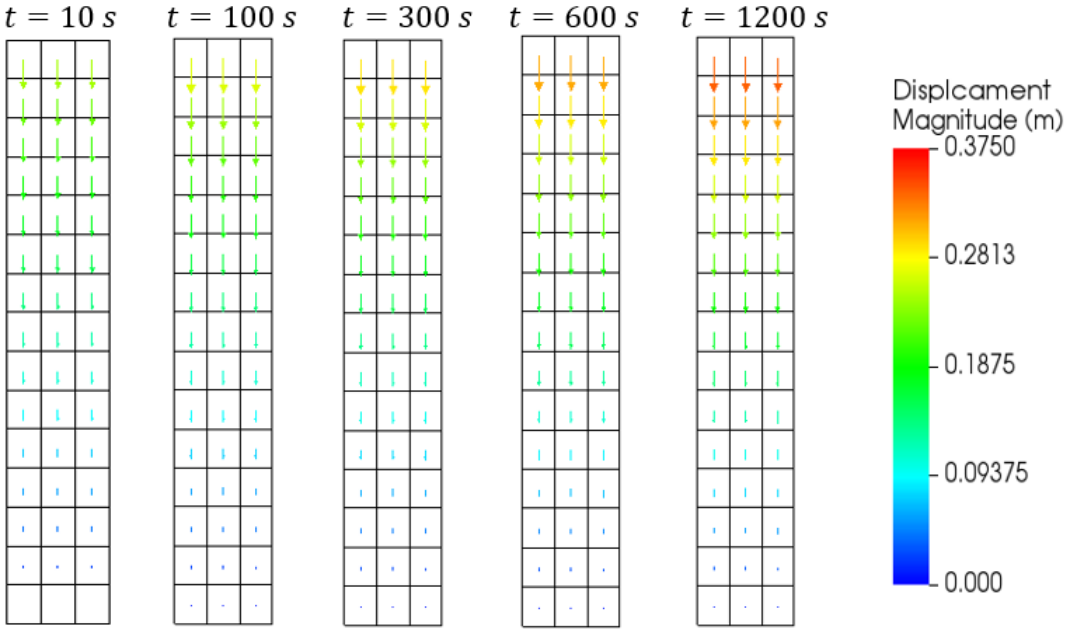

Source: Own authorship (2023)

4.2.3 Convergence Analysis

For the convergence analysis, mesh A was systematically refined as follows:

Table 3 – Terzaghi's Problem - mesh resolution for convergence analysis.

Mesh Name	Resolution	Characteristic Length (m)
Mesh A1	3×15	0.365
Mesh A2	6×30	0.183
Mesh A3	12×60	0.091
Mesh A4	18×90	0.061
Mesh A5	24×120	0.046

Source: Own authorship (2023)

Moreover, for each mesh, the pressure error was computed using Eq. (4.1) in the times $t = 1\ s$ and $t = 10\ s$, using the time steps $\Delta t = 1\ s$, $\Delta t = 0.5\ s$, $\Delta t = 0.25\ s$, $\Delta t = 0.1\ s$, $\Delta t = 0.05\ s$ and $\Delta t = 0.025\ s$. The results are shown in Table 4 and Table 5. Table 6 shows the Fourier's number associated with choice of time step and mesh resolution.

Table 4 – Terzaghi's Problem - pressure error computation for $t = 1\ s$.

Δt	$1\ s$	$0.5\ s$	$0.25\ s$	$0.1\ s$	$0.05\ s$	$0.025\ s$
A1	1.68×10^{-2}	1.43×10^{-2}	1.32×10^{-2}	1.27×10^{-2}	1.25×10^{-2}	1.25×10^{-2}
A2	2.42×10^{-2}	1.62×10^{-2}	1.16×10^{-2}	8.76×10^{-3}	7.90×10^{-3}	7.5×10^{-3}
A3	1.62×10^{-2}	8.64×10^{-3}	4.48×10^{-3}	2.06×10^{-3}	1.44×10^{-3}	1.26×10^{-3}
A4	1.47×10^{-2}	7.76×10^{-3}	3.97×10^{-3}	1.60×10^{-3}	8.55×10^{-4}	5.74×10^{-4}
A5	1.41×10^{-2}	7.56×10^{-3}	3.88×10^{-3}	1.55×10^{-3}	7.67×10^{-4}	4.14×10^{-4}

Source: Own authorship (2023)

Table 5 – Terzaghi's Problem - pressure error computation for $t = 10\ s$.

Δt	$1\ s$	$0.5\ s$	$0.25\ s$	$0.1\ s$	$0.05\ s$	$0.025\ s$
A1	5.52×10^{-3}	4.41×10^{-3}	4.06×10^{-3}	3.93×10^{-3}	3.92×10^{-3}	3.91×10^{-3}
A2	2.94×10^{-3}	1.54×10^{-3}	9.90×10^{-4}	8.46×10^{-4}	8.51×10^{-4}	8.64×10^{-4}
A3	2.87×10^{-3}	1.41×10^{-3}	6.89×10^{-4}	2.96×10^{-4}	2.16×10^{-4}	2.07×10^{-4}
A4	2.89×10^{-3}	1.43×10^{-3}	7.02×10^{-4}	2.71×10^{-4}	1.43×10^{-4}	1.01×10^{-4}
A5	2.89×10^{-3}	1.44×10^{-3}	7.12×10^{-4}	2.71×10^{-4}	1.35×10^{-4}	7.50×10^{-5}

Source: Own authorship (2023)

Table 6 – Terzaghi's Problem - Fourier's number associated with each choice of time step and mesh resolution.

Fo	$1\ s$	$0.5\ s$	$0.25\ s$	$0.1\ s$	$0.05\ s$	$0.025\ s$
A1	1.28×10^{-1}	6.38×10^{-2}	3.19×10^{-2}	1.28×10^{-2}	6.38×10^{-3}	3.19×10^{-3}
A2	5.08×10^{-1}	2.54×10^{-1}	1.27×10^{-1}	5.08×10^{-2}	2.54×10^{-2}	1.27×10^{-2}
A3	2.05×10^{0}	1.02×10^{0}	5.13×10^{-1}	2.05×10^{-1}	1.02×10^{-1}	5.13×10^{-2}
A4	4.57×10^{0}	2.28×10^{0}	1.14×10^{0}	4.57×10^{-1}	2.28×10^{-1}	1.14×10^{-1}
A5	8.03×10^{0}	4.02×10^{0}	2.00×10^{0}	8.03×10^{-1}	4.02×10^{-1}	2.00×10^{-1}

Source: Own authorship (2023)

Furthermore, two plots were constructed using the data from Table 4 and 5, to aid in the data analysis. Fig. 14 and Fig. 15 show the mesh convergence behaviour for pressure, for different time steps, at times t = 1 s and t = 10 s, respectively. Fig. 16 and Fig. 17 the mesh convergence behaviour for pressure, for different time steps, at times t = 1 s and t = 10 s, respectively.

Figure 14 – Terzaghi's Problem - pressure spatial convergence for $t = 1\ s$.

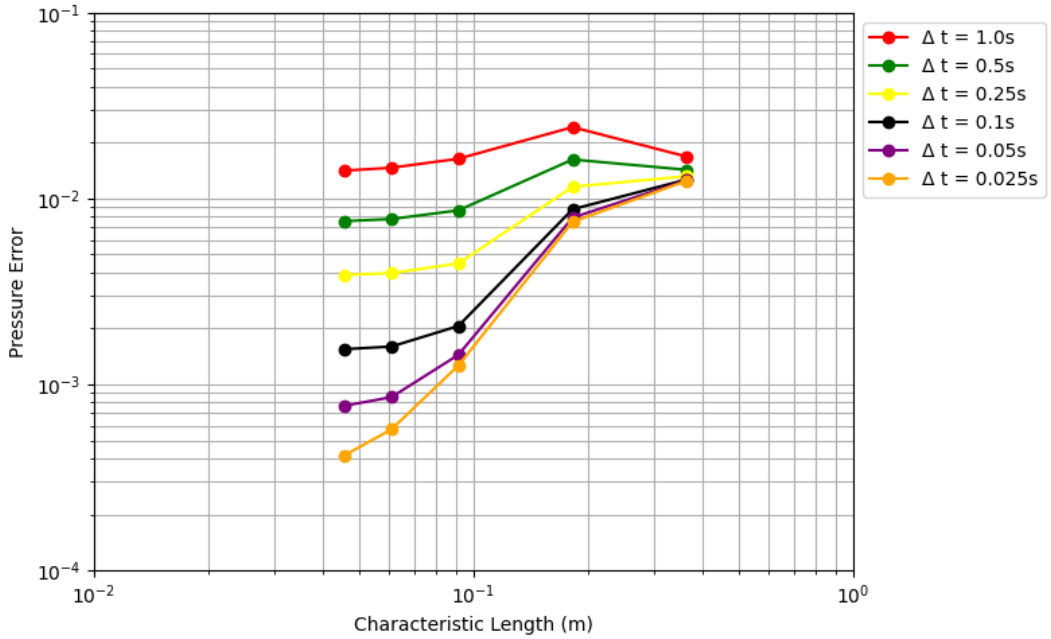

Source: Own authorship (2023)

Figure 15 – Terzaghi's Problem - pressure spatial convergence for $t = 10\ s$.

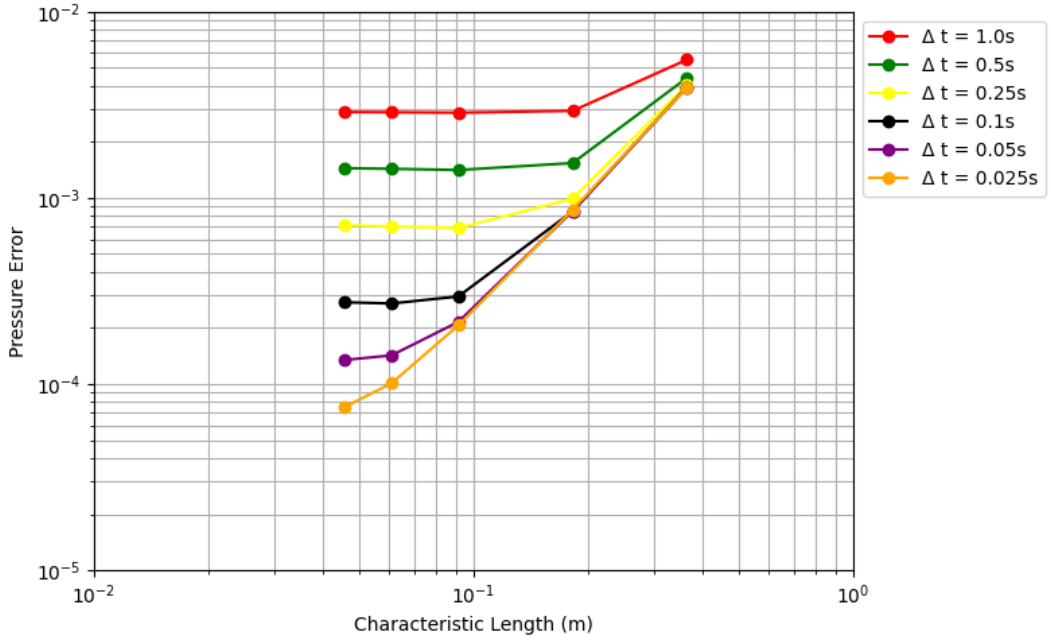

Source: Own authorship (2023)

Figure 16 – Terzaghi's Problem - pressure time convergence for $t = 1\ s$.

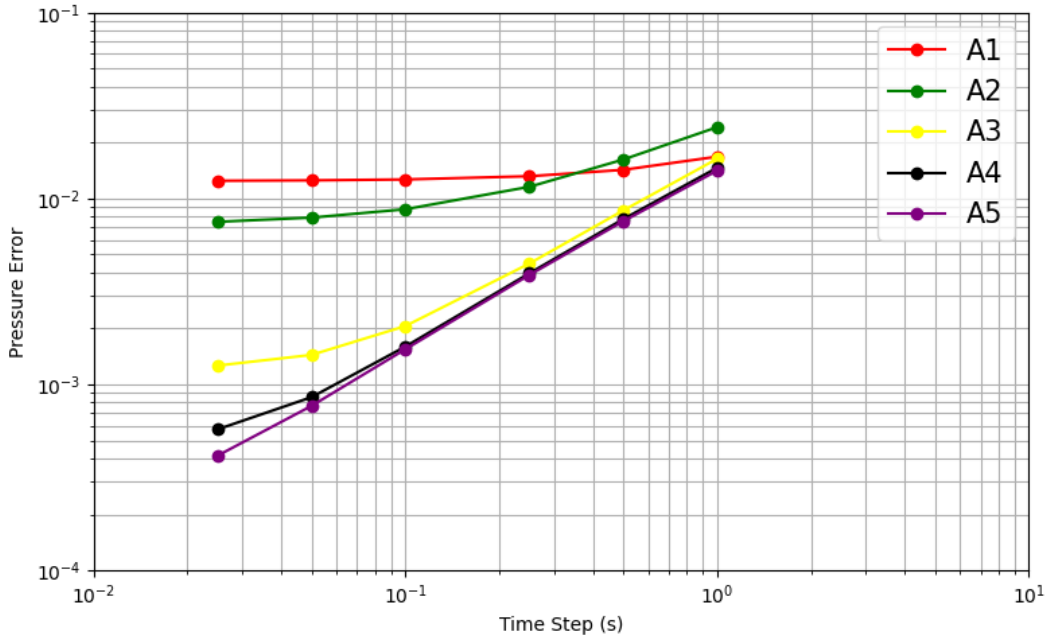

Source: Own authorship (2023)

Figure 17 – Terzaghi's Problem - pressure time convergence for $t = 10\ s$.

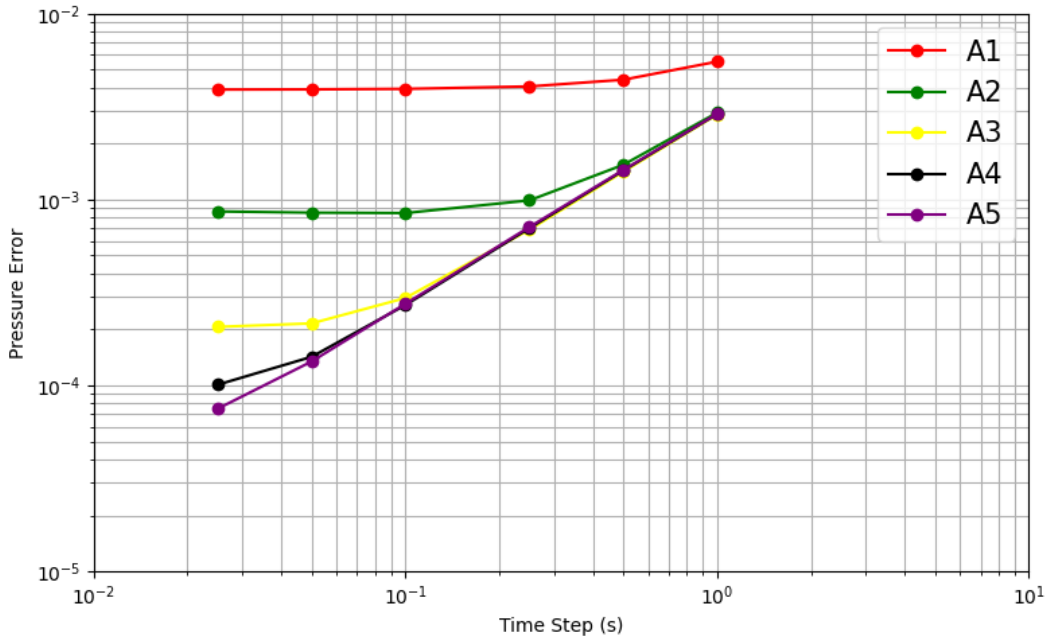

Source: Own authorship (2023)

From the analysis of data, as expected, one can conclude that mesh refinements and time step reductions, lead to overall decrease in error. Also, it is evident that the spatial and time discretization are not independent and without proper choice the expected convergence behavior is jeopardized. In addition, a increase in mesh resolution leads to

a greater error reduction than a time step reduction. This is due to the fact that the Backward Euler scheme uses a first order approximation for time while the MPFA-H is a second order approximation. As stated in section 4.2.2 a mesh refinement and a time step reduction increase the accuracy of the numerical method, which reduces the error associated with high pressure gradients.

For $t = 10\ s$, it is possible to see the effects of excessive mesh refinement and excessive time step reduction. This can lead to a increase in numerical diffusion, which can compromise the numerical solution. The error increase due to excessive mesh refinement can be seen for $\Delta t = 1\ s$, $\Delta t = 0.5\ s$, $\Delta t = 0.25\ s$, $\Delta t = 0.1\ s$, where the values of the Fourier number are relatively high compared to the stability limit for a Forwards Euler scheme, which is $Fo = 0.25$. The numerical scheme still converges to the numerical solution, since a Backwards Euler is unconditionally stable. In Fig. 15, it's possible to see that the accuracy increase due to mesh refinement reaches a plateau, to the point that, in Fig. 17, the plots for meshes A3, A4 and A5 almost coincide. However, Table 5 shows that error is actually starting to increase with further mesh refinement. A plateau can also be seen for time step reductions in meshes A1 and A2. However, like mesh refinement, Table 5 shows that error is actually starting to increase with further time step reduction. For times $\Delta t = 0.05\ s$ and $\Delta t = 0.025\ s$, the accuracy gained from time step reduction is able to postpone the effect. Furthermore, the effect of excessive time step reduction can be seen for mesh A2. Mesh A3, Mesh A4 and Mesh A5 have enough resolution so that the numerical diffusion associated wasn't enough to compromise the solution. However, due to being a coarse mesh, the error associated with Mesh A1 is high enough to where the numerical diffusion was not capable of producing a noticeable effect. In addition, when excessive mesh refinement starts to increase error, a time step reduction is necessary and vice-versa, i.e., a reduction in the Fourier's number. Thus confirming the relationship between time step and mesh resolution established by it.

4.3 Two-Layered Terzaghi's Problem

4.3.1 Problem Description

This problem is similar to the problem described in section 4.2. However the porous media is now heterogeneous, composed by 2 layers with different properties. Fig. 18 shows the dimensions of the poroelastic column and the boundary conditions, which are explicited in Table 7. Table 8 and Table 9 show solid and fluid properties used in the simulation. Both domains share the same mechanical properties with different values of permeability. Two cases were studied: one where $k1 > k2$ and the second one where $k1 < k2$. Furthermore, $p_0 = 435.2\ kPa$.

Figure 18 – Two-Layered Terzaghi's Problem - *a*) Domain dimensions and *b*) Domain boundaries.

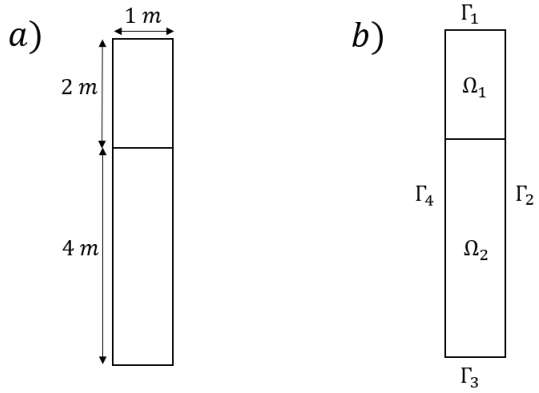

Source: Own authorship (2023)

Table 7 – Two-Layered Terzaghi's Problem - Boundary conditions.

Boundary	Fluid	Solid	
Γ_1	$p = 0\ Pa$	$\mathcal{T}_x = 0\ Pa$	$\mathcal{T}_y = -1 \times 10^6\ Pa$
Γ_2	$\overrightarrow{v_t} \cdot \overrightarrow{n}_{IJ} = 0\ ms^{-1}$	$u = 0\ m$	$\mathcal{T}_y = 0\ Pa$
Γ_3	$\overrightarrow{v_t} \cdot \overrightarrow{n}_{IJ} = 0\ ms^{-1}$	$\mathcal{T}_x = 0\ Pa$	$v = 0\ m$
Γ_4	$\overrightarrow{v_t} \cdot \overrightarrow{n}_{IJ} = 0\ ms^{-1}$	$u = 0\ m$	$\mathcal{T}_y = 0\ Pa$

Source: Own authorship (2023)

Table 8 – Two-Layered Terzaghi's Problem - Solid and fluid properties.

Property	Value
Solid Compressibility (c_s)	$2.777778 \times 10^{-11}\ Pa^{-1}$
Young's Modulus (E)	$14.4 \times 10^9\ Pa$
Poisson's Coefficient (ν)	0.2
Porosity (ϕ)	0.19
Biot's Coefficient (α)	0.777778
Fluid Compressibility (c_f)	$3.030303 \times 10^{-10}\ Pa^{-1}$
Viscosity (μ)	$1 \times 10^{-3}\ Pa.s$

Source: Own authorship (2023)

Table 9 – Two-Layered Terzaghi's Problem - Permeability values for the different domains.

	Permeability	Value
Case 1	Domain 1 (k_1)	$19 \times 10^{-15}\ m^2$
	Domain 2 (k_2)	$1.9 \times 10^{-15}\ m^2$
Case 2	Domain 1 (k_1)	$1.9 \times 10^{-15}\ m^2$
	Domain 2 (k_2)	$19 \times 10^{-15}\ m^2$

Source: Own authorship (2023)

4.3.2 Results

Fig. 19 and Fig. 20 show a comparison between the numerical and analytic pressure solutions, whose description in detail can be found in Appendix A, along the line $x = 0.5\ m$, for the mesh A1 with $\Delta t = 0.1\ s$. From Fig. 19 and Fig. 20, one can conclude that the numerical formulation presented in this work is capable of accurately match the problem's analytical solution, even with a discontinuity in the pressure field.

Figure 19 – Two-Layered Terzaghi's Problem - pore pressure distribution for mesh A1 and $\Delta t = 0.1\ s$: Case 1.

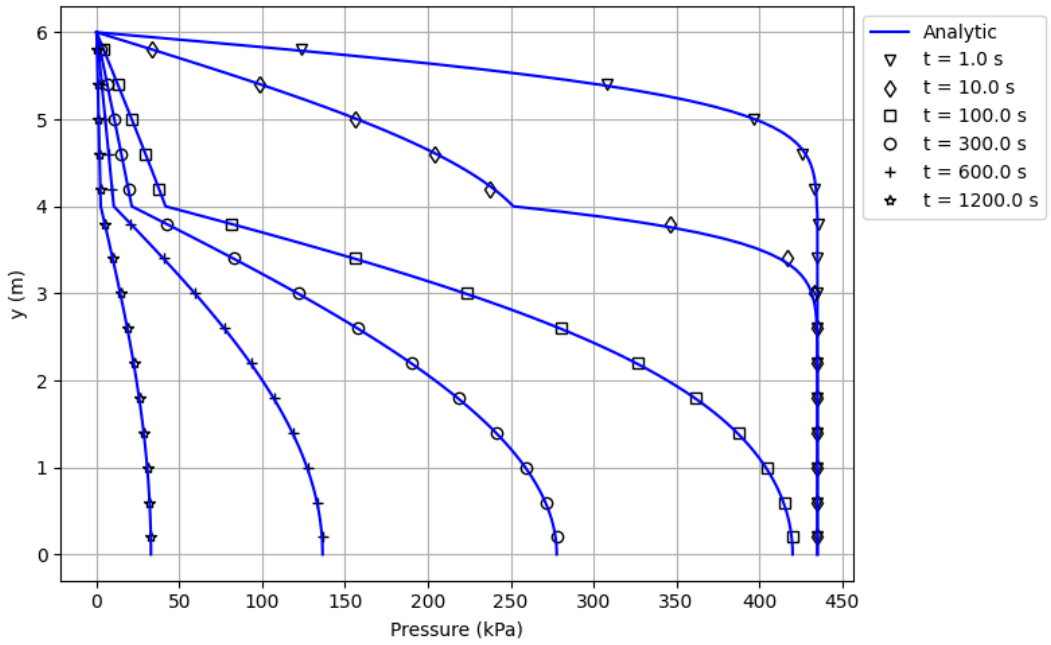

Source: Own authorship (2023)

Figure 20 – Two-Layered Terzaghi's Problem - pore pressure distribution for mesh A1 and $\Delta t = 0.1\ s$: Case 2.

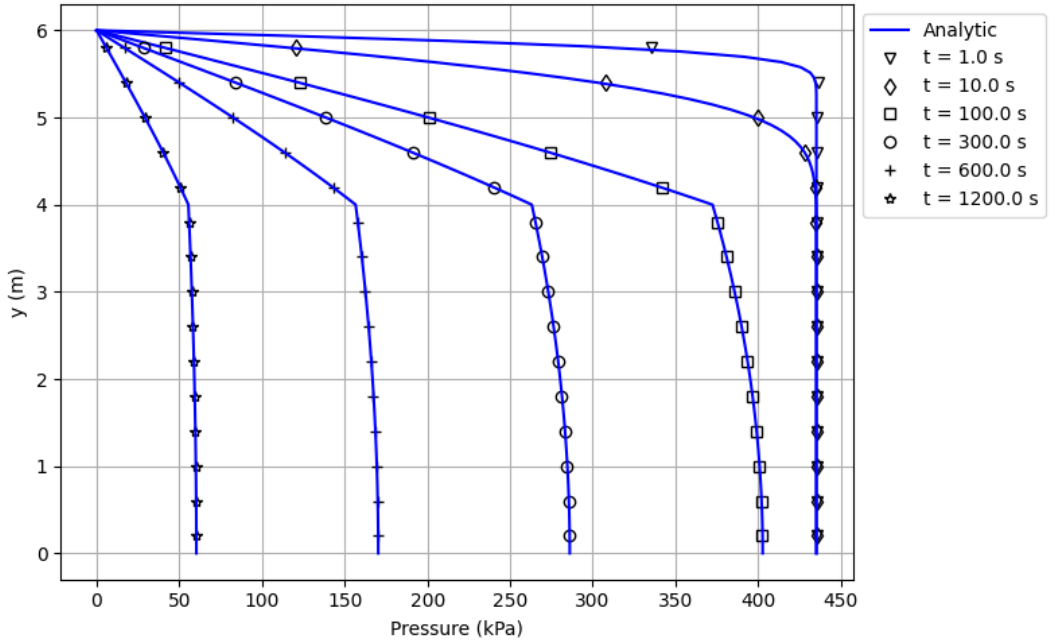

Source: Own authorship (2023)

Fig. 21 and Fig. 22 show pressure profiles for Case 1 and Case 2 respectively. Both figures shows the expected physical behavior, where the porous media with highest value of permeability have the smallest pressure gradient, until the pressure valuer are almost constant for high values of t.

Figure 21 – Two-Layered Terzaghi's Problem - Pore pressure profiles for different times with mesh A1 and $\Delta t = 0.1\ s$: Case 1.

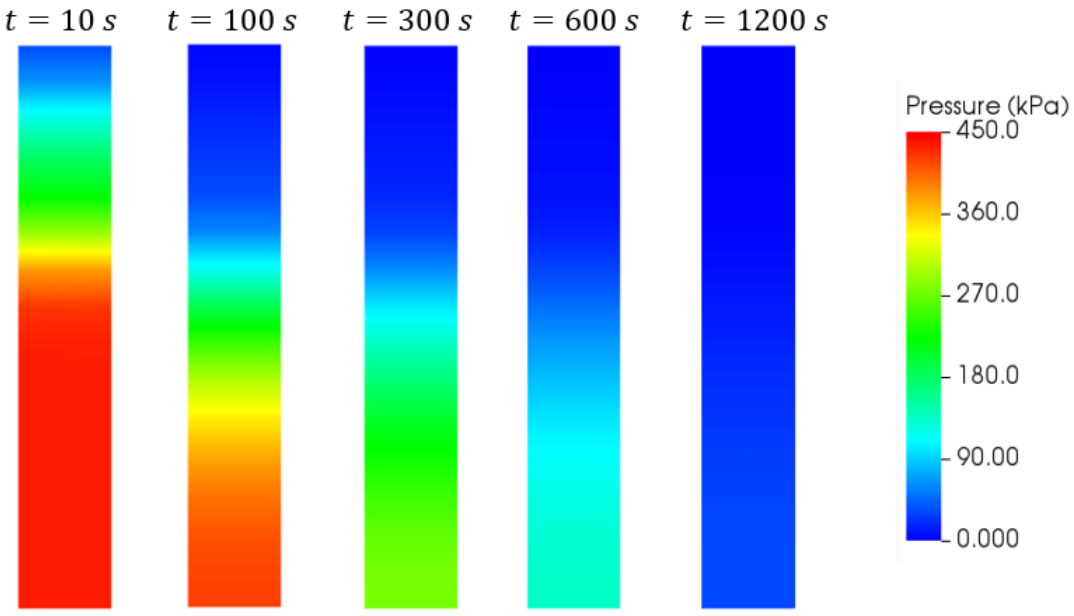

Source: Own authorship (2023)

Figure 22 – Two-Layered Terzaghi's Problem - Pore pressure profiles for different times with mesh A1 and $\Delta t = 0.1\ s$: Case 2.

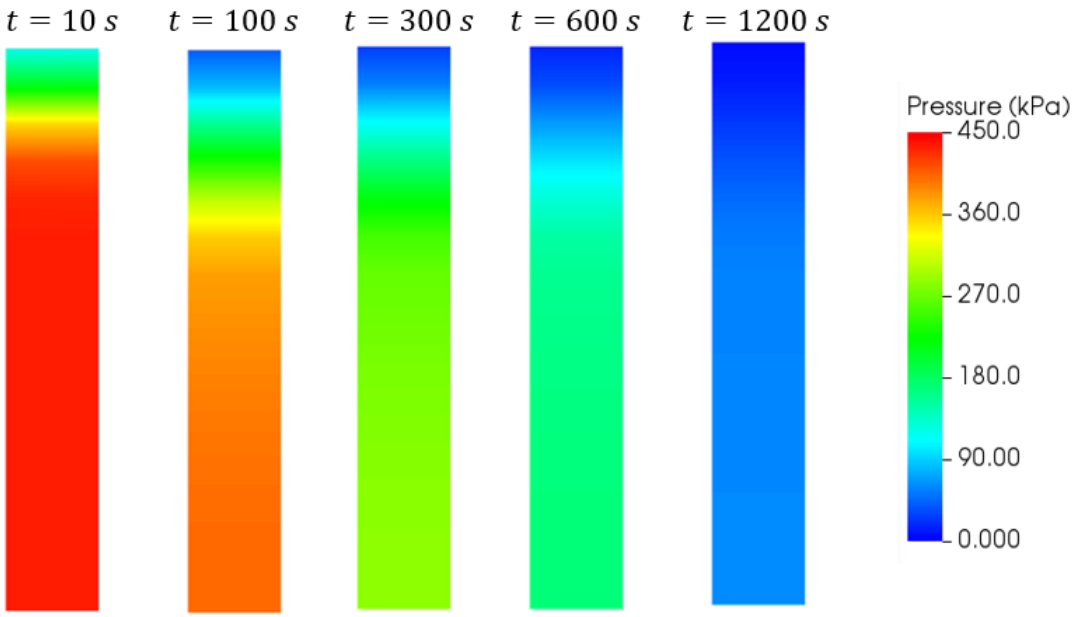

Source: Own authorship (2023)

Another interesting result is given by Fig. 23. It compares displacement solutions for mesh A1 at $t = 600\ s$, with $\Delta t = 0.1\ s$, and the analytical solution for the homogeneous case at $t = 600\ s$. No displacement solution is available for the two-layered version of Terzaghi's Problem. Since the displacement solutions for the homogeneous and heterogeneous cases are decoupled from the pressure solution, and also in both heterogeneous cases the two media share mechanical properties, all three displacement solutions are similar, albeit some negligible difference.

Figure 23 – Two-Layered Terzaghi's Problem - displacement solutions comparison at $t = 600s$ for mesh A1 and $\Delta t = 0.1\ s$.

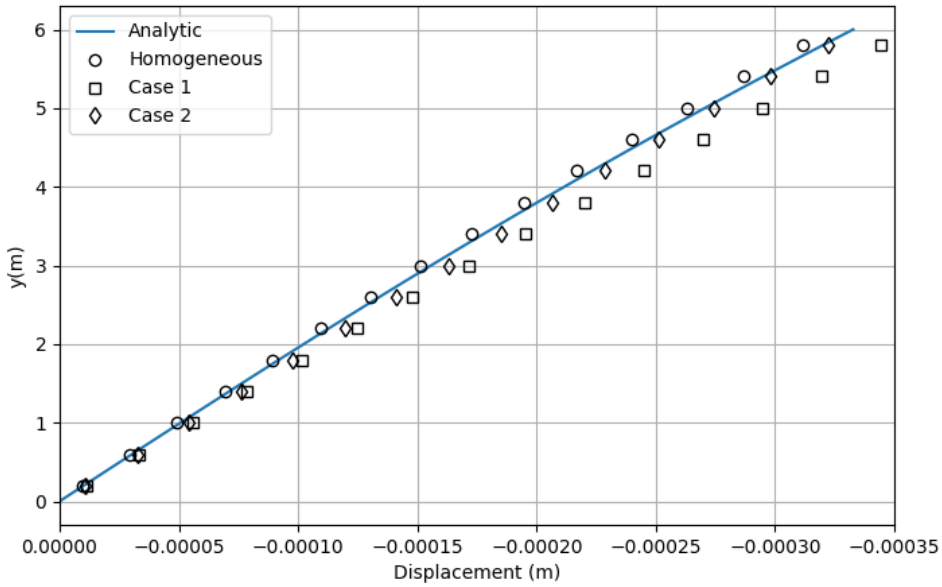

Source: Own authorship (2023)

4.4 Mandel's Problem

4.4.1 Problem Description

Mandel's Problem consists in a porous media, with height $2H$ and length $2L$, sandwiched between two frictionless, impermeable plates. A vertical force $2F$ is applied at the plates and the sample is drained from the sides, where it is free to deform. Due to the symmetry of the problem, the computational domain can be reduced as shown in Fig. 24

Figure 24 – Mandel's Problem - Description diagram.

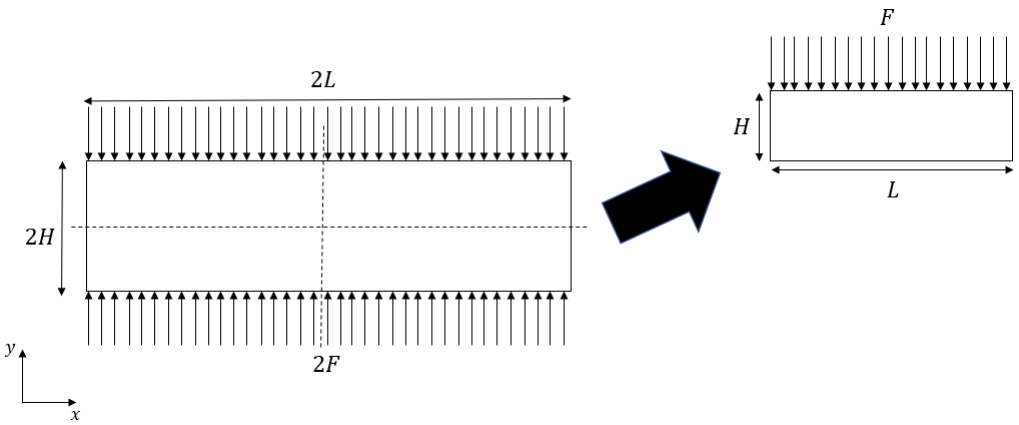

Source: Own authorship (2023)

Fig. 25 shows the computational domain dimensions and boundaries. The boundary conditions are shown in Table 10. Table 11 shows the material properties for both solid and fluid used in the present simulation. A mesh with resolution 30x6 was used in the simulation (Fig. 25). In addition, $p_0 = 6{,}675\ Pa$.

Figure 25 – Mandel's Problem - *a*) Domain dimensions, *b*) Domain Boundaries and *c*) Mesh used in the simulation.

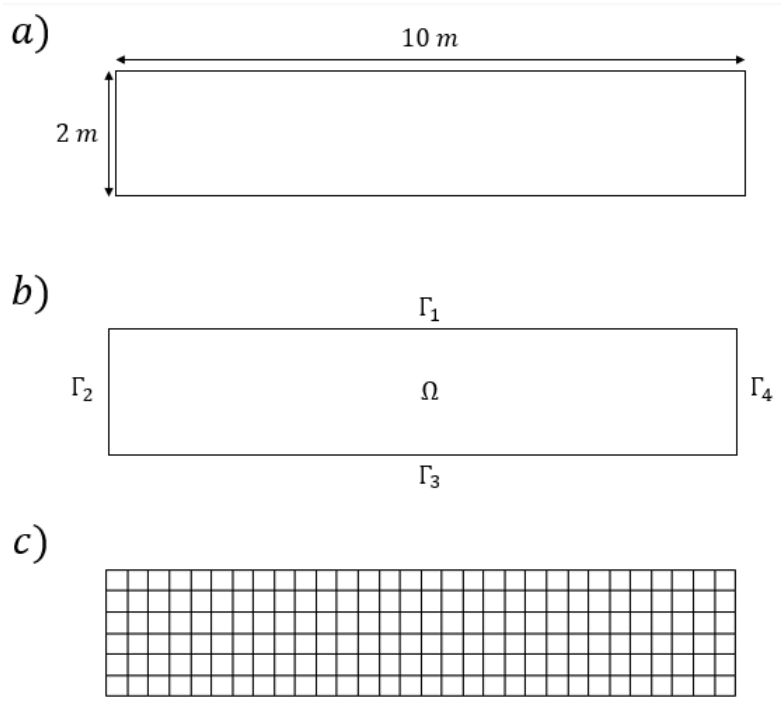

Source: Own authorship (2023)

Table 10 – Mandel's Problem - Boundary conditions.

Boundary	Fluid	Solid	
Γ_1	$\overrightarrow{v_t} \cdot \overrightarrow{n}_{IJ} = 0\ ms^{-1}$	$\mathcal{T}_x = 0\ Pa$	$F_y = -1 \times 10^6\ Pa$, $\partial_x v = 0$
Γ_2	$\overrightarrow{v_t} \cdot \overrightarrow{n}_{IJ} = 0\ ms^{-1}$	$u = 0\ m$	$\mathcal{T}_y = 0\ Pa$
Γ_3	$\overrightarrow{v_t} \cdot \overrightarrow{n}_{IJ} = 0\ ms^{-1}$	$\mathcal{T}_x = 0\ Pa$	$v = 0\ m$
Γ_4	$p = 0\ Pa$	$\mathcal{T}_x = 0\ Pa$	$\mathcal{T}_y = 0\ Pa$

Source: Own authorship (2023)

Table 11 – Mandel's Problem - Solid and fluid properties.

Property	Value
Solid Compressibility (c_s)	$0\ Pa^{-1}$
Young's Modulus (E)	$5 \times 10^9\ Pa$
Poisson's Coefficient (ν)	0.3
Porosity (ϕ)	0.3
Permeability (k)	$1 \times 10^{-13}\ m^2$
Biot's Coefficient (α)	1
Fluid Compressibility (c_f)	$4.5 \times 10^{-9}\ Pa^{-1}$
Viscosity (μ)	$1 \times 10^{-3}\ Pa.s$

Source: Own authorship (2023)

Mandel's problem has two unusual boundary conditions at Γ_1: $Fy = -1 \times 10^6$ and $\partial_x v = 0$. Since the imposed boundary condition is the total vertical force applied Fy, the load $\mathcal{T}_y$ at Γ_1 isn't necessary constant along the x direction. However, the total force at Γ_1 can be computed as follows:

$$F_y = \int_0^L \mathcal{T}_y \, dx \tag{4.3}$$

where L is the domain length.

In order to properly impose the boundary condition, an iterative method is employed:

1. A initial value of $\mathcal{T}_y$ is uniformly imposed as:

$$\mathcal{T}_y^k = \frac{F_y}{L} \tag{4.4}$$

2. Pressure and Displacement are obtained as usual.

3. A new value of $\mathcal{T}_y$ is computed numerically using the solutions obtained in the last item.

4. A convergence check is done:

$$\frac{\sum_{IJ\in\Gamma_1} |IJ| \overrightarrow{\mathcal{T}}^k_{IJ,y} - Fy}{Fy} \leq \tau_s \tag{4.5}$$

where τ_s is a user-defined tolerance, which in the present work is set to $\tau_s = 10^{-8}$.

If tolerance isn't achieved, a new value of $\mathcal{T}_y$ is uniformly imposed on the boundary:

$$\mathcal{T}_y^{k+1} = \mathcal{T}_y^k - \frac{\sum_{IJ\in\Gamma_1} |IJ| \overrightarrow{\mathcal{T}}^k_{IJ,y} - Fy}{L} \tag{4.6}$$

Then the algorithm resumes from step 2.

If tolerance is achieved, the simulation continues to the next value of t.

The second boundary condition $\partial_x v = 0$ which means v has a constant value along the x direction, but this value isn't necessarily known. In order to impose the aforementioned condition, one control volume, called $\hat{c}$, belonging to the boundary Γ_1 is chosen and every other volume in the boundary, called $\hat{b_i}$, is set to have the same value. This is achieved by changing the entries related to those volumes in the assembled matrix of the solid problem. The line corresponding to $\hat{c}$ is kept the same and the lines corresponding to $\hat{b_i}$ are changed to have 1 in the column corresponding to themselves, and -1 on the column corresponding to $\hat{c}$. The remaining columns are set to 0. There is no theoretical restriction to which volume should be chosen. However, after numerical testing, the one volume that yields the better results is the one closest to the boundary Γ_2 (Fig. 26).

Figure 26 – Mandel's Problem - Control volume used to impose constant displacement boundary condition.

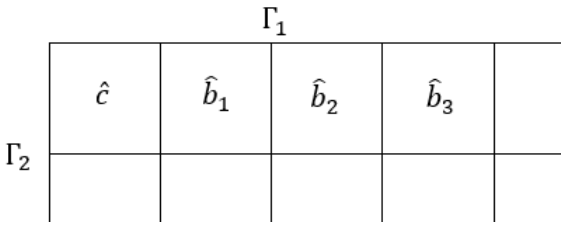

Source: Own authorship (2023)

4.4.2 Results

Fig. 27 shows a comparison between the numerical and analytic pressure solutions, whose description in detail can be found in Appendix A, along the line $x = 0\ m$ with $\Delta t = 0.1\ s$. From Fig. 27, one can conclude that the numerical formulation presented in this work is capable of accurately match the problem's analytical solution.

Figure 27 – Mandel's Problem - Pore pressure distribution with $\Delta t = 1\ s$.

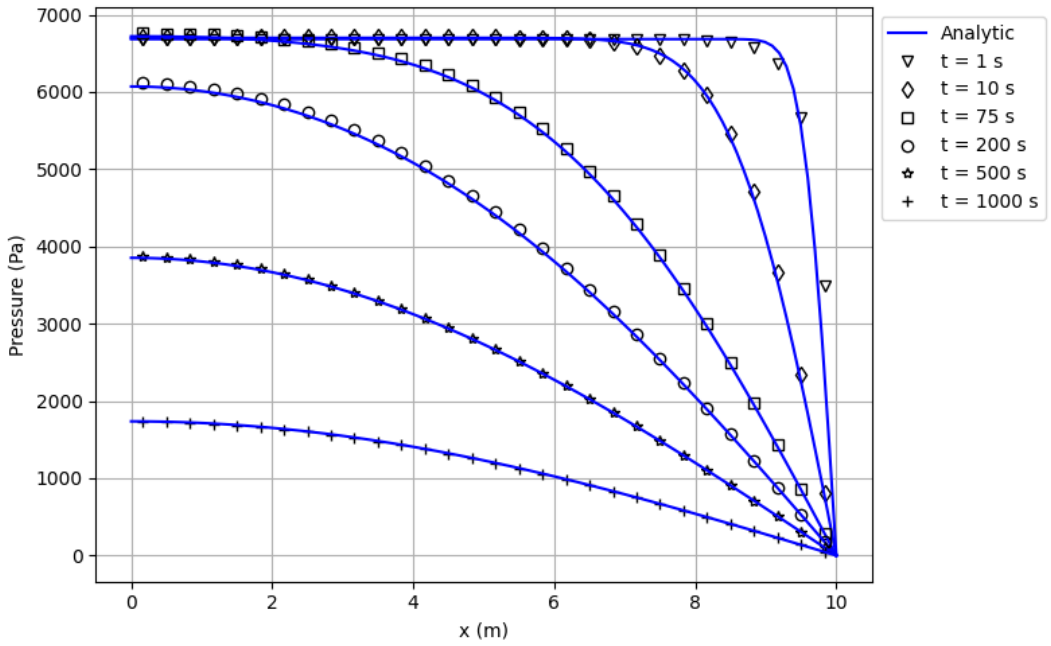

Source: Own authorship (2023)

Fig. 28, Fig. 29 and Fig. 30 show respectively the pressure, horizontal and vertical displacements profiles at different times. Fig. 31 shows the displacement field in different time values. From its analysis it is possible to conclude that the solution has the expected behaviour. Even though the problem is two-dimensional, the the pressure and horizontal displacements profiles only changes in the x direction and the vertical displacement only changes in the y directions. Furthermore, the horizontal displacement decreases over time due to fluid drainage, and the vertical displacement increases over time due to the solid compression.

Figure 28 – Mandel's Problem - Pore pressure profiles for different times with $\Delta t = 1\ s$.

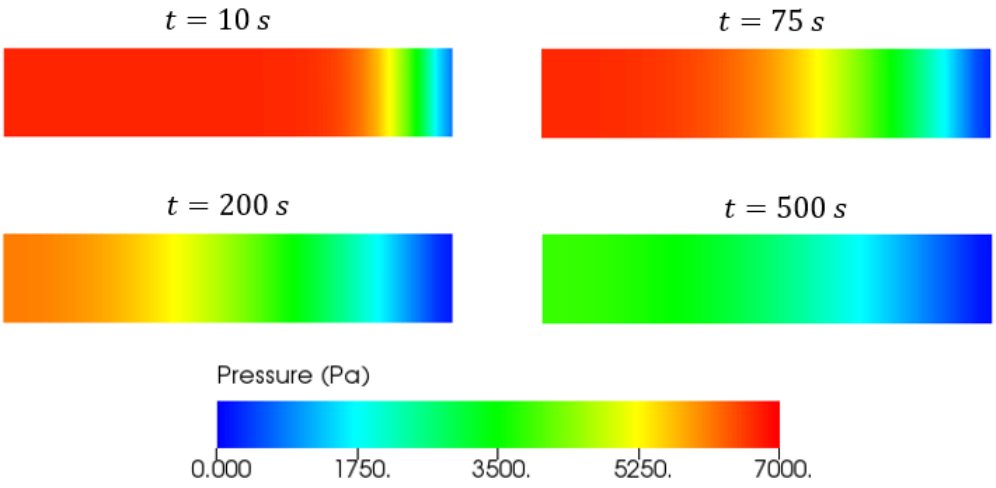

Source: Own authorship (2023)

Figure 29 – Mandel's Problem - Horizontal displacement profiles for different times with $\Delta t = 1\ s$.

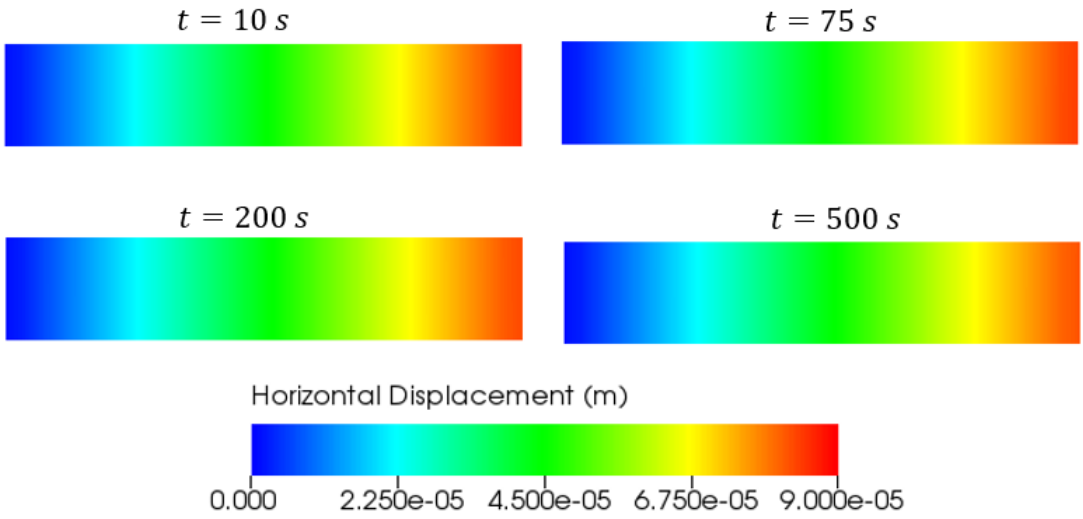

Source: Own authorship (2023)

Figure 30 – Mandel's Problem - Vertial displacement profiles for different times with $\Delta t = 1\ s$.

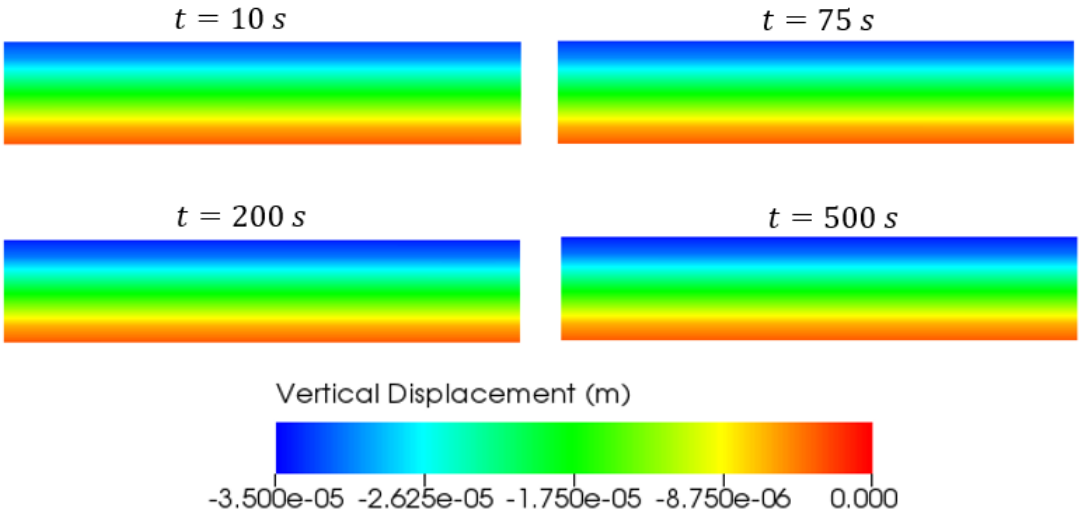

Source: Own authorship (2023)

Figure 31 – Mandel's Problem - Displacement field for different times with $\Delta t = 1\ s$.

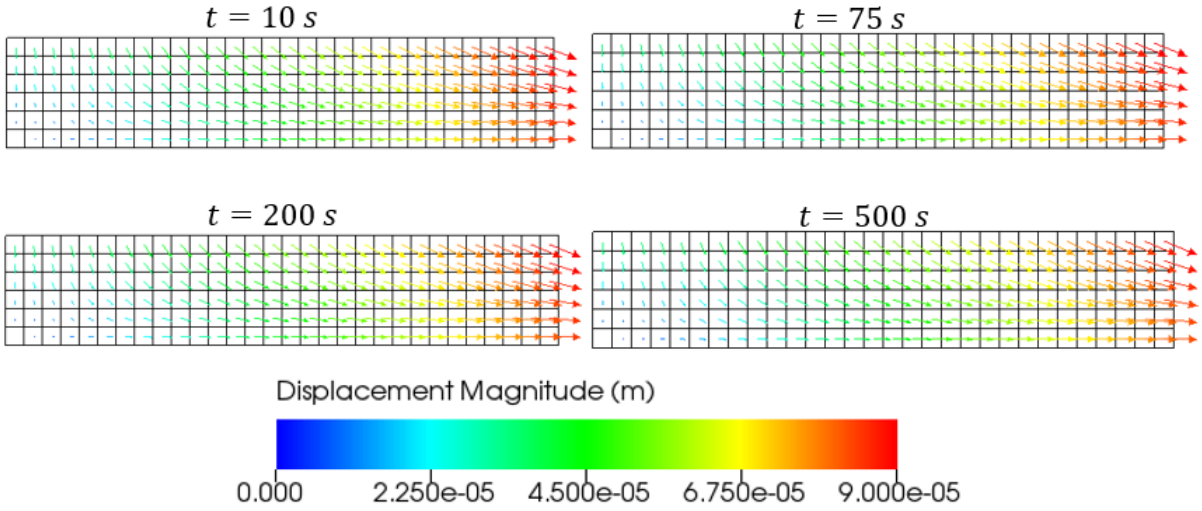

Source: Own authorship (2023)

5 CONCLUSION

5.1 Closing Remarks

From the analysis of the results showed in the present work, the numerical modeling described using a unified finite volume framework for solving poroelasticity problems was capable of producing accurate results using structured and unstructured meshes with triangular and quadrilateral elements.

In the homogeneous Terzaghi's problem, was possible to see the relationship between time step and mesh resolution, established by Fourier's number. It was shown that, even though the time integration scheme is unconditionally stable, high values of Fourier's number means mesh refinement has no effect on accuracy gain, as the error associated with time discretization is dominant, requiring a time step reduction in order to decrease error further.

In the two-layered Terzaghi's problem, it was shown how the pressure and displacemenet solutions are decoupled in Terzaghi's Model, where the displacement solutions for the homogeneous and heterogeneous cases showed the same behavior, albeit some small negligible difference.

In Mandel's problem, the numerical modeling was capable of reproduce the expected behavior, where pressure and horizontal displacement changes only in the x direction and decreases over time, meanwhile vertical displacement only changes in the y direction and increases over time.

In short, the closing remarks are:

- A Finite Volume Method based on a Multipoint Flux Approximations using harmonic points was developed for the solid mechanics problem;
- A unified Finite Volume Framework was developed for solving poroelasticity problems, using the Fixed-Strain operator split;
- The methodology was capable of producing accurate results for the benchmarks problems analyzed;
- It was possible to observe the relationship between time step size and mesh resolution, characterized by Fourier's number.
- By comparing the solutions of both homogeneous and heterogeneous versions of Terzaghi's problem, it was shown the decoupling between displacement and pressure in the Terzaghi's Model.

5.2 Suggestion for Future Works

The present work serves as a basis for future research in the field of poromechanics, more precisely, the usage of finite volume formulations in solid mechanics problems and in a unified finite volume framework for poromechanics problems, with applications in Reservoir Engineering. As suggestion for future works, one can cite a few:

- Verify the Rhie-Chow interpolation efficacy by solving examples where the even-odd decoupling can impact significantly the numerical solution.
- Introduce a non-linear finite volume formulation in the numerical framework;
- Extend the methodology presented to displacements in three dimensions;
- Modify the methodology to account for porosity and permeability changes;
- Incorporation of a multiphase or even a compositional flow model;
- Incorporation of elastoplastic constitutive model;
- Extend the numerical model to deal with fracture mechanics and fault reativation;
- Implement a solution algorithm base on the Fixed-Stress Split;

REFERENCES

ABOUSLEIMAN, Y. et al. Mandel's problem revisited. *Geotechnique*, Thomas Telford Ltd, v. 46, n. 2, p. 187–195, 1996.

AGÉLAS, L.; EYMARD, R.; HERBIN, R. A nine-point finite volume scheme for the simulation of diffusion in heterogeneous media. *Comptes Rendus Mathematique*, Elsevier, v. 347, n. 11-12, p. 673–676, 2009.

AMIRI, S. N.; HAJALI, M.; ESMAEILY, A. Consolidation of a layer under a strip loading and resting on an impermeable foundation. *Journal of Earth Sciences and Geotechnical Engineering*, v. 4, n. 2, p. 111–125, 2014.

ASADI, R.; ATAIE-ASHTIANI, B. Numerical modeling of subsidence in saturated porous media: A mass conservative method. *Journal of hydrology*, Elsevier, v. 542, p. 423–436, 2016.

ASADI, R.; ATAIE-ASHTIANI, B.; SIMMONS, C. T. Finite volume coupling strategies for the solution of a biot consolidation model. *Computers and Geotechnics*, Elsevier, v. 55, p. 494–505, 2014.

ASADOLLAHI, M. Finite volume method for poroelasticity. 2017.

BIOT, M. A. General theory of three-dimensional consolidation. *Journal of applied physics*, American Institute of Physics, v. 12, n. 2, p. 155–164, 1941.

BOOKER, J. The consolidation of a finite layer subject to surface loading. *International Journal of Solids and structures*, Elsevier, v. 10, n. 9, p. 1053–1065, 1974.

CARDIFF, P.; DEMIRDŽIĆ, I. Thirty years of the finite volume method for solid mechanics. *Archives of Computational Methods in Engineering*, Springer, v. 28, n. 5, p. 3721–3780, 2021.

CARDIFF, P.; KARAČ, A.; IVANKOVIĆ, A. Development of a finite volume contact solver based on the penalty method. *Computational Materials Science*, Elsevier, v. 64, p. 283–284, 2012.

CARDIFF, P.; KARAČ, A.; IVANKOVIĆ, A. A large strain finite volume method for orthotropic bodies with general material orientations. *Computer Methods in Applied Mechanics and Engineering*, Elsevier, v. 268, p. 318–335, 2014.

CAROLAN, D. et al. Arbitrary crack propagation in multi-phase materials using the finite volume method. *Computational materials science*, Elsevier, v. 69, p. 153–159, 2013.

CLOUGH, R. W. The finite element method in plane stress analysis. In: *Proceedings of 2nd ASCE Conference on Electronic Computation, Pittsburgh Pa., Sept. 8 and 9, 1960*. [S.l.: s.n.], 1960.

CONTRERAS, F. R. L. et al. A mpfa method using harmonic points coupled to a multidimensional optimal order detection method (mood) for the simulation of oil-water displacements in petroleum reservoirs. *Revista Interdisciplinar de Pesquisa em Engenharia*, v. 2, n. 21, p. 76–95, fev. 2017.

COWIN, S. C. Bone poroelasticity. *Journal of biomechanics*, Elsevier, v. 32, n. 3, p. 217–238, 1999.

CRYER, C. A comparison of the three-dimensional consolidation theories of biot and terzaghi. *The Quarterly Journal of Mechanics and Applied Mathematics*, Oxford University Press, v. 16, n. 4, p. 401–412, 1963.

DEMIRDZIC, I. Finite volumes vs finite elements. there is a choice. *Coupled systems mechanics*, Techno-Press, v. 9, n. 1, p. 5–28, 2020.

DEMIRDZIC, I.; MARTINOVIC, P.; IVANKOVIC, A. Numerical simulation of thermal deformation in welded workpiece. *Zavarivanje*, v. 31, n. 5, p. 209–219, 1988.

DETOURNAY, E.; CHENG, A. H.-D. Fundamentals of poroelasticity. In: *Analysis and design methods*. [S.l.]: Elsevier, 1993. p. 113–171.

EWING, R. E. *The mathematics of reservoir simulation*. [S.l.]: SIAM, 1983.

GAO, H.; ZHANG, J. Parallel 3-d simulation of seismic wave propagation in heterogeneous anisotropic media: a grid method approach. *Geophysical Journal International*, Blackwell Publishing Ltd Oxford, UK, v. 165, n. 3, p. 875–888, 2006.

GAO, Z.; WU, J. A small stencil and extremum-preserving scheme for anisotropic diffusion problems on arbitrary 2d and 3d meshes. *Journal of Computational Physics*, Elsevier, v. 250, p. 308–331, 2013.

GAO, Z.-M.; WU, J.-M. A linearity-preserving cell-centered scheme for the anisotropic diffusion equations. In: *Finite Volumes for Complex Applications VII-Methods and Theoretical Aspects*. Switzerland: Springer, 2014. p. 293–301.

GEUZAINE, C.; REMACLE, J. *Gmsh reference manual. the documentation for Gmsh 3.0*. [S.l.], 2017.

GREIN, T. B. P. Método dos volumes finitos baseado em elementos para a solução do escoamento bifásico em meios porosos com acoplamento geomecânico. 2019.

GRESHO, P. M.; SANI, R. L. Incompressible flow and the finite element method: Volume 1: Advection-diffusion. *John Wiley & Sons Ltd*, v. 168, p. 447–1020, 2000.

HENSEN, J. L.; NAKHI, A. E. Fourier and biot numbers and the accuracy of conduction modelling. In: *Proceedings of BEP'94 Conference*. [S.l.: s.n.], 1994. p. 247–256.

HERBIN, R.; HUBERT, F. Benchmark on discretization schemes for anisotropic diffusion problems on general grids, r. eymard and jm herard, editors, finite volume for complex applications, problems and perspectives. In: *5th International Conference, Wiley, New York, USA*. [S.l.: s.n.], 2008.

HONÓRIO, H. T. A stabilization technique for treating numerical instabilities in three-dimensional poroelasticity. 2018a.

HONORIO, H. T. et al. A stabilized element-based finite volume method for poroelastic problems. *Journal of Computational Physics*, Elsevier, v. 364, p. 49–72, 2018b.

HONÓRIO, H. T.; MARTINS, B.; MALISKA, C. R. A real-time optimization algorithm for the fixed-stress splitting scheme. *International Journal for Numerical Methods in Engineering*, Wiley Online Library, v. 122, n. 12, p. 2891–2918, 2021.

IMPRESS. *Intuitive Multilevel Preprocessor for Smart Simulation*. 2020. <https://github.com/padmec-reservoir/impress>. Accessed: 07-02-2023.

IRGENS, F. *Continuum mechanics*. [S.l.]: Springer Science & Business Media, 2008.

KEILEGAVLEN, E.; NORDBOTTEN, J. M. Finite volume methods for elasticity with weak symmetry. *International Journal for Numerical Methods in Engineering*, Wiley Online Library, v. 112, n. 8, p. 939–962, 2017.

KIM, J.; TCHELEPI, H. A.; JUANES, R. Stability and convergence of sequential methods for coupled flow and geomechanics: Drained and undrained splits. *Computer Methods in Applied Mechanics and Engineering*, Elsevier, v. 200, n. 23-24, p. 2094–2116, 2011a.

KIM, J.; TCHELEPI, H. A.; JUANES, R. Stability and convergence of sequential methods for coupled flow and geomechanics: Fixed-stress and fixed-strain splits. *Computer Methods in Applied Mechanics and Engineering*, Elsevier, v. 200, n. 13-16, p. 1591–1606, 2011b.

KIM, J.; TCHELEPI, H. A.; JUANES, R. Stability, accuracy, and efficiency of sequential methods for coupled flow and geomechanics. *SPE Journal*, OnePetro, v. 16, n. 02, p. 249–262, 2011c.

LIU, Z. L. Multiphysics in porous materials. In: *Multiphysics in Porous Materials*. [S.l.]: Springer, 2018. p. 29–34.

LLNL. *VisIt User Manual*. [S.l.], 2005.

MALANDRINO, A.; MOEENDARBARY, E. Poroelasticity of living tissues. *Encyclopedia of biomedical engineering*, Elsevier, p. 238–245, 2019.

MANDEL, J. Consolidation des sols (étude mathématique). *Geotechnique*, Thomas Telford Ltd, v. 3, n. 7, p. 287–299, 1953.

MCDONALD, P. W. *The computation of transonic flow through two-dimensional gas turbine cascades*. [S.l.]: American Society of Mechanical Engineers, 1971. v. 79825.

MCNAMEE, J.; GIBSON, R. Displacement functions and linear transforms applied to diffusion through porous elastic media. *The Quarterly Journal of Mechanics and Applied Mathematics*, Oxford University Press, v. 13, n. 1, p. 98–111, 1960b.

MCNAMEE, J.; GIBSON, R. E. Plane Strain and Axially Symmetric Problems of the consolidation of a semi-infinite clay stratum. *The Quarterly Journal of Mechanics and Applied Mathematics*, v. 13, n. 2, p. 210–227, 01 1960a. ISSN 0033-5614. Disponível em: <https://doi.org/10.1093/qjmam/13.2.210>.

MINKOFF, S. E.; KRIDLER, N. M. A comparison of adaptive time stepping methods for coupled flow and deformation modeling. *Applied mathematical modelling*, Elsevier, v. 30, n. 9, p. 993–1009, 2006.

MOEENDARBARY, E. et al. The cytoplasm of living cells behaves as a poroelastic material. *Nature materials*, Nature Publishing Group, v. 12, n. 3, p. 253–261, 2013.

NORDBOTTEN, J. M. Finite volume hydromechanical simulation in porous media. *Water Resources Research*, Wiley Online Library, v. 50, n. 5, p. 4379–4394, 2014a.

NORDBOTTEN, J. M. Cell-centered finite volume discretizations for deformable porous media. *International journal for numerical methods in engineering*, Wiley Online Library, v. 100, n. 6, p. 399–418, 2014b.

PIZZOL, A. D. Uma metodologia unificada empregando o método dos volumes finitos para a solução acoplada no escoamento e da geomecânica em meios porosos. 2014.

PIZZOL, A. D.; MALISKA, C. R. A finite volume method for the solution of fluid flows coupled with the mechanical behavior of compacting porous media. In: AMERICAN INSTITUTE OF PHYSICS. *AIP Conference Proceedings 4*. [S.l.], 2012. v. 1453, n. 1, p. 205–210.

RENDULIC, L. Der hydrodynamische spannungsausgleich in zentral entwässerten tonzylindern. *Wasserwirtschaft und technik*, v. 2, n. 23-26, p. 250–253, 1935.

RIBEIRO, G. G. Volumes finitos baseado em elementos para problemas de poroelasticidade. 2016.

RODRIGO, C. et al. Stability and monotonicity for some discretizations of the biot's consolidation model. *Computer Methods in Applied Mechanics and Engineering*, Elsevier, v. 298, p. 183–204, 2016.

SARVA, J. S.; RANI, S.; KUMAR, R. Consolidation of a poroelastic half–space. *Mathematical Journal of Interdisciplinary Sciences*, v. 2, n. 1, p. 1–18, 2013.

SETTARI, A.; WALTERS, D. A. Advances in coupled geomechanical and reservoir modeling with applications to reservoir compaction. *Spe Journal*, OnePetro, v. 6, n. 03, p. 334–342, 2001.

SHAW, G.; STONE, T. Finite volume methods for coupled stress/fluid flow in a commercial reservoir simulator. In: ONEPETRO. *Spe reservoir simulation symposium*. [S.l.], 2005.

SLAUGHTER, W. S. *The linearized theory of elasticity*. [S.l.]: Springer Science & Business Media, 2012.

SPALDING, D. Enlarging the frontiers of computational fluid dynamics. In: *International symposium heat and mass transfer and hydrodynamics in swirling flow, Moscow, Russia*. [S.l.: s.n.], 2008.

TANG, T.; HEDEDAL, O.; CARDIFF, P. On finite volume method implementation of poro-elasto-plasticity soil model. *International journal for numerical and analytical methods in geomechanics*, Wiley Online Library, v. 39, n. 13, p. 1410–1430, 2015.

TEREKHOV, K. M. Cell-centered finite-volume method for heterogeneous anisotropic poromechanics problem. *Journal of Computational and Applied Mathematics*, Elsevier, v. 365, p. 112357, 2020b.

TEREKHOV, K. M.; TCHELEPI, H. A. Cell-centered finite-volume method for elastic deformation of heterogeneous media with full-tensor properties. *Journal of Computational and Applied Mathematics*, Elsevier, v. 364, p. 112331, 2020a.

TEREKHOV, K. M.; VASSILEVSKI, Y. V. Finite volume method for coupled subsurface flow problems, i: Darcy problem. *Journal of Computational Physics*, Elsevier, v. 395, p. 298–306, 2019.

TEREKHOV, K. M.; VASSILEVSKI, Y. V. Finite volume method for coupled subsurface flow problems, ii: Poroelasticity. *Journal of Computational Physics*, Elsevier, v. 462, p. 111225, 2022.

TERZAGHI, K. Dir berenchnung der durchlassigkeitsziffer des tones aus dem verlaug der hidro-dynamischen spannungsercheinungen. *Akademie der Wissenschaften in Wein. Sitzungsberichte. Mathematish Naturwissenschaftliche Klasse*, n. part I, p. 125–138, 1923.

TERZAGHI, K. Theoretical soil mechanics john wiley and sons inc. *New York*, v. 314, 1943.

TERZAGHI, K.; FRÖHLICH, O. K. *Theorie der Setzung von Tonschichten: eine Einführung in die analytische Tonmechanik*. [S.l.]: Franz Deuticke, 1936.

TONELLI, R. Estratégias para tratamento do acoplamento escoamento/geomecânica utilizando volumes finitos. 2016.

TUKOVIĆ, Ž.; IVANKOVIĆ, A.; KARAČ, A. Finite-volume stress analysis in multi-material linear elastic body. *International journal for numerical methods in engineering*, Wiley Online Library, v. 93, n. 4, p. 400–419, 2013.

TUKOVIĆ, Ž. et al. Openfoam finite volume solver for fluid-solid interaction. *Transactions of FAMENA*, Fakultet strojarstva i brodogradnje, v. 42, n. 3, p. 1–31, 2018.

TURNER, M. J. et al. Stiffness and deflection analysis of complex structures. *journal of the Aeronautical Sciences*, v. 23, n. 9, p. 805–823, 1956.

VERRUIJT, A. Theory and problems of poroelasticity. *Delft University of Technology*, v. 71, 2013.

WANG, H. *Theory of linear poroelasticity with applications to geomechanics and hydrogeology*. [S.l.]: Princeton university press, 2000. v. 2.

WANG, J.; FANG, S. State space solution of non-axisymmetric biot consolidation problem for multilayered porous media. *International Journal of Engineering Science*, Elsevier, v. 41, n. 15, p. 1799–1813, 2003.

ZHANG, S.; ZHAO, X.; BAYYUK, S. Generalized formulations for the rhie–chow interpolation. *Journal of Computational Physics*, Elsevier, v. 258, p. 880–914, 2014.

ZOBACK, M. D. *Reservoir geomechanics*. [S.l.]: Cambridge university press, 2010.

APPENDIX A – ANALITIC SOLUTIONS

A.1 Terzaghi's Problem

The exact solution for Terzaghi's Problem can be found in (WANG, 2000). First, Terzaghi's Problem is one dimensional. Then, the author chooses the column top as the origin for the coordinate system and standard sign convention for the y axis.

When a load $-\sigma_0$ is applied at the column top, with height H, the sample reaches an equilibrium before fluid begins flowing, called undrained response where the initial pressure $p = 0$ becomes:

$$p_0 = \gamma\sigma_0 \tag{A.1}$$

where p_0 is the pressure at the equilibrium and γ is called loading efficiency, which is given by:

$$\gamma = \frac{B\,(1+\nu_{ud})}{3\,(1-\nu_{ud})} \tag{A.2}$$

where B is the Skempton's coefficient and ν_{ud} is the undrained Poisson's coefficient. B is a measure of how the load applied is shared between fluid and solid particles, during the undrained response. Furthermore, when the load is applied, the static fluid resist compression parallel to the load applied and increases stress in the perpendicular direction. Thus, the Poisson's coefficient measured during the undrained response is greater than the sample Poisson's coefficient ($\nu_{ud} > \nu$).

The vertical displacement at the undrained equilibrium is given by:

$$v_0 = \frac{\sigma_0\,(1+\nu_{ud})\,(H-y)}{3K_{ud}\,(1-\nu_{ud})} \tag{A.3}$$

where K_{ud} is the Bulk modulus measured at the undrained response.

Shortly after the sample reaches the undrained equilibrium, fluid beins flowing, entering the drained response. Then, the pressure and displacement behaviours are given by the following equations:

$$p\,(y,t) = p_0\Psi_p \tag{A.4}$$

$$v\,(y,t) = v_0 + p_0 \frac{\alpha\,(1+\nu)}{3K\,(1-\nu)}\left[(H-y) - \Psi_v\right] \tag{A.5}$$

where:

$$\Psi_p = \frac{4}{\pi}\sum_{m=0}^{\infty}\frac{1}{2m+1} sin\left[\frac{(2m+1)\,\pi y}{2H}\right] exp\left[\frac{-\,(2m+1)^2\,\pi^2 ct}{4H^2}\right] \tag{A.6}$$

$$\Psi_v = \frac{8}{\pi^2}\sum_{m=0}^{\infty}\frac{1}{(2m+1)^2} cos\left[\frac{(2m+1)\,\pi y}{2H}\right] exp\left[\frac{-\,(2m+1)^2\,\pi^2 ct}{4H^2}\right] \tag{A.7}$$

Moreover c is called the consolidation coefficient and is given by:

$$c = \frac{3k\gamma K\,(1-\nu)}{\mu\alpha\,(1+\nu)} \tag{A.8}$$

It's important to note that $\lim_{t\to 0^+} p(y,t) = p_0$ and $\lim_{t\to 0^+} v(y,t) = v_0$, which denotes the drained response beginning. The undrained response is instantaneous due to the quasi-static loading. Correlations for computing B, ν_{ud} and K_{ud} can be found in (WANG, 2000).

A.2 Two-Layered Terzaghi's Problem

The exact solution for the Two-layered Terzaghi's Problem can be found in (VERRUIJT, 2013). Similar to the homogenous case, the whole sample reaches the undrained equilibrium with p_0 given by Eq. (A.1). First, the material where the load is applied reaches p_0, thus γ is computed using its properties, then the other material reaches the same pressure p_0 at equilibrium. The coordinate system origin is placed at the interface between the two porous media, and standard sign convention is used for the y axis.

Where $y > 0$, the pressure behavior is given by:

$$p(y,t) = p_0 \Psi_p^1 \tag{A.9}$$

where:

$$\Psi_p^1 = 2\sum_{m=1}^{\infty}\frac{cos(A_m)cos(\beta A_m y/H_1) - \zeta sin(A_m)sin(\beta A_m y/H_1)}{R_m} exp\left(\frac{-A_m^2 t}{t_2}\right)$$

(A.10)

Furthermore, where y < 0, the pressure behavior is given by:

$$p(y,t) = p_0 \Psi_p^2 \tag{A.11}$$

where:

$$\Psi_p^2 = 2 \sum_{m=1}^{\infty} \frac{cos(A_m)cos(A_m y/H_2) - sin(A_m)sin(A_m y/H_2)}{R_m} exp\left(\frac{-A_m^2 t}{t_2}\right) \tag{A.12}$$

In Eq. (A.10) and Eq. (A.12), H_1 and H_2 are the heights of the upper and bottom materials respectively, and R_m is given by:

$$R_m = (1 + \zeta\beta)\, cos(\beta A_m)sin(A_m) + (\zeta + \beta)\, cos(A_m)sin(\beta A_m) \tag{A.13}$$

where A_m are the roots of the following equation:

$$-\zeta sin(\beta A)sin(A) + cos(\beta A)cos(A) = 0 \tag{A.14}$$

Furthermore, the coefficients ζ and β are defined as:

$$\zeta = \frac{\sqrt{k_2 m_2}}{\sqrt{k_1 m_1}},\ \beta = \sqrt{\frac{t_1}{t_2}} \tag{A.15}$$

where:

$$m_i = \left(K_i + \frac{4}{3}G_i\right)^{-1},\ t_i = \frac{H_i^2}{c_i},\ i = 1{,}2 \tag{A.16}$$

However, no analytical solution for displacement is supplied by the author.

A.3 Mandel's Problem

The exact solution for Mandel's Problem can be found in (ABOUSLEIMAN et al., 1996). The undrained equilibrium pressure p_0 is given by:

$$p_0 = \frac{FB(1+\nu_{ud})}{3L} \tag{A.17}$$

Then, the pressure behavior is given by:

$$p(x,t) = p_0 \Psi_p \tag{A.18}$$

where:

$$\Psi_p = 2\sum_{m=0}^{\infty} \frac{sin(A_m)}{A_m - sin(A_m)cos(A_m)} \left[cos\left(\frac{A_m x}{L}\right) - cos(A_m)\right] exp\left(\frac{-A_m^2 ct}{L^2}\right) \tag{A.19}$$

For Mandel's problem, the consolidation coefficient is defined as:

$$c = \frac{2kB^2G(1-\nu)(1+\nu_{ud})^2}{9\mu(1-\nu_{ud})(\nu_{ud}-\nu)} \tag{A.20}$$

Furthermore, A_m are the roots of the following equation:

$$tan(A) - \frac{(1-\nu)}{(\nu_{ud}-\nu)}A = 0 \tag{A.21}$$

The displacements behaviors are given by:

$$u(x,t) = \left(\frac{F\nu}{2GL} - \frac{F\nu_{ud}}{GL}\Psi_v\right)x + \frac{F}{G}\Psi_u \tag{A.22}$$

$$v(y,t) = \left(\frac{F(1-\nu_{ud})}{GL}\Psi_v - \frac{F(1-\nu)}{2GL}\right)y \tag{A.23}$$

where:

$$\Psi_v = \sum_{m=0}^{\infty} \frac{sin(A_m)cos(A_m)}{A_m - sin(A_m)cos(A_m)} exp\left(\frac{-A_m^2 ct}{L^2}\right) \tag{A.24}$$

$$\Psi_u = \sum_{m=0}^{\infty} \frac{cos(A_m)}{A_m - sin(A_m)cos(A_m)} sin\left(\frac{A_m x}{L}\right) exp\left(\frac{-A_m^2 ct}{L^2}\right) \tag{A.25}$$

APPENDIX B – ITERATIONS PER TIME STEP AND AVERAGE SIMULATION TIME

The following sections shows the results of average number of iterations per time step and average simulation time for the benchmark examples analysed in the present work.

B.1 Terzaghi's Problem

For Terzaghi's problem, simulations were done up to time $t = 4000\ s$ (Table 12), and for the convergence analysis simulations were done up to time $t = 20\ s$ (Table 13 and Table 14.

Table 12 – Terzaghi's Problem - Average Iterations per Time Step and Average CPU time with $dt = 1\ s$.

Mesh	Iterations per time step	Simulation time
A	20.03	219.399
B	20.05	250.102
C	35.09	384.286

Source: Own authorship (2023)

Table 13 – Terzaghi's Problem - Average Iterations per Time Step.

Δt	$1\ s$	$0.5\ s$	$0.25\ s$	$0.1\ s$	$0.05\ s$	$0.025\ s$
A1	21	20	19.22	18	17.44	16.79
A2	22	21	21	20	19	18.02
A3	22	22	21.52	20.73	20.10	19.29
A4	22	22	21.70	21.02	20.35	19.58
A5	22	22	21.74	21.12	20.47	19.66

Source: Own authorship (2023)

Table 14 – Terzaghi's Problem - Average CPU Time in Seconds.

Δt	$1\ s$	$0.5\ s$	$0.25\ s$	$0.1\ s$	$0.05\ s$	$0.025\ s$
A1	2.772	3.904	5.803	11.215	20.169	37.296
A2	4.766	7.233	10.851	20.798	36.913	68.496
A3	13.742	19.736	31.658	65.401	119.905	225.042
A4	30.986	46.348	76.784	161.814	303.789	570.122
A5	58.797	93.488	156.038	346.911	638.797	1215.718

Source: Own authorship (2023)

B.2 Two-Layered Terzaghi's Problem

For Two-Layered Terzaghi's problem, simulations were done up to time $t = 1200\ s$.

Table 15 – Two-Layered Terzaghi's Problem - Average Iterations per Time Step and Average CPU time with $dt = 0.1\ s$.

Mesh	Iterations per time step	CPU time (s)
Case 1	18.10	607.506
Case 2	17.40	609.796

Source: Own authorship (2023)

B.3 Mandel's Problem

For Mandel's problem, simulations were done up to time $t = 1100\ s$. Table 16 shows the average number of iterations for the convergence of the fixed-strain algorithm and the average number of iterations for the convergence of the boundary traction.

Table 16 – Mandel's Problem - Simulation data with $dt = 1\ s$.

Data	Value
Fixed Strain Iterations	3.30
Boundary Problem Iterations	6.554
CPU time (s)	589.895

Source: Own authorship (2023)